Insulator-metal transition in dense fluid deuterium

Insulator-metal transition in dense fluid deuterium

Peter M. Celliers,[1] Marius Millot,[1] Stephanie Brygoo,[2] R. Stewart McWilliams,[3] Dayne E. Fratanduono,[1] J. Ryan Rygg,[4,1] Alexander F. Goncharov,[5] Paul Loubeyre,[2] Jon H. Eggert,[1] J. Luc Peterson,[1] Nathan B. Meezan,[1] Sebastien Le Pape,[1] Gilbert W. Collins,[4,1] Raymond Jeanloz,[6] Russell J. Hemley[7]

[1] *Lawrence Livermore National Laboratory, Livermore, CA 94550, USA*
[2] *CEA, DAM, DIF, F-91297 Arpajon, France*
[3] *School of Physics and Astronomy and Centre for Science at Extreme Conditions, University of Edinburgh, Peter Guthrie Tait Road, Edinburgh, United Kingdom EH9 3FD*
[4] *Department of Mechanical engineering, Physics and Astronomy and Laboratory for Laser Energetics, University of Rochester, Rochester, NY 14623, USA*
[5] *Carnegie Institution of Washington, Washington, DC 20015, USA*
[6] *University of California, Berkeley, CA 94720, USA*
[7] *The George Washington University, Washington, DC 20052, USA*

Dense liquid metallic hydrogen occupies the interiors of Jupiter, Saturn and many extra-solar planets, where pressures reach millions of atmospheres. Planetary structure models must describe accurately the transition from the outer molecular envelopes to the interior metallic regions. We report optical measurements of dynamically compressed fluid deuterium to 600 GPa that reveal an increasing refractive index, the onset of absorption of visible light near 150 GPa and a transition to metal-like reflectivity (exceeding 30%) near 200 GPa, all at temperatures below 2000 K. Our measurements and analysis address existing discrepancies between static and dynamic experiments for the insulator-metal transition in dense fluid hydrogen isotopes. They also provide new benchmarks for the theoretical calculations used to construct planetary models.

The transformation of hydrogen from a molecular insulator to an atomic metal at high densities has been a longstanding focus in physics and planetary science (*1*). The unique quantum metallic properties of the low-temperature solid (*e.g.*, below 300 K) have been of sustained interest (*2–4*), and characterizing the transformation in the hot, dense fluid is crucial for understanding the internal structure and dynamics of giant planets (*5*), including the origin of their large magnetic fields (*6*). Numerous studies of the insulator-metal (IM) transition in dense fluid hydrogen beginning with theoretical work five decades ago predicted a first order transition in the fluid (*7–9*) with a critical point at very high temperatures (~13,000-15,000 K) and 60-90 GPa. However, the first experimental works on the IM transition in the fluid carried out using dynamic compression techniques provided evidence for a continuous transition with metallic states reached in the pressure range 50–140 GPa and temperatures of 3000-8000 (*10–12*). More recent predictions (*13–16*) placed the critical point at much lower temperature (~ 2000 K). This motivated several experimental studies using static diamond-anvil-cell techniques (*17–21*) and dynamic compression (*22*) to probe the fluid properties below 2000 K and up to several hundred GPa pressure.

Dynamic compression can explore a broad range of thermodynamic paths with time-varying manipulations of the applied pressure and controlled reverberation of pressure waves through the sample. This includes probing the dense fluid at temperatures below 2000 K, for example, by combining an initial jump in pressure delivered by a shock wave followed by shock reverberation or gradual ramp compression. The demonstration of this strategy was carried out on deuterium with a magnetic compression technique at the *Z* facility (*22*). The results showed strong optical absorption beginning in the range $100 < P < 130$ GPa, followed by weak fluctuating reflectance in the range $130 < P < 300$ GPa, and culminated in abrupt jumps to high reflectance near 300 GPa. They attributed the absorption to band gap closure and determined the reflectance jumps were associated with the first-order IM transition. The reflectance jumps occurred at higher pressures on compression than on decompression, plausibly due to thermal conduction. Meanwhile, improvements in static compression methods have allowed the exploration of the behavior of the fluid over part of this pressure-temperature (*P*-*T*) range (up to 170 GPa and over 1800 K) (*17–21*, *23–25*). Changes in optical properties from 120-170 GPa depending on temperature were attributed to the IM transition (*17–19*, *21*), whereas other experiments suggest the persistence of a finite (~1 eV) band gap at similar conditions (*20*).

The IM transition is the subject of a number of continuing theoretical studies (*13–16*, *26–28*), which consistently predict a discontinuous transition below a critical point near ~2000 K, but over a broad range of pressures. Density functional theory-based (DFT) calculations show a spread in the transition pressure spanning 150 GPa, arising from the sensitivity of the boundary to the choice of exchange-correlation functional used, and whether zero-point energy is accounted for (*1*, *15*). Quantum Monte Carlo (QMC) calculations should provide improved bounds on the transition pressures (*15*, *16*), although they disagree with a recent benchmarking experiment (*29*). Transition pressures for hydrogen and deuterium are expected to be different because of isotope effects, but with a small relative magnitude. The transition in deuterium from QMC simulations is 30 GPa higher than in hydrogen at 600 K and decreases to 10 GPa at 1200 K (*15*). Despite experimental support for a first-order IM transition (*18*, *19*, *21*, *22*), the critical point has not been experimentally identified. Furthermore, the broad discrepancies in the measured transition pressure (*19*, *21*, *22*) and character (*19–22*) have made resolving the differences between the theoretical models challenging.

We completed a series of five dynamic compression experiments at the National Ignition Facility (NIF) to probe the IM transition up to 600 GPa and at temperatures ranging from 900 K to 1600 K. The experiments were carried out using 168 laser beams to deliver up to 300 kJ of UV light that drove a near-isentropic reverberation compression of a cryogenic liquid deuterium sample. Adjustment of the time dependence of the laser delivery (pulse shape) controls the compression sequence imposed on the sample as a function of time. Line-imaging Doppler velocimetry recorded both the compression history and the evolution of the optical properties of the D_2 sample during the nanosecond compression process, using a probe laser operating at 660 nm.

Our fluid deuterium sample is sandwiched between a copper piston and a LiF window and is viewed through the window by the diagnostic (Fig. 1). The upper half of the view shows signal from the light reflected at the D_2-LiF interface where a 100 nm thick aluminum film was deposited (position > 0 μm in top panel of Fig. 1B,C). The lower half shows the signal from light reflected initially at the piston surface (double-passed through the transparent sample layer). Because the two reflecting interfaces move differently the two halves of the field of view display different apparent velocities (different fringe phases) until the time when the light intensity on the sample side reaches a minimum. At later times the apparent velocity on the sample side matches that of the Al-LiF interface (common fringe phase) indicating that the optical reflection has shifted from the piston surface to the D_2-LiF interface.

The copper piston (lower half) started moving near t = 10 ns when an initial weak shock was transmitted into the sample layer. We controlled the first shock strength for each experiment in order to follow different isentropic compression paths. The first shock strengths varied from 1.8 GPa to 3.4 GPa (Table S1). After the first shock crossed the sample layer it reverberated against the LiF window (upper half, 16 ns), and continued to reverberate between the piston and the window while the sample layer was compressed. After several reverberations both the piston and window interface approached a common apparent velocity by 27 ns. At this point the sample was compressed to conditions estimated to be near $\rho \approx 0.8$ g/cm^3, $P \approx$ 20-30 GPa, $T \approx$ 600-900 K and observed to be fully transparent. A second pressure wave arrived at the sample layer at 30 ns and initiated a second set of reverberations, further pressurizing the sample to nearly 600 GPa in four experiments and to 215 GPa in one experiment. The duration of this second set of reverberations was shorter than the first, accomplishing much of the pressure increase in less than 3 ns. The transition from optically transparent to strongly reflecting occured during the second set of reverberations and is attributed to the insulator-metal (IM) transition in deuterium.

The thermodynamic path of the sample was inferred from hydrodynamic simulations constrained by the measured interface velocities (*30*), similar to previous work (*22*). Different equation of state (EOS) models for deuterium (*31–33*) resulted in calculated pressures that are nearly the same to within 1% percent independent of the EOS model. We estimate the pressure along the compression path is accurate to ±3 GPa (measurement error of the velocities), enabling determination of the metallization pressure to <3% accuracy (after accounting for measurement error in the reflectance). The EOS models compare well with recent benchmarking experiments (*12*, *29*, *34*). However, none of the current EOS models include a representation of the IM transition as a first-order phase transition and the range of temperature predictions among EOS models is large leading to uncertainties as much as ±260 K near the IM transition. Density is known to within ±6% among the models.

Several optical signatures are associated with the transition from transparent to reflecting (Fig. 2). While the sample layer remained partially transparent we determined the absorption coefficient up to a magnitude of about 1 μm^{-1} (Fig. 2B), when the optical depth of the sample layer exceeded ≈ 2 and the layer became opaque. When the sample

was opaque light continued to be returned from the target because of the reflection from the D_2-LiF interface, with reflectance near 10%. While the sample was still partially transparent we observed changes in the real part of the index of refraction that are consistent with band-gap closure. We extracted the real part of the index of refraction (Fig. 2C) by fitting to the apparent velocity of the piston (observed through the deuterium sample) self-consistently with our hydrodynamic simulation (*30*) (Fig. 1). The real part of the index agrees closely with that of insulating hydrogen at lower pressure (*35*) but deviates from the low-pressure linear density dependence as the band gap decreases.

The gap energy, which we estimated from the refractive index (*30*), approaches ~2 eV when the sample layer becomes opaque, consistent with the wavelength 1.9 eV probe. Extrapolation (linear in density) suggests that, for the fluid deuterium states achieved in our study, the band gap closes in the range $200 < P < 250$ GPa (*30*) depending on the experiment (Fig. S22B). The ≈10% reflectance we observed when the sample becomes opaque (Fig. 2A) is consistent with the expected reflectivity of the pressurized D_2-LiF interface with $n_{D2} \approx 2.8$ and $n_{LiF} \approx 1.5$ and represents a minimum reflectivity of insulating deuterium in this experiment. Further pressurization reveals a rapid increase in reflectivity at the D_2-LiF interface eventually reaching a saturation level near 55%. Reflectivity of ≈30% at the D_2-LiF interface corresponds to the minimum metallic electrical conductivity $\sigma_{DC} \approx 2000$ S/cm (*10*, *36*); values exceeding this indicate metallic behavior (*30*). From this measurement we inferred that the IM transition occurs in the pressure range between approximately 150 GPa and 250 GPa. While we did not observe a discontinuous change in reflectivity through this range for three of our experiments finite temporal resolution in the measurements may have obscured a sharp transition; one experiment (magenta dashed curves and Fig. 2A inset) recorded at higher time resolution revealed a sharp reflectivity increase. In all cases the reflectivity increase steepened noticeably near 200 GPa. Of the four experiments reaching 600 GPa peak pressure, we recorded some of the reflectivity data during pressure relaxation; unlike prior experiments (*22*) there is no evidence for different reflectivity signals during increasing ($dP/dt > 0$) and decreasing ($dP/dt < 0$) pressurization.

We can fit our results to simple models of the evolution of the optical properties through the transparent, optically absorbing, and optically reflecting regimes. The absorption has a steep pressure dependence and increases with temperature (Fig. 2B), most likely due to disorder in the material. In the partially transparent regime we extracted the optical conductivity (Fig. 2D, symbols) directly from our data using the expression $\sigma(\omega) = n\alpha c$ (Gaussian units) where n is the real part of the index of refraction (Fig. 2B), α is the absorption coefficient (Fig. 2C), and c the speed of light. A Lorentz optical model incorporating a density-dependent oscillator frequency matches these data (Fig. 2D, curves below 150 GPa). We estimated the DC conductivity above the transition (Fig. 2D, $P >$150 GPa) with the Smith-Drude model (*20*, *37*) evaluated with a fixed relaxation time τ=0.075 fs and variable backscatter parameter matched to the optical reflectivity (Fig. 2A and Fig. S25). The conductivities determined here exhibit similar trends to those calculated theoretically (*13*).

We plotted the optical absorption and reflectivity signatures along the calculated temperature versus pressure (*T*-*P*) paths extracted from the simulation models (Fig. 3), referred to by their *T* near 200 GPa (Table S1). Our observations of the onset of optical absorption (open circles in Fig. 3) are in good agreement with the results of McWilliams *et al*. (*20*) and Knudson *et al*. (*22*) black dashed line in Fig. 3). These observations along with the extrapolated band gap energy as a function of *P* (Fig. S22B) imply that the band gap remains finite leading up to the IM transition. These conclusions differ from those of several diamond anvil cell (DAC) measurements performed at similar conditions (*17–19*, *21*). The DAC measurements using laser heating produced plateaus in temperature with increasing laser power that were interpreted as a signature of the metallization transition (*17–19*, *21*). However, the heating plateaus in the static experiments are better correlated with the onset of absorption in our experiment rather than metallization, consistent with alternative interpretations of those data (*20*, *38*, *22*). The observation of absorption well below the point of band gap closure is also found in the solid at lower temperatures (*39*, *40*).

We found saturation of the reflectivity above ~280 GPa in the four experiments carried out to the highest pressures. In these datasets the transition temperature exhibited a clear trend decreasing with pressure by ≈20 K/GPa. The lowest observation at $T \sim 1100$ K showed the transition occurring at 221 GPa. One experiment at even lower $T \sim 940$ K did not reveal reflectivity greater than 10% to the maximum $P \sim 215$ GPa, but does not rule out the possibility of a transition at higher *P*. Pulsed heating DAC experiments on H_2 (*19*, *21*), found reflectivity saturation at temperatures similar to our experiments and ~20 GPa lower pressure, which may be consistent with the expected isotope effect.

The steep increase in reflectivity with pressure that we observe near 200 GPa contrasts with the interpretation of the ramp compression experiment on deuterium carried out at the Z facility (*22*). Although the onset of optical absorption is consistent with our work, the subsequent weak reflectivity followed by jumps near 300 GPa (attributed to the IM transition) occured at higher pressure than observed here and in other later studies (*19*, *21*), while the low (< 2%) reflectivity of the D_2-LiF interface recorded at intermediate conditions is not consistent with either insulating or semiconducting deuterium and LiF under pressure (*30*, *35*, *41*, *42*). While our data indicates onset of the IM transition at *P* ~200 GPa the optical reflectivity saturates to a constant value of ~55% near 280 GPa, and remains stable over hundreds of GPa, similar to the pressures where high reflectivity is displayed in the Z experiments. This shows that both experiments are probing similar states at onset and completion of the IM transition, but not at intermediate conditions.

We propose that the different results are related to the two-orders of magnitude longer time scale of the Z experiments, allowing turbulent lateral flows within the sample layer to be established during the observations. These effects lead to a different interpretation of the reflectivity jumps observed in the Z data, correlating these with completion rather than onset of the IM transformation (*30*). This requires a correction of the inferred transition temperatures from the Z-machine to lower values (Table S3), owing to the latent heat of the IM transition. Although there are uncertainties in the temperature estimates in both experiments, we expect that those uncertainties are accentuated by the

longer time scales, which give rise to multiple mechanisms of heat transport in the Z experiments. The much shorter time scales in our experiments preclude these from occurring, so that the temperature estimates for our experiments depend primarily on the EOS models in the molecular fluid phase.

We interpreted the onset of reflectivity above 10% as the beginning of pressure-induced molecular dissociation associated with the IM transition. The extent and *P-T* range of the IM transition are in approximate agreement with the DFT-based molecular dynamics calculations using the van der Waals (vdW-DF1) exchange-correlation functional (*43*) reported in Knudson *et al*. (*22*) Our observations and analyses are also consistent with the CEIMC calculations of Pierleoni *et al*. (*15*) and with the quantum Monte Carlo calculations of Mazzola *et al*. (*16*). They are about 100 GPa higher than DFT calculations based on the Perdew-Burke-Ernzerhof (*44*) (PBE) exchange-correlation functional (*28*, *14*) and about 50 GPa lower than DFT calculations based on the van der Waals vdW-DF2 functional (*22*, *45*). In the saturation regime the estimated $\sigma_{DC} \approx 10^4$ S/cm is in good agreement with the recent estimates from lower pressure experiments (*21*) and with calculations (*13*).

Our interpretation of the Z experiments does not alter the conclusion that the abrupt reflectivity jumps observed in those experiments are evidence of a first-order insulator-metal transition. The revised $\underline{T} \approx 600$ K are well below the predicted critical point temperature, while one of our experiments provides evidence for first order behavior up to 1100 K. The extrapolated band gap energies (linear in density, Fig. S22B) reach closure at higher *P* than the corresponding observed transition *P*, indicating that the gap closes non-linearly and could indicate first-order behavior as high 1640 K. Therefore, while the critical point temperature, T_{CP}, is not yet precisely identified, it is bounded in the range $3000\ \text{K} > T_{CP} > 1100$ K, based on our data and continuous transformations observed in prior experiments to higher temperature (*10*).

Our revision of the IM transition data from the Z experiments lies close to and even below previous melting line studies on hydrogen (*25*, *23*) A straight line connecting our data to the revised Z data has a slope of –5 K/GPa. This invites speculation as to whether a thermodynamic triple point with coexisting crystalline solid, insulating fluid and liquid metal phases is located near 600 K and 300 GPa. If so, at higher pressure the insulating crystalline solid would transform directly to the liquid metal. Since the melting line of deuterium hasn't been determined, and quantum effects are important, the existence and location of such a triple point remains an open question.

Demixing in dense H-He fluid mixtures, an important process expected to occur inside giant planets (*46*, *47*), is closely connected with the IM transition (*48*). Recent state-of-the-art calculations of H-He demixing are all based on *ab-initio* calculations with increasing levels of sophistication (*48–54*). The two most recent calculations of H and He EOS for planetary models are based on DFT molecular dynamics (*55*, *56*) with the PBE exchange-correlation functional and until this year *ab-initio*-based demixing studies (*52*, *53*) were also based on PBE. The emerging theoretical (*15*, *16*) and experimental (*22*) evidence that PBE underestimates the IM transition pressure motivated Schöttler and

Redmer (*54*) to examine H-He demixing with the vdW-DF1 functional. They showed a clear shift of the demixing boundary to higher pressure and lower temperature compared to PBE-based calculations. Thus, while the first-order IM transition occurs at much lower temperature than the Jupiter and Saturn isentropes it plays an important role as a benchmarking feature to validate the functional on which the H-He demixing calculations are based.

References

1. J. M. McMahon, M. A. Morales, C. Pierleoni, D. M. Ceperley, The properties of hydrogen and helium under extreme conditions. *Rev. Mod. Phys.* **84**, 1607–1653 (2012).

2. N. W. Ashcroft, Metallic Hydrogen: A High-Temperature Superconductor? *Phys. Rev. Lett.* **21**, 1748–1749 (1968).

3. E. G. Brovman, Y. Kagan, A. Kholas, Properties of metallic hydrogen under pressure. *Sov. Phys. JETP*. **35**, 783 (1972).

4. E. Babaev, A. Sudbo, N. W. Ashcroft, A superconductor to superfluid phase transition in liquid metallic hydrogen. *Nature*. **431**, 666–668 (2004).

5. N. Nettelmann, A. Becker, B. Holst, R. Redmer, Jupiter Models with Improved Ab Initio Hydrogen Equation of State (H-REOS.2). *The Astrophysical Journal*. **750**, 52 (2012).

6. J. E. P. Connerney *et al.*, The Juno Magnetic Field Investigation. *Space Science Reviews*. **213**, 39–138 (2017).

7. G. É. Norman, A. N. Starostin, Thermodynamics of a dense plasma. *Journal of Applied Spectroscopy*. **13**, 965–967 (1970).

8. W. Ebeling, W. Richert, Plasma phase transition in hydrogen. *Physics Letters A*. **108**, 80–82 (1985).

9. D. Saumon, G. Chabrier, Fluid hydrogen at high density: The plasma phase transition. *Phys. Rev. Lett.* **62**, 2397–2400 (1989).

10. S. T. Weir, A. C. Mitchell, W. J. Nellis, Metallization of Fluid Molecular Hydrogen at 140 GPa (1.4 Mbar). *Phys. Rev. Lett.* **76**, 1860–1863 (1996).

11. P. M. Celliers *et al.*, Shock-Induced Transformation of Liquid Deuterium into a Metallic Fluid. *Phys. Rev. Lett.* **84**, 5564–5567 (2000).

12. P. Loubeyre *et al.*, Extended data set for the equation of state of warm dense hydrogen isotopes. *Phys. Rev. B*. **86**, 144115 (2012).

13. W. Lorenzen, B. Holst, R. Redmer, First-order liquid-liquid phase transition in dense hydrogen. *Phys. Rev. B*. **82**, 195107 (2010).

14. M. A. Morales, C. Pierleoni, E. Schwegler, D. M. Ceperley, Evidence for a first-order liquid-liquid transition in high-pressure hydrogen from ab initio simulations. *Proceedings of the National Academy of Sciences*. **107**, 12799–12803 (2010).

15. C. Pierleoni, M. A. Morales, G. Rillo, M. Holzmann, D. M. Ceperley, Liquid–liquid phase transition in hydrogen by coupled electron–ion Monte Carlo simulations. *Proceedings of the National Academy of Sciences*. **113**, 4953–4957 (2016).

16. G. Mazzola, R. Helled, S. Sorella, Phase Diagram of Hydrogen and a Hydrogen-Helium Mixture at Planetary Conditions by Quantum Monte Carlo Simulations. *Phys. Rev. Lett.* **120**, 025701 (2018).

17. V. Dzyabura, M. Zaghoo, I. F. Silvera, Evidence of a liquid–liquid phase transition in hot dense hydrogen. *Proceedings of the National Academy of Sciences*. **110**, 8040–8044 (2013).

18. K. Ohta *et al.*, Phase boundary of hot dense fluid hydrogen. **5**, 16560 (2015).

19. M. Zaghoo, A. Salamat, I. F. Silvera, Evidence of a first-order phase transition to metallic hydrogen. *Phys. Rev. B*. **93**, 155128 (2016).

20. R. S. McWilliams, D. A. Dalton, M. F. Mahmood, A. F. Goncharov, Optical Properties of Fluid Hydrogen at the Transition to a Conducting State. *Phys. Rev. Lett.* **116**, 255501 (2016).

21. M. Zaghoo, I. F. Silvera, Conductivity and dissociation in liquid metallic hydrogen and implications for planetary interiors. *Proceedings of the National Academy of Sciences* (2017), doi:10.1073/pnas.1707918114.

22. M. D. Knudson *et al.*, Direct observation of an abrupt insulator-to-metal transition in dense liquid deuterium. *Science*. **348**, 1455–1460 (2015).

23. C. Zha, H. Liu, J. S. Tse, R. J. Hemley, Melting and High P-T Transitions of Hydrogen up to 300 GPa. *Phys. Rev. Lett.* **119**, 075302 (2017).

24. N. Subramanian, A. F. Goncharov, V. V. Struzhkin, M. Somayazulu, R. J. Hemley, Bonding changes in hot fluid hydrogen at megabar pressures. *Proceedings of the National Academy of Sciences*. **108**, 6014–6019 (2011).

25. R. T. Howie, P. Dalladay-Simpson, E. Gregoryanz, Raman spectroscopy of hot hydrogen above 200 GPa. *Nat Mater*. **14**, 495–499 (2015).

26. W. J. Nellis, A. A. Louis, N. W. Ashcroft, Metallization of fluid hydrogen. *Philosophical Transactions of the Royal Society A - Mathematical, Physical and Engineering Sciences*. **356**, 135-- 138 (1998).

27. S. Scandolo, Liquid–liquid phase transition in compressed hydrogen from first-principles simulations. *Proceedings of the National Academy of Sciences*. **100**, 3051–3053 (2003).

28. I. Tamblyn, S. A. Bonev, Structure and Phase Boundaries of Compressed Liquid Hydrogen. *Phys. Rev. Lett.* **104**, 065702 (2010).

29. M. D. Knudson, M. P. Desjarlais, High-Precision Shock Wave Measurements of Deuterium: Evaluation of Exchange-Correlation Functionals at the Molecular-to-Atomic Transition. *Phys. Rev. Lett.* **118**, 035501 (2017).

30. P. M. Celliers *et al.*, Supplementary Material.

31. G. I. Kerley, "Equations of State for Hydrogen and Deuterium" (SAND2003-3613, Sandia National Laboratories, 2003).

32. L. Caillabet, S. Mazevet, P. Loubeyre, Multiphase equation of state of hydrogen from ab initio calculations in the range 0.2 to 5 g/cc up to 10 eV. *Phys. Rev. B*. **83**, 094101 (2011).

33. A. Correa, L. X. Benedict, Equation of State of Hydrogen (2017).

34. S. Brygoo *et al.*, Analysis of laser shock experiments on precompressed samples using a quartz reference and application to warm dense hydrogen and helium. *Journal of Applied Physics*. **118**, 195901 (2015).

35. A. Dewaele, J. H. Eggert, P. Loubeyre, R. Le Toullec, Measurement of refractive index and equation of state in dense He, H2, H2O, and Ne under high pressure in a diamond anvil cell. *Phys. Rev. B*. **67**, 094112 (2003).

36. W. J. Nellis, S. T. Weir, A. C. Mitchell, Minimum metallic conductivity of fluid hydrogen at 140 GPa (1.4 Mbar). *Phys. Rev. B*. **59**, 3434–3449 (1999).

37. N. V. Smith, Classical generalization of the Drude formula for the optical conductivity. *Phys. Rev. B*. **64**, 155106 (2001).

38. Z. M. Geballe, R. Jeanloz, Origin of temperature plateaus in laser-heated diamond anvil cell experiments. *Journal of Applied Physics*. **111**, 123518 (2012).

39. H. Mao, R. J. Hemley, Ultrahigh-pressure transitions in solid hydrogen. *Rev. Mod. Phys.* **66**, 671–692 (1994).

40. P. Loubeyre, F. Occelli, R. LeToullec, Optical studies of solid hydrogen to 320 GPa and evidence for black hydrogen. *Nature*. **416**, 613–617 (2002).

41. D. E. Fratanduono *et al.*, Refractive index of lithium fluoride ramp compressed to 800 GPa. *Journal of Applied Physics*. **109**, 123521 (2011).

42. P. A. Rigg, M. D. Knudson, R. J. Scharff, R. S. Hixson, Determining the refractive index of shocked [100] lithium fluoride to the limit of transmissibility. *J. Appl. Phys.* **116**, 033515 (2014).

43. M. Dion, H. Rydberg, E. Schröder, D. C. Langreth, B. I. Lundqvist, Van der Waals Density Functional for General Geometries. *Phys. Rev. Lett.* **92**, 246401 (2004).

44. J. P. Perdew, K. Burke, M. Ernzerhof, Generalized Gradient Approximation Made Simple. *Phys. Rev. Lett.* **77**, 3865–3868 (1996).

45. K. Lee, É. D. Murray, L. Kong, B. I. Lundqvist, D. C. Langreth, Higher-accuracy van der Waals density functional. *Phys. Rev. B*. **82**, 081101 (2010).

46. E. E. Salpeter, On Convection and Gravitational Layering in Jupiter and in Stars of Low Mass. *The Astrophysical Journal*. **181**, L83 (1973).

47. D. J. Stevenson, E. E. Salpeter, The dynamics and helium distribution in hydrogen-helium fluid planets. *Astrophysical Journal Supplement Series*. **35**, 239–261 (1977).

48. W. Lorenzen, B. Holst, R. Redmer, Demixing of Hydrogen and Helium at Megabar Pressures. *Phys. Rev. Lett.* **102**, 115701 (2009).

49. J. E. KLEPEIS, K. J. SCHAFER, T. W. BARBEE, M. Ross, Hydrogen-Helium Mixtures at Megabar Pressures: Implications for Jupiter and Saturn. *Science*. **254**, 986 (1991).

50. O. Pfaffenzeller, D. Hohl, P. Ballone, Miscibility of Hydrogen and Helium under Astrophysical Conditions. *Phys. Rev. Lett.* **74**, 2599–2602 (1995).

51. J. Vorberger, I. Tamblyn, B. Militzer, S. A. Bonev, Hydrogen-helium mixtures in the interiors of giant planets. *Phys. Rev. B*. **75**, 024206 (2007).

52. M. A. Morales *et al.*, Phase separation in hydrogen–helium mixtures at Mbar pressures. *Proc Natl Acad Sci USA*. **106**, 1324 (2009).

53. M. A. Morales, S. Hamel, K. Caspersen, E. Schwegler, Hydrogen-helium demixing from first principles: From diamond anvil cells to planetary interiors. *Phys. Rev. B*. **87**, 174105 (2013).

54. M. Schöttler, R. Redmer, Ab Initio Calculation of the Miscibility Diagram for Hydrogen-Helium Mixtures. *Phys. Rev. Lett.* **120**, 115703 (2018).

55. B. Militzer, W. B. Hubbard, Ab Initio Equation of State for Hydrogen-Helium Mixtures with Recalibration of the Giant-planet Mass-Radius Relation. *The Astrophysical Journal*. **774**, 148 (2013).

56. A. Becker *et al.*, Ab Initio Equations of State for Hydrogen (H-REOS.3) and Helium (He-REOS.3) and their Implications for the Interior of Brown Dwarfs. *The Astrophysical Journal Supplement Series*. **215**, 21 (2014).

57. R. L. Kauffman *et al.*, High Temperatures in Inertial Confinement Fusion Radiation Cavities Heated with 0.35 μm Light. *Phys. Rev. Lett.* **73**, 2320–2323 (1994).

58. M. D. Rosen, The science applications of the high-energy density plasmas created on the Nova laser. *Phys. Plasmas*. **3**, 1803–1812 (1996).

59. R. E. Marshak, Effect of Radiation on Shock Wave Behavior. *Phys. Fluids*. **1**, 24–29 (1958).

60. H. N. Kornblum, R. L. Kauffman, J. A. Smith, Measurement of 0.1–3 keV x rays from laser plasmas. *Rev. Sci. Instrum.* **57**, 2179–2181 (1986).

61. E. L. Dewald *et al.*, Dante soft x-ray power diagnostic for National Ignition Facility. *Rev. Sci. Instrum.* **75**, 3759–3761 (2004).

62. J. T. Larsen, S. M. Lane, HYADES—A plasma hydrodynamics code for dense plasma studies. *Journal of Quantitative Spectroscopy and Radiative Transfer*. **51**, 179–186 (1994).

63. F. Datchi, P. Loubeyre, R. LeToullec, Extended and accurate determination of the melting curves of argon, helium, ice (H2O), and hydrogen (H2). *Phys. Rev. B*. **61**, 6535–6546 (2000).

64. D. P. Dobson, Self-diffusion in liquid Fe at high pressure. *Physics of the Earth and Planetary Interiors*. **130**, 271–284 (2002).

65. E. S. Posner, D. C. Rubie, D. J. Frost, V. Vlček, G. Steinle-Neumann, High P–T experiments and first principles calculations of the diffusion of Si and Cr in liquid iron. *Geochimica et Cosmochimica Acta*. **203**, 323–342 (2017).

66. H. F. Wilson, B. Militzer, Sequestration of Noble Gases in Giant Planet Interiors. *Phys. Rev. Lett.* **104**, 121101 (2010).

67. L. M. Barker, R. E. Hollenbach, Laser interferometer for measuring high velocities of any reflecting surface. *J. Appl. Phys.* **43**, 4669–4675 (1972).

68. P. M. Celliers *et al.*, Line-imaging velocimeter for shock diagnostics at the OMEGA laser facility. *Rev. Sci. Instrum.* **75**, 4916–4929 (2004).

69. R. E. Setchell, Refractive index of sapphire at 532 nm under shock compression and release. *J. Appl. Phys.* **91**, 2833–2841 (2002).

70. C. T. Silbernagel, P. Torres, D. H. Kalantar, in *Proc. SPIE* (2004), vol. 5559, pp. 435–442.

71. P. Datte *et al.*, in *Proc. SPIE* (SPIE, 2013; http://dx.doi.org/10.1117/12.2026893), vol. 8850, p. 88500G.

72. G. R. Labaria, A. L. Warrick, P. M. Celliers, D. H. Kalantar, in *Proc. SPIE* (2015), vol. 9345, p. 93450Q.

449 73. M. Takeda, H. Ina, S. Kobayashi, Fourier-transform method of fringe-pattern
450 analysis for computer-based topography and interferometry. *J. Opt. Soc. Am.* **72**, 156–60
451 (1982).

452 74. P. Tomassini *et al.*, Analyzing laser plasma interferograms with a continuous
453 wavelet transform ridge extraction technique: the method. *Appl. Opt.* **40**, 6561–6568
454 (December DEC 102001).

455 75. M. K. Philpott, A. George, G. Whiteman, J. De'Ath, J. C. F. Millett, The
456 application of line imaging velocimetry to provide high resolution spatially resolved
457 velocity data in plate impact experiments. *Meas. Sci. Tech.* **26**, 125204 (2015).

458 76. S. Crockett, S. Rudin, "Lithium Fluoride Equation of State (SESAME 7271)"
459 (LA-UR-06-8401, Los Alamos National Laboratory, 2006).

460 77. J.-P. Davis, M. D. Knudson, L. Shulenburger, S. D. Crockett, Mechanical and
461 optical response of [100] lithium fluoride to multi-megabar dynamic pressures. *J. Appl.*
462 *Phys.* **120**, 165901 (2016).

463 78. S. A. Bonev, E. Schwegler, T. Ogitsu, G. Galli, A quantum fluid of metallic
464 hydrogen suggested by first-principles calculations. *Nature*. **431**, 669–672 (2004).

465 79. E. Gregoryanz, A. F. Goncharov, K. Matsuishi, H. Mao, R. J. Hemley, Raman
466 Spectroscopy of Hot Dense Hydrogen. *Phys. Rev. Lett.* **90**, 175701 (2003).

467 80. S. Deemyad, I. F. Silvera, Melting Line of Hydrogen at High Pressures. *Phys.*
468 *Rev. Lett.* **100**, 155701 (2008).

469 81. M. I. Eremets, I. A. Trojan, Evidence of maximum in the melting curve of
470 hydrogen at megabar pressures. *JETP Letters*. **89**, 174–179 (2009).

471 82. H. Shimizu, E. M. Brody, H. K. Mao, P. M. Bell, Brillouin Measurements of
472 Solid n-H2 and n-D2 to 200 kbar at Room Temperature. *Phys. Rev. Lett.* **47**, 128–131
473 (1981).

474 83. W. J. Evans, I. F. Silvera, Index of refraction, polarizability, and equation of state
475 of solid molecular hydrogen. *Phys. Rev. B*. **57**, 14105–14109 (1998).

476 84. P. C. Souers, *Hydrogen properties for fusion energy* (University of California,
477 Berkeley, 1986).

478 85. M. M. Marinak *et al.*, Three-dimensional HYDRA simulations of National
479 Ignition Facility targets. *Physics of Plasmas*. **8**, 2275–2280 (2001).

480 86. P. M. Celliers, thesis, University of British Columbia, Vancouver, British
481 Columbia (1987). doi: 10.14288/1.0085458

87. P. Colella, P. R. Woodward, The Piecewise Parabolic Method (PPM) for gas-dynamical simulations. *J. Comp. Phys.* **54**, 174–201 (1984).

88. J. K. Dukowicz, A general, non-iterative Riemann solver for Godunov's method. *J. Comp. Phys.* **61**, 119–137 (1985).

89. T. S. Moss, Relations between the refractive index and energy gap of semiconductors. *Phys. Status Solidi B*. **131**, 415 (1985).

90. R. R. Reddy, S. Anjaneyulu, Analysis of the Moss and Ravindra Relations. *Phys. Status Solidi B*. **174**, K91 (1992).

91. P. Hervé, L. K. J. Vandamme, General relation between refractive index and energy gap in semiconductors. *Infrared Phys. Techn.* **35**, 609–15 (1994).

92. N. M. Ravindra, P. Ganapathy, J. Choi, Energy gap–refractive index relations in semiconductors – An overview. *Infrared Phys. Techn.* **50**, 21–9 (2007).

93. A. F. Ioffe, A. R. Regel, *Prog. Semicond.* **4**, 237 (1960).

94. M. Gurvitch, Ioffe-Regel criterion and resistivity of metals. *Phys. Rev. B*. **24**, 7404 (1981).

95. L. A. Collins *et al.*, Dynamical and optical properties of warm dense hydrogen. *Phys. Rev. B*. **63**, 184110 (2001).

96. L. A. Collins, J. D. Kress, D. E. Hanson, Reflectivity of warm dense deuterium along the principal Hugoniot. *Phys. Rev. B*. **85**, 233101 (2012).

97. M. D. Knudson, private communication (2015).

98. D. Ryutov *et al.*, Similarity Criteria for the Laboratory Simulation of Supernova Hydrodynamics. *The Astrophysical Journal*. **518**, 821 (1999).

99. R. P. Drake, *High-Energy-Density Physics Fundamentals, Inertial Fusion, and Experimental Astrophysics* (Springer, Berlin, 2006).

100. J. Clérouin, The viscosity of dense hydrogen: from liquid to plasma behaviour. *Journal of Physics: Condensed Matter*. **14**, 9089 (2002).

101. Z.-G. Li *et al.*, Benchmarking the diffusion and viscosity of H-He mixtures in warm dense matter regime by quantum molecular dynamics simulations. *Physics of Plasmas*. **24**, 052903 (2017).

102. G. Sidebotham, *Heat Transfer Modeling An Inductive Approach* (Springer, New York, 2015; http://dx.doi.org/10.1007/978-3-319-14514-3).

103. F. W. Dittus, L. M. K. Boelter, Heat transfer in automobile radiators of the tubular type. *International Communications in Heat and Mass Transfer*. **12**, 3–22 (1985).

104. D. Jo, O. S. Al-Yahia, R. M. Altamimi, J. Park, H. Chae, Experimental Investigation Of Convective Heat Transfer In A Narrow Rectangular Channel For Upward And Downward Flows. *Nuclear Engineering and Technology*. **46**, 195–206 (2014).

105. P. A. Sterne, S. B. Hansen, B. G. Wilson, W. A. Isaacs, Equation of state, occupation probabilities and conductivities in the average atom Purgatorio code. *High Energy Density Physics*. **3**, 278–282 (2007).

106. B. Holst, M. French, R. Redmer, Electronic transport coefficients from ab initio simulations and application to dense liquid hydrogen. *Phys. Rev. B*. **83**, 235120 (2011).

107. G. W. Collins *et al.*, Temperature Measurements of Shock Compressed Liquid Deuterium up to 230 GPa. *Phys. Rev. Lett.* **87**, 165504 (2001).

108. J. E. Bailey *et al.*, Time-resolved optical spectroscopy measurements of shocked liquid deuterium. *Phys. Rev. B*. **78**, 144107 (2008).

Acknowledgments We thank J. Kroll, the target fabrication team at LLNL and the NIF operations crew for experimental support. **Funding:** This work was performed under the auspices of the U.S. Department of Energy by Lawrence Livermore National Laboratory under contract DE-AC52-07NA27344, Lawrence Livermore National Security, LLC. This material is based upon work supported by the Department of Energy National Nuclear Security Administration under Grant No. DE-NA0001944, the University of Rochester, and the New York State Energy Research and Development Authority. RSM acknowledges support from EPSRC under Grant No. Ep/P024513/1. AFG acknowledges support the Army Research Office (56122-CH-H), the National Natural Science Foundation of China (21473211), and the Chinese Academy of Science (YZ201524). RJ acknowledges support from DOE/NNSA (including DE-NA0003607) and the University of California. **Authors contributions**: RSM, RJ, RJH, GWC, PMC, MM, SB, PL, JRR, AFG and JHE conceived the experiments; JLP, NBM, PMC, MM, DEF and SB designed the experiments; PMC, MM, SLP, SB, DEF and AFG executed the experiments; PMC, SB, MM and RSM analyzed the data and performed post-shot simulations; PMC, RJH, RSM, MM and RJ wrote the manuscript; all authors reviewed and discussed the manuscript during preparation. **Competing interests**: All authors declare no competing interests. **Data and materials availability:** all data is available in the manuscript or the supplementary material.

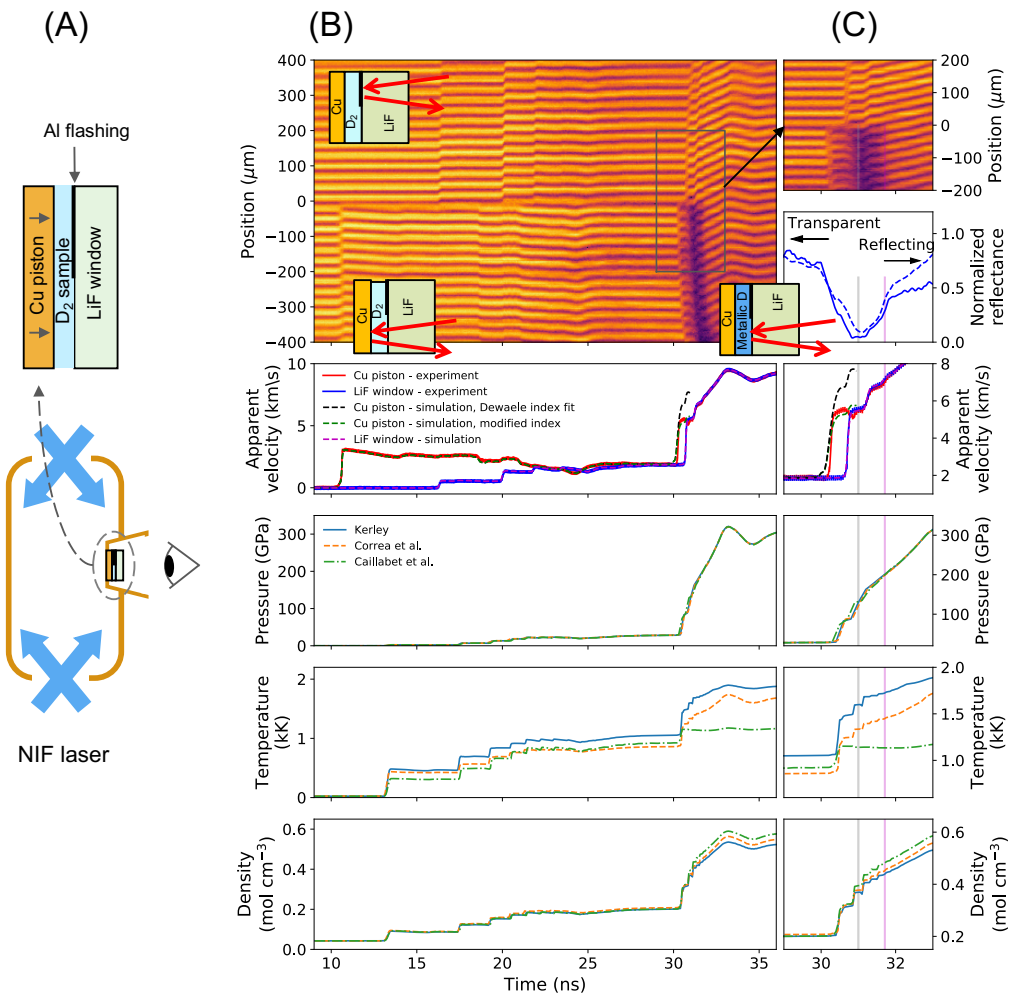

Fig. 1 Schematic of target and experiment together with raw data. (A) A planar sample layer of liquid deuterium, 31 μm thick, contained between a 70 μm thick copper piston and a 500 μm thick LiF window is mounted onto the side of a hohlraum (brown in bottom sketch), driven with the NIF laser (blue block arrows) and diagnosed with a line-imaging VISAR (sensor positioned on right). (B) Example data record from experiment N150914-2: fringe amplitude encodes reflectivity and fringe phase is proportional to the Doppler shift of the reflected light (piston and window interface velocities); the frame below shows apparent velocity signals extracted from the fringe phase and corresponding simulated velocities. At times $30 < t < 31$ ns simulations (black dashed) with the extrapolated Dewaele *et al*. (*35*) refractive index fit do not match the observations and require a corrected index (green dashed) to match observations; additional frames below show pressure, temperature and density at a point in the center of the sample estimated from simulations matched to the velocity data based on three different equation of state models for deuterium. (C) Details of the information presented in (B) with magnified time axis: vertical gray lines denote the transition from partially transparent to opaque; vertical magenta lines indicate the time when the reflectivity at the D/LiF interface exceeds 30%. The normalized reflectance shows independent measurements from the two detectors.

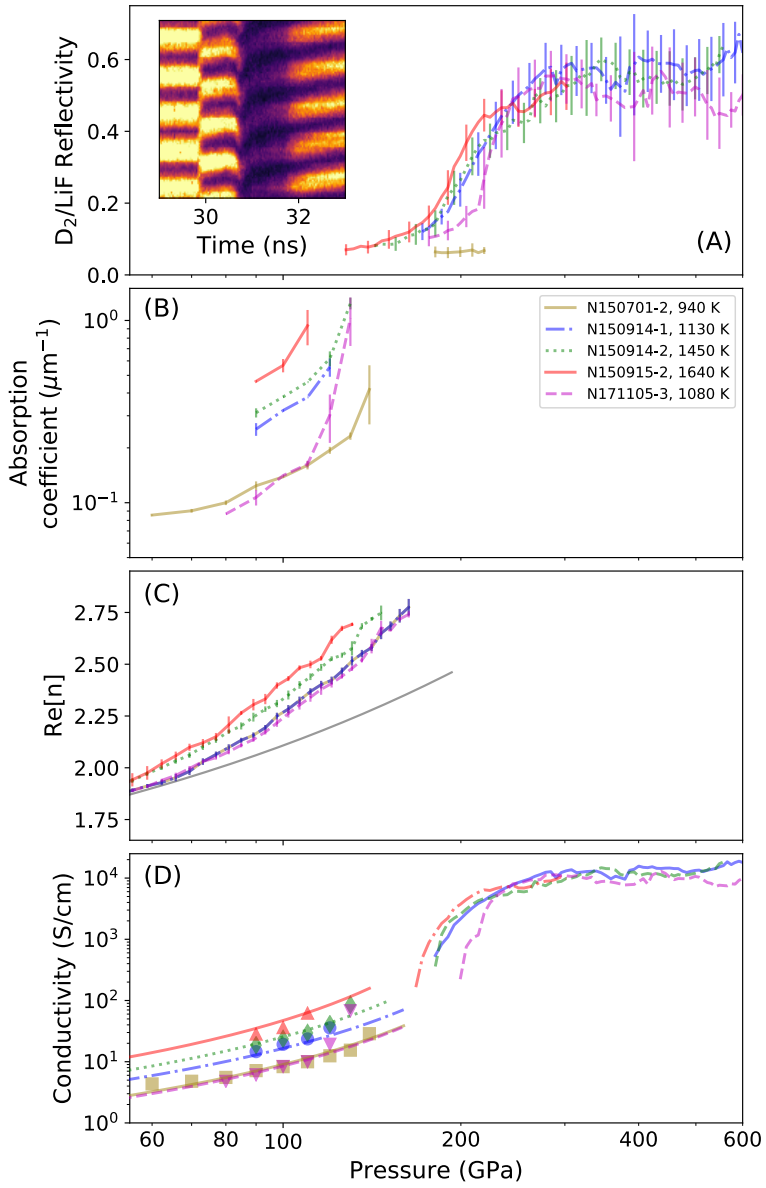

Fig. 2. Optical signatures of the insulator-metal transition. Curves in all frames are matched for the five experiments following isentropes that correspond to the colored *T*-*P* bands in Fig. 3. (B) Absorption coefficient, legend indicates experiment number and *T* along isentrope near $P = 200$ GPa (C) Index of refraction from simulations matched to the observed Doppler shifts (symbols); and, for comparison, extrapolation of the Dewaele *et al*. (*35*) refractive index fit to higher density (solid gray curve). (D) For $P < 150$ GPa, optical (AC) conductivity as extracted by combining the data in (B) and (C) (symbols) and corresponding Lorentz model fits (curves); for $P > 150$ GPa the DC conductivity inferred from the reflectivity data in (A) and the Smith-Drude model with $\tau = 0.075$ fs (*30*). Inset in (A): raw data from N171105-3, showing a sharp reflectivity jump just before $t = 32$ ns.

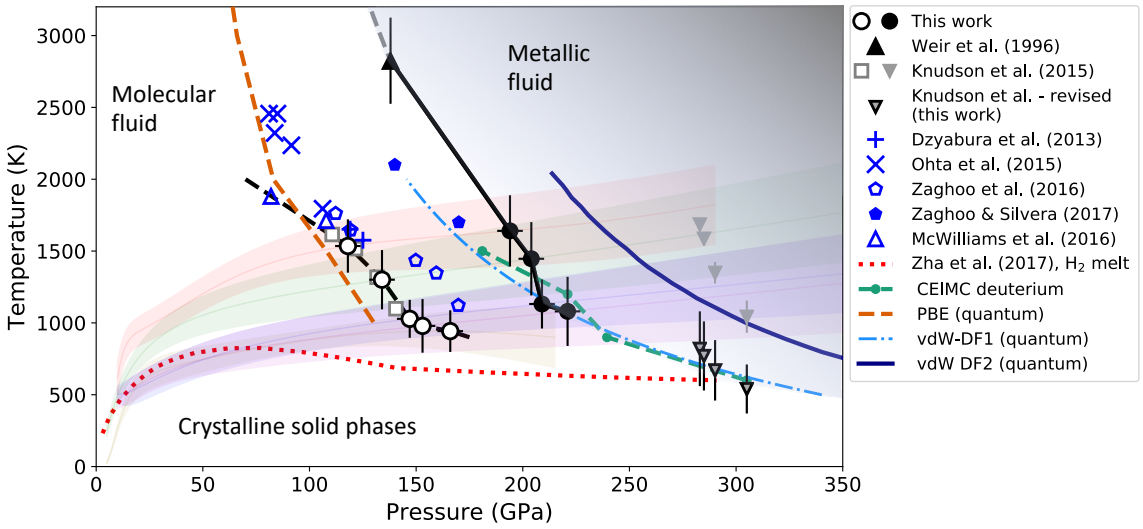

Fig. 3 Phase diagram of H_2/D_2 at high *P-T* conditions. Present results: threshold where optical absorption coefficient exceeds ≈1 μm^{-1} at 660 nm and the band gap is ≈ 2eV (black open circles connected by thick dashed line); and, points where the D/LiF interface reflectivity exceeds *R*=30% (black solid circles), corresponding to the minimum metallic conductivity $\sigma \approx 2 \times 10^3$ S/cm. The thick black curve connects these points to the metallization transition, $\sigma \approx 2 \times 10^3$ S/cm, identified by Weir *et al*. (solid black triangle) (*10*). The colored solid curves and associated bands show the compression paths of the current experiments (shading indicates estimated systematic uncertainty). Previous experimental results on H_2: Ohta *et al*. (x) (*18*) and Dzyabura *et al*. (crosses) (*17*) both from heating curve analyses of in laser-heated DACs; Zaghoo *et al*. (open pentagons) from absorption and reflectance in laser-heated DAC (*19*); McWilliams *et al*. (*20*) determination of the onset of absorption from transient DAC optical transmission measurements (open triangles); Zaghoo & Silvera (*21*) reflectance saturation data (solid pentagons); melting measurements of Zha *et al*. (*23*) (dotted red). Previous results on D_2: Knudson *et al*., absorption onset for 532 nm wavelength (open squares) (*22*) Knudson *et al*., reported IM transition (inverted gray triangles) (*22*) and revised with our interpretation (inverted black-edged triangles). A selection of theoretical curves reported in Pierleoni *et al*. (*15*) compares results from three DFT exchange-correlation functionals: PBE (dashed orange), vdW-DF1 (chain-dash blue) and vdW-DF2 (solid blue) and the CEIMC calculation for deuterium (dashed green).

Supplementary Materials for

Insulator-metal transition in dense fluid deuterium

Peter M. Celliers,[1] Marius Millot,[1] Stephanie Brygoo,[2] R. Stewart McWilliams,[3] Dayne E. Fratanduono,[1] J. Ryan Rygg,[4,1] Alexander F. Goncharov,[5] Paul Loubeyre,[2] Jon H. Eggert,[1] J. Luc Peterson,[1] Nathan B. Meezan,[1] Sebastien Le Pape,[1] Gilbert W. Collins,[4,1] Raymond Jeanloz,[6] Russell J. Hemley[7]

[1] Lawrence Livermore National Laboratory, Livermore, CA 94550, USA
[2] CEA, DAM, DIF, F-91297 Arpajon, France
[3] School of Physics and Astronomy and Centre for Science at Extreme Conditions, University of Edinburgh, Peter Guthrie Tait Road, Edinburgh, United Kingdom EH9 3FD
[4] Department of Mechanical engineering, Physics and Astronomy and Laboratory for Laser Energetics, University of Rochester, Rochester, NY 14623, USA
[5] Carnegie Institution of Washington, Washington, DC 20015, USA
[6] University of California, Berkeley, CA 94720, USA
[7] The George Washington University, Washington, DC 20052, USA

correspondence to: celliers1@llnl.gov

This PDF file includes:

Materials and Methods

Target configuration

The experimental platform consists of a cylindrical Au hohlraum that serves as a blackbody radiation cavity, with a target package mounted on the side (Fig. S1). The hohlraum dimensions are 10.9 mm long by 6.2 mm diameter with 3.6 mm diameter laser entrance holes (LEHs) in each end. The sample package is placed over a 2 mm diameter hole in the side of the hohlraum and is contained within a 3 mm long Au cone to allow diagnostic viewing down the axis of the cone. The sample package consists of a Cu plate 2 mm diameter x 70 μm thick acting as the piston and a LiF window 1 mm square x 500 μm thick. These components are assembled to leave a 30 - 32 μm gap between the LiF window and the Cu piston. The sample volume is sealed with a quartz window and attached to a supply of high purity deuterium gas through capillary lines. The hohlraum is attached to mounting arms at the top and bottom and additional shielding components are placed around the hohlraum (Fig. S2). Shields around the arms holding the hohlraum disperse unfocused and unconverted laser light (at 527 nm and 1053 nm), and a large conical shield extending out to 50 mm radius from the target maintains a plasma-free optical line-of-sight for the velocimetry diagnostic viewing the target package. The completed assembly is mounted onto a cryogenic cold finger and cooled to a temperature of 21.5 K.

Shortly prior to the experiment the sample volume is filled with liquid deuterium at a pressure of 820 torr. The interior of the hohlraum is also sealed and filled with He gas at a pressure of 200 torr. The He gas is confined using thin (40 nm) polyimide windows to seal the LEHs. The He gas limits the rate and range of expansion of the Au hohlraum walls into the interior of the hohlraum volume during the experiment. The polyimide windows are destroyed by the laser drive beams during the first few dozen picoseconds of the experiment.

Laser power and radiation drive

Most beams of the NIF laser are directed through the laser entrance holes to heat the interior was of the hohlraum with a precisely defined power as a function of time. Of the available 192 beams 168 are active (24 beams are inactive to avoid striking the sample package). The power is delivered in two parts, with half of the beams delivering the early part of the pulse and the other half the later part (the dividing time is evident in the power transients at 15 and 23 ns seen in Fig. S3). The heated hohlraum walls absorb and re-emit the power deposited by the laser to form a high temperature thermal radiation bath within the interior of the hohlraum (*57, 58*). The resulting thermal radiation flux drives an ablative Marshak radiation wave (*59*) into the walls of the hohlraum and into the Cu piston. The ablation process creates a pressure wave that outruns the radiation wave and accelerates the Cu plate, causing it to act like a piston to compress the sample. The temporal history of the radiation temperature in the hohlraum is recorded by the DANTE radiation temperature diagnostic (*60, 61*). The DANTE data show that peak temperature reached 140 eV for the first experiment and 165 eV for the following four experiments. Also evident in Fig. S3 is the variation in the initial power of the pulse (the "picket"). This initial burst of power launches a weak shock (20 - 40 GPa amplitude) into the Cu piston, which in turn is transmitted into the deuterium sample at much lower amplitude (ranging from 1.5 GPa to 3 GPa) because of the impedance mismatch between the Cu and

the deuterium. This shock deposits most of the entropy into the sample layer, thereby determining the average temperature of the sample upon subsequent compression. Stronger initial shocks lead to higher temperatures upon compression. The late-time peak pressure is determined by the peak temperature in the radiation drive. Our first experiment reached a peak pressure of about 215 GPa, while the subsequent three experiments reached ~550 GPa. The drive pressure scales as a high power (~4) of the radiation temperature. The details of this scaling depend on the radiative properties of the ablated gold and copper plasmas expanding from the surfaces of these components.

As the x-ray spectrum emitted by the hohlraum is approximately Planckian its spectrum peaks near 2.8 times the temperature, or < 500 eV for our experiments. Consequently, emission of photons harder than 2 keV is negligible. The deuterium sample and the accompanying LiF window are shielded by thick layers of Cu (80 μm) and Au (≥ 100 μm) that block the hohlraum radiation from affecting the sample.

Compression History

Compression of the deuterium layer is accomplished through a combination of reverberating shock waves, followed by a smoother pressure increase once the layer is compressed to a few microns thickness. A radiation-hydrodynamic calculation (Fig. S4) using the HYADES code (*62*) shows the basic features of the compression process. It takes about 10 ns for the initial shock in the Cu layer to reach the Cu/deuterium interface (time t_1). Initial compression of the deuterium starts with this event, which initiates a reverberation sequence in the layer. A release wave launched at time t_1 travels back through the Cu piston to the ablation surface arriving at t_2. Starting at t_2 a recompression wave is launched in the Cu by the increasing drive pressure, reaches the deuterium layer at t_3, and produces a second fast reverberation sequence. After several reverberations of the second sequence compression becomes continuous. The IM transition starts after t_3. Curves showing the pressure, the density and the thickness of the layer are also shown. Near the IM transition the layer thickness reaches ~2.8 μm and 2 g cm^{-3} (0.5 mol cm^{-3}). At peak compression (near 550 GPa) the density reaches ~2.8 g cm^{-3}, and the layer thickness is ~1.9 μm.

Detailed profiles of the density, pressure, temperature and sound speed at several times near the IM transition are shown in Fig. S5. While conditions in the surrounding Cu and LiF are non-uniform, the deuterium sample layer is compressed to near-uniform conditions. This is helped by the high sound speed in the sample (> 15 km/s) and relatively small layer thickness.

Details of the two reverberation sequences in the sample layer are highlighted (Fig. S6) in lagrangian coordinates. The transmitted first shock strength in the deuterium layer has amplitude spanning 1.6 GPa to 2.6 GPa over the 5 experiments. The first shock reverberates approximately 4-5 times before the pressure reaches a nearly constant level between 20 and 32 GPa; this occurs over a period of about 15 ns. The second compression wave from the Cu piston raises the pressure to between 50 and 80 GPa (depending on experiment), with further increases through subsequent reverberations. Above about 200 GPa the pressure rise is continuous.

The insulator-metal (IM) transition occurs during the second sequence, somewhere between 150 and 250 GPa. Because of the reverberations the pressure increase over much of this range occurs discretely in about 5 or 6 steps. Furthermore, the transit times

of each reverberation are sub-nanosecond in duration, starting at ~450 ps, and diminishing to ~150 ps as the layer compresses and the sound speed increases. For most of the experiments the time resolution of our detection system was about 150 ps, comparable to the transit times of the final reverberations. These experiments were not able to discriminate easily between an abrupt (first order) transition from insulator to metal and a continuous transition. While the analyzed results have the appearance of a continuous transition, we cannot rule out a first order transition because of the discrete nature of the compression steps and the finite time resolution of the measurements. On one experiment it with ≈50 ps time resolution we did observe a sharp transition (Fig. 2 inset).

Sample containment and the optical interface

Hydrogen is known to escape from diamond anvil cells at high temperature and pressure via diffusion into the gasket materials on time scales of seconds or longer (*63*); however, quantitative data on mass diffusivities at the relevant conditions are sparse. Available values for mass diffusivities in pressurized and heated Fe (*64*, *65*) are many orders of magnitude too low for bulk diffusion (sample escape) to occur in a few nanoseconds. Assuming that mass diffusivity in Cu and LiF are of similar order of magnitude it is highly unlikely that the sample can escape through diffusion into the containing materials during the few nanoseconds duration of the experiments.

We also considered chemical reaction with the LiF window. Calculated temperatures of the LiF at the D_2/LiF interface are < 1000 K over the duration of the experiment. The most plausible contamination, a layer of pressurized LiD and DF formed at the optical interface through chemical reaction is likely to be dielectric at T < 1000 K, with low conductivity, and therefore would behave like an optical coating. However, the ambient pressure enthalpy of formation of LiF (-620 kJ/mol) compared with LiH (-91 kJ/mol) and HF (-15 kJ/mol) prohibit such reactions for energetic reasons and make it unlikely that they could occur at pressure in the short time scales of the experiment. LiF is a remarkably stable wide-bandgap dielectric material at high pressure with band gap estimated to exceed 8 eV (*41*) over the entire pressure range of our experiments. The electronic configuration is closed shell, the same as the configuration of He and Ne. Ne, like He, is immiscible in liquid metallic hydrogen at low temperature and high pressure (*66*). In order to affect the optical reflectivity an interface perturbation must extend over a good fraction of a wavelength of the light, i.e. more than 35 nm, and change the dielectric properties drastically (optical conductivity). We see no evidence of optical degradation of the D_2/LiF interface during the first reverberation sequence leading up to the IM transition, and our IM transition observations are completed within a time duration of 3 ns after the second reverberation starts. The experiments of Knudson *et al.* (*22*) showed reversible reflectivity signals during an experimental duration of > 300 ns, suggesting that any chemical reactions or diffusion, if present, occurs on much longer time scales.

Diagnostic configuration

The primary diagnostic is a line-imaging velocity interferometer system for any reflector (VISAR) (*67, 68*). In this arrangement a beam of laser light is directed onto the target, and the reflected beam is relayed back through an imaging system that projects the

target image onto the slit of a streak camera after passing through the interferometer. The target image is split into two parts (Fig. S7): one part views through the LiF window and reflects from the Cu piston; in the other part the light is reflected from a 100 nm thick Al flashing coated onto the LiF window located at the interface between the LiF and the deuterium sample. LiF is known to remain transparent up to at least 800 GPa under quasi-isentropic or ramp compression (*41*).

The light source is a single frequency (single longitudinal mode) Nd:YAG laser operating at 1319 nm, frequency doubled to 659.5 nm. The light is conveyed to the diagnostic through a multi-mode optical fiber conduit and formed into a beam with collimating optics, then coupled into the line-of-sight with a 50% beam splitter. The power delivered to the target was < 12 kW. At the target the beam is focused to a diameter of approximately 2 mm forming a spatially uniform multi-mode (speckled) pattern with irradiance < 380 kW/cm^2. This power level is insufficient to raise the temperature of a skin depth layer of metallic deuterium by a significant amount during our measurements. Assuming a typical specific heat capacity of metallic deuterium of 6 J/g/K, density of 2 g/cm^3 and skin depth of 50 nm, the rate of temperature rise in the absorbing layer (assuming 100% absorption) is < 6.4 K/ns. The transition from insulator to metal occurs in less than 3 ns. The maximum temperature rise expected from the probe laser during this time, ~20 K, is much less than our uncertainty in the layer temperature.

Superimposed on the image returned through the image relay system is a sinusoidal fringe pattern (sinusoidal intensity as a function of position) created by passing the light through the VISAR interferometer (Fig. S8). Within the interferometer one sample beam is delayed in time relative to the other (148 ps in one interferometer channel, 59 ps in a second interferometer channel). The recombined sample beams are overlapped to reform the image along with the resulting fringe pattern. A Doppler shift in the reflected light beam is manifested as a shift in the phase of the fringe pattern in linear proportion to the Doppler shift. Because the signal is captured at an image plane, the phase shifts are localized in both space and time. Rather than referring to the Doppler shift in frequency units we refer to it in terms of "apparent velocity", by which we mean the velocity of a reflector moving through vacuum that produces an equivalent signal. Thus, the raw data captured by the streak camera provides a space- and time-resolved recording of the apparent velocities of reflecting interfaces within the target.

Since our targets contain refracting media, the apparent velocity is not the same as the actual velocity of the reflecting interface. The observed Doppler shift is proportional to the rate of change of total optical path between the probe source and the detector:

$$v_{\text{apparent}}(t) = \frac{d}{dt} \int_{\text{path}} n(x,t)dx, \qquad (1)$$

which is usually larger than the actual velocity. The actual velocity can be extracted by applying corrections that account for the refractive indices in the transparent media traversed by the probe beam (*67*, *69*).

It is common with VISAR arrangements to have at least two interferometers and detectors record a common reflected light signal (*68*). Each interferometer is configured with a different sensitivity (referred to as velocity-per-fringe or VPF). In many cases the data contains shifts of several cycles; the integer portion of the phase shift (measured in

cycles) cannot be inferred purely from analysis of a single interferometer pattern, and requires additional information. With two interferometers this ambiguity is easily resolved. The VPFs of our dual interferometer setup were 2.186 km/s/fringe and 5.460 km/s/fringe respectively.

Data reduction – camera corrections

Prior to analysis basic manipulations are applied to the data sets including: background subtraction, two-dimensional distortion correction and sweep linearization. The distortion correction removes electron-optic image distortions from the output image. Most of the distortion is removed using a distortion map created by off-line calibration with a picosecond laser source and an etalon which projects a precise pattern of light impulses forming a space-time grid onto the camera input (*70*). Secondary correction is generated in-situ 1 to 2 hours prior to the experiment (Fig. S9) using a high precision 0.5 GHz or 1 GHz laser comb generator source to project a similar signal onto a set of ten spatial locations across the slit (*71*, *72*). The two outer comb generator signals are always recorded simultaneously with the data on each edge of the data region. These signals are used to correct residual fluctuations in sweep rate and/or linearity that can occur on a sweep-to-sweep basis. An additional light impulse that is precisely synchronized to the facility timing system is also recorded on the camera to provide an absolute timing reference relative to the laser drive, and to other diagnostic equipment. Experience with this suite of corrections over hundreds of NIF experiments confirms that the corrections map the raw data onto a Cartesian space-time coordinate system with a relative accuracy of ~0.3% of the respective spatial window (3 μm out of 1 mm) and 0.3% of the temporal sweep window (< 0.12 ns out of 40 ns), with absolute accuracy of < 100 ps relative to the NIF clock.

Data reduction – phase and velocity extraction

The apparent velocities of the reflecting interface(s) in the target are determined from the instantaneous phase of the fringe pattern. We have applied two methods to extract the phase: (i) a variant of the Fourier transform method (FTM) developed by Takeda *et al.* (*73*, *68*); and, (ii) a technique based on ridge extraction from a continuous wavelet transform (CWT) of the data (*74*, *75*). Both techniques provide a global extraction of the velocity over the entire data set, allowing the generation of two-dimensional phase and amplitude maps. Both techniques give near identical results for the apparent velocity, aside from minor differences in the noise levels. For the reflectance and absorptivity analysis presented below we chose the CWT technique because of its superior immunity to noise sources in the raw data.

The analysis tools that extract the fringe phase (FTM or CWT) produce a complex-valued result, $Z(x,t) = A(x,t)\exp(i\varphi(x,t))$. From this complex-valued signal we can extract the phase: $\varphi(x,t) = \tan^{-1}[\mathrm{Re}(Z), \mathrm{Im}(Z)]$; and the amplitude, $A(x,t) = |Z(x,t)|$.

Data reduction – velocity map

The fringe patterns span about 35 fringes in our data sets, corresponding to a background phase ramp. The velocity map is obtained after subtracting the phase ramp and multiplying the resulting phase (measured in cycles) by the VPF. The ramp subtraction is achieved by subtracting a blank (or reference) fringe pattern obtained on

the streak camera shortly before the experiment; this method removes residual distortions present in the interferometer and camera systems. Discontinuities in the fringes at specific event locations are treated specially to allow for jumps of multiple fringes in some cases. The fringe jumps are resolved by comparing the analyses of the data from the two interferometers and choosing jumps that produce matching results. The raw phase ramp extracted from the data record shown in Fig. S8 and wrapped to the interval [-π, π] is shown in Fig. S10A and the corresponding velocity map in Fig. S10B.

Data reduction – reflectance map and reflectivity

The CWT and FT methods for fringe analysis provide a two-dimensional field $Z(x,t) = A(x,t) \exp(i\varphi(x,t))$ from which we extract the reflectance from the fringe amplitude $A(x,t) = |Z(x,t)|$ (Fig. S11). By using the fringe amplitude signal rather than the total light intensity the analysis is immune to DC frequency bias (background); however, it is sensitive to changes in fringe visibility that are most evident during velocity transients when the detector cannot resolve the rapid fringe motion. The upper half of the recording provides the reflected signal from the Al/LiF interface. We use this signal as a normalization reference for the portion of the signal reflected from the Cu piston and transmitted through the deuterium sample.

The reference signal is observed gradually to decrease over the duration of the recording, due to increasing optical absorption as the compression wave propagates through the LiF window. The increasing absorption is likely related to heating and mechanical deformation of the material (generation of optically active color centers and lattice defects) and also because the amount of compressed LiF entrained in the compression wave increases approximately linearly with time. The material becomes hot (several thousand K) under the isentropic compression of the steepening pressure wave. A strong leading shock eventually develops and attains a strength up to several hundred GPa rendering the window optically opaque. A thin layer of LiF adjacent to the deuterium sample remains cool because its compression path most closely approximates an isentrope starting from cryogenic conditions. With the assumption that the window effects are uniform over the field of view the absolute reflectance can then be obtained by assuming a fixed value for the Al/LiF interface reflectivity.

The reflectance signal from the Cu piston region can be divided into two time domains according to whether a difference in apparent velocity is observed on the Cu piston side of the target as compared to the Al/LiF window side (Fig. S12). While the deuterium layer remains transparent, or partially transparent, the velocity signal returned from the Cu piston will be different from that of the window. That is because the Cu piston and LiF window are separated by the compressible layer of deuterium, and transient events experienced by either surface are communicated to the other by weak shocks or acoustic waves, resulting in different velocity histories. At some time, t_M, during the experiment the reflection of the probe light shifts from the Cu piston to the deuterium-LiF interface. For $t > t_M$ the two apparent velocity signals match each other, indicating that they originate from a common interface, the pressurized deuterium-LiF window interface. For $t \leq t_M$ the reflectance signal is decreasing with time and is interpreted in terms of the intrinsic reflectivity of the Cu piston and optical transmission through the partially absorbing deuterium sample layer; we can estimate the absorption coefficient in the deuterium sample layer from this signal, described below. At time t_M

the normalized reflectance signal reaches a minimum, typically near 0.10 (relative to the Al/LiF reflectivity). The reflectance is not expected to reach zero because the deuterium refractive index at these conditions exceeds 2.5 even when the deuterium layer is not metallized. The refractive index of the pressurized LiF is around ~1.5 at these conditions leading to a minimum reflectivity $R \approx 10\%$, consistent with the reflectivity expected from the Fresnel formula (also accounting for the increased refractive index discussed later in 4(a)).

For the times $t > t_M$ the reflectivity of the deuterium-LiF interface was obtained from the normalized reflectance map by assuming a fixed value for the reflectivity of the Al/LiF interface. The spectrally-dependent reflectivity of the pressurized Al/LiF interface was computed by Knudson *et al*. (*22*) to be $R_{\mathrm{Al/LiF}} = 0.78$ at our probe wavelength 659.5 nm; to extract absolute reflectivity we scaled the reflectance by this value. After applying this normalization the reflectance map and the velocity maps were analyzed on a pixel-by-pixel basis, for which each pixel has a reflectance value and an apparent velocity value associated with it. These data were assigned into velocity bins of width 0.04 km/s to form a histogram of the reflectivity versus apparent velocity over the entire data set. Within each bin the average and standard deviation of the reflectance values are used to determine the reflectance and assess the statistical measurement error. We converted apparent velocity to pressure by assuming a window correction for the velocity of 1.295 (i.e. $u_{\mathrm{LiF}} = u_{\mathrm{Apparent}}/1.295$) and the known principal isentrope from the SESAME 7271v3 equation of state model for LiF (*76*, *77*).

Data reduction – temporal dependence of reflectance

The assignment of reflectivity to velocity bins removes information about the temporal dependence of the signal. The time history of pressure experienced by the sample layer was in fact not monotonic at times above the IM transition. The details of the time history experienced by the sample in experiments 2 and 3 are shown in Fig. S13, encoded by the colors of the filled circles. These points were extracted from spatially-averaged lineouts across the sample, with each point corresponding to a particular observation time in the sample. From the figure it is evident that the pressure loading initially passed though the IM transition at early times until reaching approximately 300 GPa, then dwelling for a few ns at a near constant (but slightly oscillating) level. At later times the pressure rapidly increased to its peak value above 500 GPa and then subsequently relaxed back down to near 300 -400 GPa. The signal was cut off at this point because of the eventual steepening of the pressure wave in the LiF window into a strong shock. Evidently the apparent reflectivity of the D/LiF interface is independent of time-dependent effects on the time scale of the experiments (~15 ns). This observation contrasts with the time-dependent reflectivity observed in the experiment of Knudson *et al.* (*22*) In their interpretation Knudson *et al.* attributed the time dependent effects to heat transport at the D_2–LiF interface. In the current experiments times scales are apparently too short for such effects to play a significant role. We return below to discuss the significant differences in heat transport in our experiments compared with those on Z.

Data reduction – absorption coefficient

The absorption coefficient can be estimated from the reflectance signal for $t \leq t_M$ and knowledge of the thickness of the deuterium layer as a function of time. The

normalized reflectance $r_n(t)$ is related to the absorption coefficient in the deuterium layer through the equation,

$$r_n(t) = \frac{R_{\mathrm{Cu}}}{R_{\mathrm{Al/LiF}}} \exp[-2\kappa L(t)] + \frac{R_{\mathrm{D2/LiF}}(t)}{R_{\mathrm{Al/LiF}}}, \quad (2)$$

where R_{Cu}, $R_{\mathrm{Al/LiF}}$ and $R_{\mathrm{D2/LiF}}(t)$ are the reflectivities of the Cu piston, the Al/LiF and D_2/LiF interfaces, respectively, κ is the absorption coefficient and *L(t)* is the layer thickness. The second term accounts for the optical reflection from the deuterium-LiF interface. Solving for the absorption coefficient gives,

$$\kappa(t) = -\frac{1}{2L(t)} \log\left[\frac{r_n(t)R_{\mathrm{Al/LiF}} - R_{\mathrm{D2/LiF}}(t)}{R_{\mathrm{Cu}}}\right]. \quad (3)$$

The time dependent *L(t)* must be extracted from a simulation model matched to the observed velocity histories (see below); the model includes the refractive indices of the pressurized deuterium and the LiF window, from which the optical reflectivity $R_{\mathrm{D2/LiF}}(t)$ can be estimated with the Fresnel formula. Additionally it provides the average density $\rho(t)$, temperature *T(t)* and pressure *P(t)* history so that $\kappa(t)$ can be related to the thermodynamic state of the sample. In our analysis assumes $R_{\mathrm{Cu}} = 0.95$ and $R_{\mathrm{Al/LiF}} = 0.78$. At the time when the reflectance signal reaches its minimum, $r_n \approx 0.07$, the layer thickness is *L*~3 μm, and $R_{\mathrm{D2/LiF}}(t)$ has a comparable magnitude. This limits the maximum value of the absorption coefficient that can be determined. For example when the two terms in (2) are nearly balanced then the layer has OD ≈ 1.4 (double-passed OD ≈ -log(0.07) ≈ 2.7), and $\kappa \approx 1.4/(3\ \mu\mathrm{m}) \approx 0.5\ \mu\mathrm{m}^{-1}$. Values of κ much larger than 1 $\mu\mathrm{m}^{-1}$ are not possible to determine because $R_{\mathrm{D2/LiF}}(t)$ (the second term in eq. 2) begins to dominate. Fig. S14 shows an example result.

Simulation modeling

Thermodynamic states in the sample were inferred from simulations matched accurately to the observed apparent velocity signals. In the simulation a boundary condition with a prescribed velocity and temperature history is applied to the deuterium sample acting as a source of pressure and heat to account for the effects of the Cu piston. We determined the time history of the pressure (or equivalently the Cu piston velocity) applied to the sample layer using an iterative procedure designed to converge on the observed apparent velocities of both the Cu piston signal and the Al-LiF interface signal. The converged simulations determined the spatial and temporal history of the pressure *P(t)*, density $\rho(t)$ and the temperature *T(t)* in the sample layer. The Cu piston temperature increases during the experiment because it undergoes shock compression, followed by decompression and then a second shock compression (Fig. S5). To account for this our model estimates the penetration of heat originating from the piston surface into the sample layer by solving the heat equation self-consistently with the fluid motion. Further details of the heat penetration model are given below.

Equation of state models

The simulations require accurate tabular equation-of-state models for deuterium and LiF. We used three equation of state models for deuterium: the models of Kerley (*31*), Caillabet *et al.* (*32*) and Correa *et al.* (*33*) The Caillabet et al. (*32*) and Correa et al. (*33*) models are based on DFT calculations with the Perdew-Burke-Ernzerhof (PBE)

exchange-correlation functional (*44*). In both cases the DFT results are fitted with physically-motivated free-energy forms in order to generate wide-range tabular models, but implementation details are different. The Kerley model developed prior to more recent calculations (*78*, *28*) and experiments (*23*, *24*, *79–81*) is based on a chemical picture construction; it does not represent the melt physics accurately (melt curve maximum near 5000 K and 350 GPa), implying that the compression paths are situated entirely in the molecular solid phase. None of the models attempt to represent the first order IM transition, although the Caillabet *et al.* and Correa *et al.* models do show $dT/dP < 0$ along isentropes near the IM transition, which is a manifestation of the metallization transition. Recent accurate benchmarking data for the deuterium and hydrogen EOS based on shock measurements are available from Brygoo *et al.* (*34*) (based on an earlier work by Loubeyre *et al.* (*12*)) and also from Knudson & Desjarlais (*29*). A comparison with the Brygoo *et al.* results is summarized in Fig. S15. Similar comparisons are in Fig. 2 of Knudson & Desjarlais (*29*) for the Kerley and PBE-based principal Hugoniots (as well as other functionals and a QMC calculation). All the models represent the density compression and shock temperatures close to the available benchmarking data over a wide range of states at 5 kK $< T <$ 40 kK and $0.12 < \rho_M < 0.3$ mol/cm^3, but with some systematic differences. By construction, all of the models are fitted to available static compression data (cold curve data), so the low T EOS is also accurate. No benchmarking T data exist at $1 < T <$ 5 kK where the models produce differing results. We use the spread in T among the three models (standard deviation) to provide a conservative estimate of the systematic uncertainty in T.

For the LiF window we used the recently developed SESAME 7271v3 table for LiF (*76*, *77*) which was developed specifically to match accurate benchmarking data along the Hugoniot, and ramp compression paths to 350 GPa. The conditions in the LiF window at the IM transition are well within the validity range of this recent calibration.

Refractive index models

Optical models giving the density and temperature dependence of the index of refraction for *both* the LiF window and deuterium layer are required to relate the dynamic state (interface velocities) to the observed Doppler shifts in the reflected light signals; these are needed to evaluate equations (3a) and (3b) below.

For the LiF refractive index we used the calibration developed by Rigg *et al* (*42*) and extended by Knudson *et al.* (*22*) and J.P Davis *et al.* (*77*) This model is primarily density-dependent with a correction for temperature effects. For the index of refraction of deuterium we use the Gladstone-Dale fit for fluid hydrogen reported by Dewaele *et al.* (*35*) which assumes a linear dependence of index with molar density. This calibration is valid up to a density of 0.23 mol/cm^3 (~0.93 g/cm^3 for deuterium) and is consistent with previous data sets collected with static techniques (*82*, *83*). A similar fit was published by Souers (*84*) with a density coefficient that is about 3% different (the Souers book predates the Dewaele *et al.* study by about 17 years). Our experiments approach 0.5 mol/cm^3 (2 g/cm^3) before the deuterium sample becomes opaque, thus requiring an extrapolation of the known density dependence. The data indicate that a simple linear extrapolation is not accurate, and a correction beyond linear is needed at high densities. Details of this correction are given below.

Hydrodynamic codes

We used several codes for simulating the experiments. The inertial confinement fusion code HYDRA (*85*) was used in 2D mode for initial modeling of the hohlraum radiation drive. The radiation hydrodynamics code HYADES (*62*) and HYDRA in 1D mode and were both used for modeling the motion of the target package in order to design the laser pulse shape (as in Fig. S4). For detailed matching to the experimental observables we used primarily the code LTC (*86*), and cross-checked those results against similar optimizations performed with HYDRA in 1D. In LTC the numerical solution is based on a Lagrangian mesh and the equations of motion are integrated using the piecewise-parabolic-method (*87*) incorporating the Riemann solver of Dukowicz (*88*). All of these codes can be configured to use the EOS models described above. We found agreement among results computed with all of them, despite differences in the details of the numerical methods. For the matching calculations we used a computational mesh of 55 zones for the D_2 layer and 447 cells for LiF, with feathering in the LiF layer to match zone masses at the D_2/LiF interface. We checked convergence by performing several cases at twice the resolution and found differences well within error bars.

Matching algorithm

The hydrodynamic calculation solves the equations of motion of the deuterium layer and the LiF window in one-dimensional plane-parallel geometry subject to a boundary condition for the velocity of the Cu piston on one side, and the pressure at LiF window boundary at the side opposite to the LiF/D2 interface. At each time step the computational mesh captures both the dynamic state (velocities and positions) and thermodynamic state (temperature, density, pressure and internal energy) of the two media. The density and temperature profiles are required to determine the refractive index of both layers based on the calibrated models. The goal is to determine the time history of the Cu piston velocity, $v_{\mathrm{Cu}}(t)$, which drives the compression wave through the sample and the LiF window. The simulations start with the observed apparent velocity of the Cu piston, $v_{\mathrm{Cu},0}(t) = v^{obs}_{\mathrm{Cu,apparent}}(t)$ as the initial guess for the velocity boundary condition. Once a simulation is complete the apparent velocity data from that simulation result is then computed using the refractive index models for both materials:

$$v^{sim}_{\mathrm{Cu,apparent}}(t) = \frac{d}{dt}\left[\int_{\mathrm{LiF\ window}} n(x,t)dx + \int_{\mathrm{D2\ sample}} n(x,t)dx\right] \qquad (3a)$$

and,

$$v^{sim}_{\mathrm{Al/LiF,apparent}}(t) = \frac{d}{dt}\left[\int_{\mathrm{LiF\ window}} n(x,t)dx\right]. \qquad (3b)$$

That is, the apparent velocity is the rate of change of optical path difference between the probe source and detector for the two paths: (i) reflection from the Cu piston through both the deuterium layer and the LiF window; and, (ii) reflection from the Al/LiF interface through the LiF window only. From the difference between the simulated and observed apparent velocities we generate a correction to the piston motion, $\delta v_{Cu,j}(t)$, and use the correction to update the boundary velocity: $v_{\mathrm{Cu,j+1}}(t) = v_{\mathrm{Cu,j}}(t) + \delta v_{Cu,j}(t)$. To generate the correction we use a characteristics analysis to connect the events observed at the Al/LiF interface to events at the piston surface occurring earlier in time (these events launch acoustic perturbations that are observed later at the Al/LiF interface). The

correction $\delta v_{Cu,j}(t)$ combines the observations from both optical paths in a weighted average to take into account information from both signals and is evaluated and applied iteratively through multiple simulation passes. We found that the simulation results converged to the data after about 10 – 20 iterations. The converged simulation model matched the data over the entire duration of the velocity signals to within experimental error (Fig. S16) after accounting for an additional correction to the refractive index model for dense deuterium.

When the Cu piston boundary velocity is converged, the corresponding simulation determines the complete space- and time-resolved history of the compressed sample layer. Of most interest is the temperature history, which is not possible to measure with our current techniques.

Thermal conduction effects

The Cu piston acts as a heat source adjacent to the sample layer. To estimate the temperature at the surface of the piston we computed the thermodynamic path experienced by the piston according to the various shock, release and reverberation events that interact with the piston. Initially the piston undergoes a shock and release event to initiate the first reverberation sequence. Following the first shock and release event the piston surface is heated to ~500 K and a series of weak shocks are transmitted back into the piston from the reverberating wave in the sample layer (causing it to decelerate); these events lead to quasi-isentropic heating; the temperature jumps are connected to the corresponding pressure jumps. The calculations show that the piston temperature is comparable to (but slightly lower than) the sample temperature during the first reverberation sequence. A second shock and release event initiates the second reverberation sequence culminating in the peak compression. Because the piston temperature is elevated when the second shock arrives the second shock and release event leads to a much higher piston surface temperature (3000 to 6000 K, see also Fig. S5). The subsequent reverberations follow approximately an isentropic path from there. The temperature estimates were computed using the SESAME 3336 equation of state table for Cu. The second reverberation sequence is much faster and passes through the IM transition pressure over a much shorter time interval (1 - 2 ns), too fast for the heat to penetrate the layer significantly. However, since the piston temperature can be as much as 3500 K higher than that of the sample it is important to develop a quantitative assessment of the conduction of heat through the layer. To make this assessment we assumed thermal conductivities that were close to the maximum credible values: 1, 50 and 1000 W/m/K for the LiF window, the deuterium sample and the Cu piston, respectively. Lower values are more likely and realistic, so this estimate provides an upper limit on possible heating effects. The heat equation using the temperature boundary condition was solved self-consistently with the equations of motion of the fluid. The effects of heat conduction can be evaluated by comparing with a similar set of simulations that assume no thermal conduction (Fig. S17). During the IM transition, the heat-affected zone is confined to approximately a tenth of the full thickness of the layer adjacent to the piston, which is situated at an optical depth of OD >> 3 from the window interface. At later times the heat-affected zone expands slowly but remains many optical depths away from the window interface. Thus, we conclude that the piston heating should not affect the optical signals.

Supplementary Text

Temperature path results

All three of the deuterium EOS models predict nearly the same pressure-density dependence, i.e. $P(\rho)$, independent of the temperature. This is because the thermal contribution to the pressure at the conditions of our experiments is relatively small. However, the estimated temperature history $T(t)$ varies significantly according to the EOS model used for the deuterium sample (Fig. S18), and this variability leads to a systematic uncertainty in estimating the temperatures of the sample (Fig. 3 and Fig. S19). The thermodynamic path is determined primarily by first-shock strength, along with small amounts of additional heating introduced by subsequent shocks. The simulations show sharp shifts in the *P-T* path at conditions close to predicted melting curves that arise from crossing of the melting line in the *P-T* trajectories predicted by the EOS models. The Kerley model represents an upper bound; other models give lower temperatures. The temperature spread among the available models leads to a large systematic uncertainty in estimated temperatures, as large as ±260 K near the IM transition.

Table S1 summarizes the two key optical signatures associated with the IM transition. For all cases listed, the pressures are tied to the calibration of the LiF window response, accurate to a few percent, while the temperatures are extracted from the *T-P* simulation results by combining the values predicted by the three EOS models. The first optical signature is the transition from partially-transparent to opaque, identified as the point where where the absorption coefficient reaches a threshold level of 1 μm^{-1} (absorption depth comparable to the vacuum wavelength of the probe beam). The corresponding optical depth of the deuterium layer reaches values of OD≈1.5 (double passed OD≈3) effectively extinguishing the reflection from the Cu piston. To determine the pressure corresponding to $\alpha = 1\ \mu m^{-1}$ we used least squares fits to the absorption data (Fig. S14) with exponential pressure dependence. The second signature is the transition to metallic behavior where the D/LiF interface reflectivity exceeds the threshold R > 30%. The choice of 30% reflectivity as a threshold is discussed below.

Refractive index of deuterium at densities above 1 g cm^{-3} (0.25 mol cm^{-3})

The need for correcting the deuterium refractive index model is illustrated in Fig. S20. Using the extrapolated Dewaele *et al.* fit (*35*) to the deuterium index the calculated apparent velocity of the Cu piston near the transition is consistently higher than observed by about 30% to 50%. The simulation model was brought into much closer agreement by incorporating a piecewise continuous correction to the Dewaele fit,

$$n(\rho_M) = \begin{cases} 0.994 + 3.26\,\rho_M, & \text{for } \rho_M < \rho_T \\ 0.994 + 3.26\,\rho_M + a(\rho_M/\rho_T - 1)^b, & \text{for } \rho_M \geq \rho_T \end{cases}, \qquad (4)$$

where ρ_M is the molar density and the three parameters ρ_T, a and b are a threshold density, a coefficient and an exponent for a power law form. (We use mol cm^{-3} units here to be consistent with Dewaele *et al.*) Over the range $\rho_M < \rho_T$ this form matches the Dewaele fit, while for $\rho_M \geq \rho_T$ the additional term provides the correction. The parameters ρ_T, a and b were determined by optimizing the fit to the apparent velocity of the Cu piston through the high-compression phase of the experiments using a Levenberg-Marquardt optimization. This optimization was repeated for 15 simulation runs, corresponding to all of the possible permutations among the 5 experiments and the three equation of state models for the deuterium layer. All of these optimizations produced a

consistent ensemble of fits for the density dependence of refractive index. We were able to obtain a wide-ranging match of the observed apparent velocities to the simulation model for all five of our data sets (see Fig. S20B for an example). We also investigated two other three-parameter forms for the corrected index: (i) a quadratic form $0.994 + 3.26\ \rho_M + a(\rho_M/\rho_T - 1) + b(\rho_M/\rho_T - 1)^2$; and (ii) a cubic form $0.994 + 3.26\ \rho_M + a(\rho_M/\rho_T - 1)^2 + b(\rho_M/\rho_T - 1)^3$. These two forms produced final estimates of the density dependence of the refractive index nearly identical to the form in equation (4).

The resulting adjustments to the index are summarized in Fig S21A and provide new information on the refractive index of fluid deuterium for 950 K < T < 1500 K and 0.25 mol/cm^3 < ρ_M < 0.5 mol/cm^3. Over the range of our fits the threshold density was near 1 g cm^{-3} (ρ_M = 0.25 mol cm^{-3}) and the correction magnitude reached > 0.7 relative to the linear extrapolation. The global best fit is given by: $\rho_T = 0.260 \pm 0.001$ [mol/cm^3], $a = 0.898 \pm 0.007$, $b = 1.29 \pm 0.01$, with correlation matrix: [[1,0.941,-0.932],[0.941,1,-0.770],[-0.932,-0.770,1]]. The fitting domain is for $0 < \rho_M \leq 0.5$ [mol/cm^3]. The broad spread in refractive index results over the ensemble of experiments encompasses a temperature dependence that becomes evident when the experiments are examined individually (we combined the first two experiments). Examination of the fits for the individual experiments reveals an index increasing with temperature for a given density, Fig. S21B.

Band gap estimates

The increase of the refractive index beyond the Dewaele fit signifies closure of the band gap. In general an increasing index is associated with a decreasing band gap, and studies of the relationship between refractive index and band gaps over a broad sampling of semiconductor materials have revealed empirical relationships that can be used to estimate the band gap from the index (*89*–*92*). Results from the empirical formulas proposed by Moss (*89*), Reddy-Anjaneyulu (*90*) and Hervé-Vandamme (*91*) are plotted in Fig. S22 based on the data in Fig. S21, all suggesting that the band gap has closed to about 1.8 – 2.0 eV at the point when the deuterium sample becomes optically thick. This is consistent with the onset of strong absorption expected to occur for the 1.9 eV photon energy (660 nm) used in our experiment. Linear extrapolations of the gap energies as a function of density (Fig. S22A), when plotted against pressure (Fig. S22B) all suggest that the gap closes between 200 and 250 GPa, depending on the temperature. These extrapolated gap closure pressures are consistently higher than the IM transition pressures (Table S1), indicating that gap closure is non-linear in density, possibly discontinuous.

The estimated gap energies are compared with the band gaps determined by Weir *et al*. (*10*) and McWilliams *et al.* (*20*). The Weir *et al.* experiments acquired band gap data over a reported temperature range of 1500 < *T* < 3000 K (calculated, lower temperatures correlated with lower pressures); the data shown are from the reanalysis by Knudson *et al.* (*22*) who found a somewhat higher range of temperatures, 2000 K < *T* < 4000 K. The McWilliams *et al.* datum is at 2400 K (measured). Our index measurements encompass a range of conditions broadly in the range of 1000 K to 1550 K, reaching a factor of two or three lower in temperature than the other measurements, and show consistency with the temperature-dependent trends in the Weir *et al.* and McWilliams *et al.* results.

Lorentz oscillator model

An approximate fit to the optical response of the sample below the metallization transition is possible with the single oscillator Lorentz model, incorporating the density dependence of the band gap. The Lorentz oscillator model reads as,

$$\varepsilon(\omega) - 1 = \frac{4\pi N f e^2}{m_e} \frac{1}{\omega_0^2 - \omega^2 - i\gamma\omega}, \quad (5)$$

where $\varepsilon(\omega)$ is the dielectric function, ω_0 is the oscillator frequency, γ is a damping rate, N is the number density of electrons and f is an oscillator strength. Based on discussions found in Moss (*89*), Hervé and Vandamme (*91*) and Ravindra *et al.* (*92*) the oscillator frequency and band gap are closely connected and can be related through an energy offset,

$$\hbar\omega_0 = E_{\text{gap}} + B, \quad (6)$$

where $B \approx 3.4$ eV has been found empirically to fit a wide range of cases (*91*). We assume that

$$N = (2\,A\,\rho)/M, \quad (7)$$

where ρ is the mass density, A is Avogadro's number, M = 4.028 g mol^{-1} is the molecular weight of the deuterium molecule, and the oscillator strength is $f = 0.34$ (adjusted to match, approximately, the real part of the index of refraction near the transition). The parameter ω_0 varies as a function of density according to equation (6) using the linear fits shown in Fig. S22B and γ is adjusted to match the optical conductivity. The optical conductivity can be extracted directly from the data with the expression,

$$\sigma(\omega) = \alpha\,\mathrm{Re}(n)c. \quad (8)$$

Comparison of the model with the data for one experiment is shown in Fig. S23. It is evident that the Lorentz model does not individually match the real and imaginary parts of the index very accurately, but the errors cancel out in a way that matches the optical conductivity, thus establishing a well-defined value of γ for each experiment. The values of γ range from $\gamma = 3.5 \times 10^{14}$ Hz (N150701-002, N171105-003) to $\gamma = 1.1 \times 10^{15}$ Hz (N150915-002). This represents a damping rate in the range of 4% to 14% of the resonant frequency; the absorption at 660 nm is in the tail of the oscillator resonance and is produced by extended interband states below the band edge that are created by the increasing level of disorder associated with higher temperatures.

Smith-Drude conductivity model

The Smith-Drude conductivity model (*37*) is more suited than the Lorentz model for quantifying the metal-insulator transition at and beyond band gap closure; it has been used successfully to model spectrally-resolved absorption data near the IM transition by McWilliams *et al.* (*20*) In this model, the complex-valued optical conductivity is given by,

$$\sigma_{SD}(\omega) = (Ne^2\tau/m_e)(1 - i\omega\tau)^{-1}[1 + C(1 - i\omega\tau)^{-1}], \quad (9)$$

where N is defined by equation (7), τ is a relaxation time and C is an additional parameter referred to as the backscatter parameter. The parameter C is defined in the interval [-1,0], with the case C=0 corresponding to the traditional Drude model. At the other extreme C=-1 the Smith-Drude expression represents a conductivity model in which scattering events are dominated by backscattering (similar to the conductivity of extended states within the band gap). A plot of the real part of the optical conductivity as a function of C is shown in Fig. S24 for the case of $\tau = 0.075$ fs and $\rho = 2.0$ g/cm^3. These parameters

were chosen to match approximately the behavior of liquid deuterium near the IM transition. Note that the relaxation time defines the frequency of the broad resonance near $\hbar\omega = \hbar\tau^{-1} \approx 9$ eV. The relaxation time is closely connected to the Ioffe-Regel minimum scattering time (*93*, *94*, *36*), i.e. assuming nearest neighbor scattering for electrons at the Fermi velocity. This produces values ranging between 0.05 fs and 0.1 fs depending on the density and the degree of ionization. On the insulating side of the transition the backscatter parameter starts near *C*=-1 and the DC conductivity is zero; on the conducting side C approaches zero (Drude-like). At intermediate values of *C,* the DC conductivity is finite and the frequency-response has a non-Drude character that is typical of metal-insulator transitions. The utility of the Smith-Drude model lies in providing a simple three-parameter functional form that captures the main features of modern calculations of optical conductivities near insulator-metal transitions in shock compressed materials. For example, compare Fig. S24 with Fig. S7 of the supplementary material from Knudson *et al.* (*22*); also compare with calculations of optical conductivity along the deuterium principal Hugoniot by Collins *et al.* (*95*, *96*) (specifically Fig. 3 in (*95*) and Fig. 1 in (*96*)), finally with Fig. 3 in Morales *et al*. (*14*) The Smith-Drude model is therefore appropriate for representing the optical conductivity throughout the IM transition by varying the backscatter parameter from *C*=-1 (insulator) to *C*=0 (metal).

We use the parameter *C* in the Smith-Drude model to characterize the extent of the IM transition by matching to the observed reflectivity data. To do this we start with the complex-valued refractive index,

$$n_{SD}(\omega) = \sqrt{\epsilon_{SD}(\omega)} = \sqrt{1 + 4\pi i\sigma_{SD}(\omega)/\omega}\,, \tag{9}$$

combine it with the calibrated model for the refractive index of LiF, compute the pressurized D/LiF interface reflectivity using the Fresnel formula, and solve for values of *C* that match the reflectivity data. The density $N(\rho)$ is varied according to the experimental ρ extracted from the simulations (eq. 7), and τ is kept constant. The real part of the index of refraction predicted by the Smith-Drude model just below the IM transition is primarily sensitive to τ and relatively insensitive to *C*; the imaginary part is sensitive to both. Thus, it is important to choose τ to match the measured refractive index data near the transition (i.e. $n \approx 3$). τ also controls the saturation level of the reflectivity ($R \approx 55\%$) at pressures above the IM transition pressure. Based on these considerations we set $\tau = 0.075$ fs; this value is consistent with the study of McWilliams *et al*. (*20*), with our measured index data and with the saturated reflectivity.

Near the minimum reflectivity, ~10%, the model matches the data with *C*=-1, consistent with the behavior of an insulator or semiconductor. The fits, shown in Fig. S25, show that *C* > -1 at P > 170 GPa, at which point *C* increases with pressure approximately linearly and the DC conductivity rapidly exceeds 10^3 S/cm within a few GPa of the onset of the reflectivity rise. The conductivity reaches a value of 2000 S/cm to 3000 S/cm when -0.8 < *C* < -0.7, representing the behavior of a poor metal.

Estimates of the minimum metallic conductivity for hydrogen near the Mott transition range from 500 S/cm to 4000 S/cm, depending on the density (*36*, *97*). A minimum conductivity criterion is needed to identify the threshold for metallic behavior. Since the estimated conductivity is model-dependent, we establish a reflectivity threshold as an alternative criterion and determine the metallization pressure directly from the reflectivity data. The threshold we use is *R* > 30%. Within the context of the Smith-Drude model the relationship between reflectivity and σ_{DC} is shown in Fig. S26. Here we

find that $R > 30\%$ corresponds to $\sigma_{DC} > 2000$ S/cm, within the middle of the range estimated by Nellis *et al.* (*36*) The curves in Fig. S26 show sensitivity to the choice of τ for $R < 30\%$. This is because the real part of the index dominates in the Fresnel formula when $\sigma_{DC} \approx 0$ and $C = -1$. The value $\tau = 0.08$ fs likely overestimates the refractive index, hence overestimates the reflectivity, while $\tau = 0.07$ fs may underestimate it. For $R > 30\%$ both cases converge to a common curve for σ_{DC} as a function of R. A similar set of curves establishing the relationship between σ_{DC} and R was computed by Knudson *et al.* for 532 nm light (*22*) using a detailed and rigorous model (shown in Fig. S7 of the supplementary material of that work); from that study $R > 30\%$ also corresponds to $\sigma_{DC} > 2000$ S/cm, confirming our choice of threshold.

Returning to Fig. S25, the experiments show slightly different thresholds, all near 200 GPa, with threshold pressure increasing at lower temperature (lower isentrope). The four experiments in the temperature range 1080 K < T < 1640 K showed significant reflectivity exceeding 3000 S/cm in the range 194 GPa < P_{metal} < 221 GPa. The first experiment, N150701-2 at 940 K, did not produce higher than 10% reflectivity, suggesting in that case $P_{metal} > 215$ GPa. It is interesting to note that the threshold pressures defined by $\sigma_{DC} > 2000$ S/cm or $R > 30\%$ are systematically lower, by 10 – 40 GPa, than the gap closing pressures inferred from the linear extrapolation of the gap energy with density (Fig. S21B). In the high-pressure limit DC conductivity saturates above 10^4 S/cm for P > 300 GPa, consistent with previous calculations and measurements. Most of the curves do not show strong evidence for a prominent conductivity jump that could signify a first-order phase transition although as discussed above our instrumentation may not be able to resolve such a jump. N171105-3, recorded at higher time resolution, did show a sharp jump. The data do show that the DC conductivity increases by more than an order of magnitude from non-metallic to metallic levels within a span of about 20 GPa in pressure.

Comparison to Z experiment

The reverberation experiments performed at the Z facility by Knudson *et al.* (*22*) used a technique and geometry similar to those of the present study, but produced apparently conflicting results. Comparison of the optical reflectance as a function of pressure for a NIF experiment and a Z experiment (Fig. S27) reveals key similarities and differences in the measurements. The Z reflectances are systematically lower for P > 120 GPa and stay near zero in the range 140 < P < 240 GPa, much lower than the expected ~10% minimum dielectric interface reflectivity. These differences can be partly attributed to wavelength-dependence (532 nm versus 660 nm probe wavelengths), but not entirely. The Z reflectance signals exhibit complicated temporal behavior.

These contrasting features need to be understood both to understand the IM transition, and to provide a foundation for future applications of both experimental platforms. The Z experiments differ from those at NIF in several key details. The relevant differences are (i) the use of an Al piston instead of a Cu piston; (ii) a sample layer initially 150 μm thick, approximately 5 x thicker than on the NIF experiments; (iii) compression path defined by a single shock in the piston and sample followed by a single reverberation sequence and smooth ramp compression; (iv) a ramp-compression time scale approximately 200 to 300 ns in duration, two orders of magnitude longer than for the NIF experiments (crucially this is also several times the acoustic transit time across

the lateral extent of the sample, $\tau \approx 60$ - 100 ns, derived below); and, (v) a complicated time history of reflectance, velocity signal dropouts and non-reversible response on decompression. The strong jumps in the observed reflectance near 300 GPa were interpreted to be signatures of the IM transition.

Sample confinement

In both the NIF and Z experiments the sample layer is confined in two dimensions by the piston and window, but there is no confinement in the third lateral dimension. Since the sample can escape at the edges where $P \approx 0$, a pressure release wave (rarefaction wave) propagates from the edge to the center when the compression starts. Fluid entrained in the wave accelerates towards the edge. The propagation speed of the head of the release wave is the speed of sound, C_s. The speed of sound in the deuterium is higher than in the confining walls (Fig. S5). The confinement time is $\tau_c = R/C_s$, where R is the distance from the sample edge to the center. A diagram of characteristics (trajectories of acoustic signals across the lateral dimension of the sample) in Fig. S28A shows the domain of influence of the edge rarefaction. Edge rarefactions in the NIF experiments are launched at $R \pm 500$ μm, and do not reach the center of the field of view until $t \approx 50$ ns, well after completion of the experiment. Therefore, the NIF samples remain *inertially confined* in the lateral dimension during the experimental observations, and the assumption of one-dimensional axial motion for analysis is valid.

The pattern of characteristics shown in Fig. S28B, for one of the Z experiments, shows that edge rarefactions (launched at $R = \pm 2.8$ mm) reach the field of view of the diagnostic fiber probes ($R = \pm$ 1 mm) at $t \approx 170$ ns (approximately the time when the VISAR signal viewing the Cu piston becomes noisy), and they meet in the center at $t \approx$ 240 ns. The samples in the Z experiment may therefore be subject to lateral pressure gradients and rarefaction flows.

Lateral flow (Z experiment)

The primary observables in the Z experiment are the signals from a pair of fiber-coupled point-VISAR probes arranged to view the motion of the compressed layer and the LiF window interface, in a similar fashion to the NIF experiment. The raw data from these signals were kindly provided by M.D. Knudson (*97*). The pair of probes were separated by a lateral distance of $L \approx 2$ mm. During the ramping part of the experiment the two VISAR probes recorded apparent velocities that matched very closely, but not exactly. (The difference is evident with close examination of Fig. 2 in Knudson *et al.*) Loss of velocity information from the probe viewing the sample layer occurred during time intervals totaling about 150 ns duration for each experiment. When both signals are available they can be subtracted to assess the magnitude of velocity difference, and therefore pressure difference between the two probes. Fig. S29A shows the velocity differences for the four Z experiments.

The VISAR probes measure the apparent velocity of either the piston surface or the D/LiF window interface. During the ramp phase the two interfaces remain in near pressure equilibrium, because the sound speed in the deuterium layer varies between 10 and 16 km/s during the compression, while the layer thickness ranges between 15 and 30 microns. (Sound speeds in the confining walls are lower, see Fig. S5.) Therefore, pressure equilibration across the layer (axial direction) occurs in the range of 1 – 3 ns,

much shorter than the 300 ns experiment duration. The apparent velocity at the probe location combined with the known response of the LiF window was used to infer the pressure at the D/LiF window interface, and can be assumed to represent the local pressure in the layer (averaged in the axial direction across the layer). In the lateral dimension the two probes measure slightly different velocities, evidence of a pressure gradient along the lateral dimension. Fig. 26B shows the lateral pressure differences.

The lateral pressure gradient (of order a few percent of the peak pressure) drives flow of the sample fluid in the direction parallel to the layer. As discussed above, for short times the fluid layer remains inertially confined, but for times longer than a sound transit time ($\tau_L = L/C_s \approx 100$ ns) the fluid accelerates in response to the pressure gradient. The signals in Fig. S29A and S29B show time variations occuring on a characteristic time scale comparable to this estimate. We apply Newton's second law to compute the average acceleration of the fluid layer driven by the time-varying pressure difference, and integrate to determine the average flow velocity (assuming a nearly inviscid fluid). The accelerating flow velocity is given by,

$$u(t) = \int \frac{\Delta P(t)}{\rho(t) L} dt, \tag{10}$$

where $\Delta P(t)$ is the time-varying pressure difference between the two probes, L = 2 mm is the spacing between the two VISAR probes, and $\rho(t)$ is the time-varying spatially-averaged density of the layer (estimated from $P(t)$ and the compression isentrope of the D_2 fluid). The signal dropouts from the D/LiF probe force us to supply the missing information with plausible values. In Fig 2B we set the pressure difference to a constant at the maximum recorded before the dropout over the duration of the missing interval. The trends in the signals suggest that this may underestimate the pressure difference over some portion of the dropout interval (because we don't expect the signals to respond on a time scale much short than τ_L). Integration of equation (10) using the signals plotted in Fig. S29B leads to Fig. S29C showing the lateral flow velocity produced by the pressure gradient. The estimated velocity reaches between 0.4 and 0.7 km/s. This magnitude remains significantly smaller than the axial velocity (~10 km/s), but is nevertheless large enough to lead to convection within the sample.

The Peclet number of this flow, defined as (*98, 99*),

$$Pe = \frac{X(t)u(t)}{\chi} = \rho C_P X(t) \frac{u(t)}{\kappa}$$

involves the scale length (layer thickness) *X(t)*, the flow velocity *u(t)* and the thermal diffusivity $\chi = \kappa/\rho C_P$, which depends on the thermal conductivity κ and the specific heat capacity at constant pressure, C_P. The Peclet number provides a measure of the relative importance of advective or convective transport to diffusive transport within hydrodynamic flows . We find 200000 > *Pe* > 5000 as the thermal conductivity varies between 1 < κ < 25 W/m/K (insulating to conducting). In systems with large *Pe* heat transfer is dominated by advective (or convective) processes rather than diffusive processes.

The Reynolds number is,

$$Re = \rho(t) u(t) X(t)/\mu, \tag{11}$$

where $\rho(t)$ is the average mass density in the layer, $u(t)$ is the lateral flow speed, μ is the viscosity and $X(t)$ is the thickness of the layer. The viscosity of liquid metallic hydrogen, μ, at the conditions of the experiment has been estimated by Clérouin (*100*)

and Li *et al.* (*101*) to be $\mu \sim 0.5$ mPa-s. Using this value along with the time-dependent $X(t)$ and $u(t)$ leads to Fig. S29D. The Reynolds numbers associated with the lateral flow reach values of 20000 or higher. Fluid flow in constrained channels becomes turbulent typically when Re > 1000, thus the fluid D_2 layer develops turbulent flow patterns within a few tens of nanoseconds after the lateral acceleration begins.

Heat exchange with the confining walls (Z experiment)

Both the Al piston and LiF window temperatures are substantially lower than the D_2 sample. Convective heat exchange between the fluid sample and the confining walls can be estimated using engineering formulas based on Newton's law of cooling (*102*),

$$Q = \rho A X C_v \frac{d\,\Delta T}{dt} = hA\,\Delta T. \qquad (12)$$

Here Q is cooling power, $\Delta T = T_F - T_W$ is the temperature difference between the fluid and the wall, X is the thickness of the fluid layer, ρ the density, C_v the heat capacity, A the surface area and h is the convection coefficient (units of e.g. W/m^2/K). The convection coefficient can be estimated from empirical Nusselt number correlations. The Nusselt number, *Nu*, gives the ratio of convective transport relative to thermal conduction expressed in the form $Nu = h\,X/\kappa$, where κ is the thermal conductivity and X is the relevant scale length, in this case the thickness of the layer. Nusselt number correlations are determined from empirical measurements and are typically expressed in the form,

$$Nu = CRe^n Pr^\alpha$$

which involves the Reynolds number, the Prandtl number, *Pr*, a coefficient *C* and two power law exponents. The earliest practical formulation was published 1933 by Dittus and Boelter (*103*). More recent investigations have provided refinements; a recent study of Jo *et al.* (*104*) is relevant because of similar geometry. The Jo *et al.* fit reads,

$$Nu = 0.0058\,Re^{0.94} Pr^{0.4}$$

The Prandtl number, a property of the fluid, is defined as $Pr = C_P\mu/\kappa$, which evaluates to Pr = 0.2 for the compressed D_2 (assuming μ = 0.5 mPa-s, κ = 25 W/m/K and $C_P \approx C_v$ = 10 J/g/K). Evaluation of this expression for $20000 < Re < 40000$ yields $30 < Nu < 60$. Evaluation using the Dittus & Boelter correlation produces almost the same result. Therefore, convective mechanisms dominate heat transport because the convection coefficient is about two orders of magnitude higher than would be expected from standard thermal conduction. Evaluation of equation (12) using $Nu \sim 60$ and a temperature difference of ΔT = 500 K, leads to an estimated cooling rate 25 K per 100 ns.

We estimated the Al piston temperature using two EOS models for Al and knowledge of the compression path experienced by the piston. Compression of the deuterium sample starts with an initial shock transmitted through the aluminum piston and then into the deuterium sample. Several reverberations occur as the shock passes through the sample and reflects repeatedly from the LiF window and the Al piston surface. The piston temperature is therefore determined by the initial shock state and the isentrope connecting that state to higher pressures, because the reverse-directed reverberation shocks are weak (quasi-isentropic), as is the subsequent ramp compression. The estimates, using two available equation of state models for Al, are shown in Fig. S30. We take as the final temperature for the Al piston surface the temperature reached at the IM transition pressures published by Knudson *et al.*, all within the range of $280 < P_{IM} <$ 305 GPa. These results are summarized in Table S2. These temperatures range from 500

< T < 1000 K, approximately a factor of two, or 800 K, lower than the estimated deuterium sample bulk temperatures (assuming no thermal transport). The two models produce somewhat different results; a systematic uncertainty of about ± 140 K is estimated from the difference between models. The incident shock stress in the piston ranges between 25 and 40 GPa. These estimates assume hydrostatic compression of the aluminum piston, which neglects the effects of dynamic yielding under which the compression process is partly elastic and partly plastic. Only the plastic deformation contributes to heating. The strength of Al under shocks, around ~2 GPa, is a significant fraction of the first shock stress. Because the simplified analytic calculations summarized in Fig. S26 and Table S2 do not account for the yield strength (elastic-plastic response of Al), they overestimate the true temperature of the piston surface (possibly by 10% to 20%).

Similar calculations can be used to estimate the temperature of the LiF window and the resulting values are somewhat lower than the corresponding Al temperature. However, precise values are not needed because the low thermal diffusivity of LiF results in a negligible effect on cooling rates.

Convective exchange of heat with the confining walls cools the D_2 fluid. Fig. S31 shows the results of thermal conduction calculations similar to the calculations of Knudson *et al.* that examined the D_2-LiF interface. Our calculations assume static conditions (no fluid flow and no wall motion) similar to those obtained on the Z2631 experiment near 200 GPa: ρ_{D2} = 1.79 g/cm^3, T =1600 K, ρ_{Al}=5.22 g/cm^3, T_{Al}=670, ρ_{LiF}=5.14 g/cm^3, T_{LiF}=552 K. For thermal conductivities we used 700 W/m/K, 25 W/m/K and 1 W/m/K for the Al piston (*105*), D_2 layer (*106*) and LiF window (*22*), respectively. The intrinsic thermal conductivity of the D_2 layer is too low to allow the bulk of the sample layer to be significantly cooled under static conditions (Fig. S31A); a boundary layer of ~3 μm thickness will be cooled near the Al piston and LiF window surfaces while the bulk of the layer remains at constant temperature. The turbulent flow conditions increase the thermal transport coefficient by around two orders of magnitude. We repeated the calculation (Fig. 31B) with κ_{D2} artificially increased from 25 W/m/K to 2500 W/m/K. The average layer temperature drops by about 100 K on a time scale of 200 ns, while the temperature at the piston surface increases to 1400 K. The specific heat capacity of the Al at these conditions ~1 J/g/K is an order of magnitude lower than that of the D_2 fluid ~10 J/g/K. This is too low to absorb much heat from the D_2 fluid without raising the wall temperature to values close to the fluid temperature. As the wall heats up the cooling effect diminishes and most of the heat remains in the D_2 fluid.

The confining walls, therefore, do not have enough heat capacity or thermal diffusivity to cool the D_2 sample by much more than about 100 K, even under convective flow. The transfer of heat into the Al piston wall, however, leads to the lack of reversibility in the IM transition pressure upon decompression, discussed below.

Latent heat and turbulent mixing (Z experiment)

Recent theoretical models predict that the liquid-liquid IM transition in hydrogen is a discontinuous first-order transition below 1400 K with a volume change of approximately 2% - 3% (*13–16*). From direct evaluations of the simulation results (*15*), and based on the Clausius-Clapeyeron equation the latent heat across the transition is approximately (for deuterium) ΔH ~ 2.5 to 3 kJ/g (*14*, *15*). The experiment follows an

isentropic compression path and across a first-order transition the compression isentrope resides in the mixed phase region over an extended range of T and P. That is, the compression path follows the IM phase line to *lower* temperatures as the sample layer is compressed through the transition. The temperature drop between the beginning and the completion of transformation along a particular isentrope can be estimated from the Clausius-Clapeyron relation.

Compression-induced self-cooling due to mixing and advection occurs during the IM transformation. A heterogeneous distribution of temperatures in the layer develops as metallized and insulating fluid elements are mixed between the walls and the central region of the layer. The hottest fluid elements respond to the increasing ramp pressure by undergoing the IM transformation first (because the highest isentropes intersect the phase line at the lowest pressure, $dT/dP < 0$). Metallized and un-metallized elements are in close thermal contact owing to turbulent mixing. Increasing compression causes a temperature drop of the transforming mixed-phase because mixed phase states are constrained to follow the phase line. As a consequence, the average temperature of the sample layer decreases under adiabatic compression, including the fluid fraction that has not yet transformed. Because the metallization pressure increases with lowering temperature, a steadily increasing pressure is required to force the transformation of the unmetallized fluid fraction. At high enough pressure the entire layer is completely transformed (Fig. S32), and the average temperature is lower than the temperature when the transformation initiated.

The point-VISAR reflectivity signal is collected from a sampling area of approximately 200 μm diameter, much larger than the expected size of the turbulent eddies in the layer (5 – 10 μm). It records a signal in proportion to the fraction of metallized fluid in contact with the LiF window. When the transformation initiates most of the fluid elements advected into the LiF window boundary are insulating and highly absorbing, and a negligible reflectance signal is registered. As the transformation progresses, the VISAR registers a moderately increasing and fluctuating reflectivity signal because turbulent eddies containing both metallized and insulating (absorbing) fluid elements are periodically advected into the boundary layer at the D/LiF window interface. (The reflectivity probe is sensitive to a skin depth layer of approximately 100 nm thick near the D/LiF window interface). Steady high-reflectivity signals are unlikely to occur until the *entire* sample layer has transformed. This scenario is consistent with the fluctuating low-to-moderate reflectivity signals observed in the Z experiments prior to the high reflectivity phase. We therefore infer that the high reflectivity regime observed towards the end of the Z experimental records should be identified with *completion of IM transformation across the entire layer*; i.e. the point where the *compression isentrope exits the mixed phase region*. The temperature at this point is several hundred Kelvin lower than at the starting point. We provide quantitative temperature estimates below.

Lack of reversible signal on decompression (Z experiment)

The Z experiments documented an extended period of high reflectivity signal bounded by two strong reflectivity jumps. The initial jump, a transition from low to high reflectivity $dR/dt > 0$ occurs at pressure P_1 during increasing pressure $dP/dt > 0$. Upon release of the peak pressure $dP/dt < 0$ a second jump from high to low reflectivity $dR/dt < 0$ is observed at pressure P_2. In all cases the pressures associated with these two events

were such that $P_2 < P_1$. A systematic relationship between $\Delta P_{IM} = P_1 - P_2$ and the temperature is also evident (larger ΔP_{IM} on lower isentropes, see Fig. 4 in Knudson *et al.*). Knudson *et al.* proposed that this lack of reversibility is explained by thermal conduction in the boundary layer near the LiF window. The explanation invoked a rapid change in the thermal conductivity of the deuterium upon metallization, and the calculations assumed laminar conditions. However, the assumption of laminar conditions is not consistent with high *Pe* and *Re* flow.

We propose that both of the jumps are associated with the IM transition and the lack of reversibility is connected with exchange of heat with the Al piston wall. The temperature of the wall is raised rapidly to within 100 – 200 K of the temperature of the deuterium fluid (Fig. S31B) before the metallization transformation begins. The wall stores this heat in a layer about 10 μm thick. As the metallization progresses the temperature of the metallized deuterium subsequently drops, eventually to reach values that are *less* than the wall temperature (because of latent heat). The reversal in temperature gradient causes heat to flow back into the metallized deuterium from the wall during the peak pressure phase of the experiment. The flow of heat into the metallized fluid raises the thermodynamic path to a higher isentrope (Fig. S32). The decompression path along the higher isentrope intersects the IM phase line at higher temperature $T_2 > T_1$, and lower pressure $P_2 < P_1$, because $dP/dT < 0$ along the phase line. Our interpretation is qualitatively consistent with all of the features observed in the Z experiments including the systematics of the ΔP_{IM} trend (because the slope of the PPT phase line is expected to flatten out at lower pressure).

Revised temperature estimates (Z experiment)

We combine transition pressure observations from the NIF data and the Z data to estimate the temperature drop in the Z experiments. The NIF experiments follow a series of isentropes overlapping those of the Z experiments fairly closely. The four highest-temperature NIF experiments indicate $194 < P_{IM} < 222$ GPa, whereas the Z experiments document $283 < P_{IM} < 305$ GPa over a similar range of isentropes. Assuming the two sets of transition-pressure observations mark the beginning (NIF) and completion (Z) of the IM transformation respectively, then the compression path resides within the mixed-phase region for approximately 100 GPa before the transformation is completed. The Clausius-Clapeyron equation cast into finite difference form reads,

$$T_0 \frac{\Delta P}{\Delta T} = \frac{\Delta H}{\Delta V},$$

which can be rearranged to give the estimated ΔT,

$$\Delta T = T_0 \frac{\Delta P\, \Delta V}{\Delta H} = f T_0.$$

Following an isentrope that intersects the IM phase line on the insulating side at T_0, the fluid temperature upon completion of the metallization transition will be $T_1 = T_0 + \Delta T$ at pressure $P_1 = P_0 + \Delta P$. Assuming that ΔH, ΔV and ΔP are constant (or nearly so) we find that the temperature drop ΔT is proportional to T_0, given by the scaling factor f. Note that $\Delta T < 0$ and $f < 0$ because $\Delta V < 0$, $\Delta P > 0$ and $\Delta H > 0$. Using the estimated latent heat $2.5 < \Delta H < 3$ kJ/g, 2% - 3% relative volume change $0.011 < |\Delta V| < 0.016$ cm^3/g (near 200 GPa) and the observed pressure difference $90 < \Delta P_{IM} < 100$ GPa we find the correction factor lies in the range $-0.65 < f < -0.33$, or $f = -0.49 \pm 0.16$. The revised

temperatures are given by $T_1 = (T_0 - \Delta T_{CW})(1 + f)$, where we have added an additional temperature term $\Delta T_{CW} \approx 100$ K to account for cooling by the piston wall prior to the start of the IM transformation. Using this expression we arrive at the set of corrected temperature values for the Z experimental data in Table S3. The downward corrections are in the range –600 K > ΔT > –900 K. These corrections place the Z data near the low temperature limits of the calculations by Pierleoni *et al.* (*15*) and close to the melt transition measured by Zha *et al.* (*23*).

To summarize: (i) the Z-experiment reflectivity jumps take place when the IM transition is nearly complete (low fraction of insulating and absorbing fluid), rather than beginning (low fraction of metallized fluid); (ii) the conclusion that the abrupt nature of the optical signals signifies a first order transition remains unchanged; (iii) temperature estimates for the Z reflectivity need to be reduced by about 600 – 900 Kelvin from the published values owing to the latent heat of the IM transition; and, (iv) the pressures of the Z reflectivity jumps are consistent with the Morales *et al.* (*14*) and Pierleoni *et al.* (*15*) calculations, assuming a latent heat at least as high as reported in those studies. The correct EOS model should be able to match both the NIF and the Z observations, since the two experiments sample the phase line at opposite ends of the IM transformation along a given isentrope.

Lateral flow (NIF experiment)

Time scales in the NIF experiment are short enough to enforce inertial confinement, however, lateral pressure gradients do exist as a result of a gently parabolic spatial distribution of ablation pressure across the piston surface (evident in the streak data). From the characteristics diagram in (Fig. S28A) fluid elements separated spatially by more than 200 μm do not communicate with each other during relevant experimental times. We use equation (10) to estimate an upper bound on gradient-driven flow, although this equation is marginally valid in the inertially-confined context. Velocity measurement uncertainties (larger than the Z velocity uncertainty) make the estimate challenging. Using the velocity maps extracted from N150914-2 and for points spatially separated by up to L = 200 μm we find |u| < 100 m/s (with fluctuating direction) and Re < 1000. As a consequence, the assumption of inertially-confined laminar flow is justified and the use of standard thermal conduction analysis is expected to be accurate. The boundary layer near the LiF window should remain intact throughout the measurement time.

Interpretation of optical signals on NIF platform

The optical reflectivity signals in the NIF experiments emerge from a layer approximatley 100 nm thick adjacent to the LiF window. This thickness is the approximate skin depth of the metallic phase, or the absorption depth of the semiconducting phase just before metallization. This layer is in pressure equilibrium with the LiF window, and while it is in thermal contact with the adjacent material in the sample thermal conduction is too slow to affect its energy content on the time scale of the compression. The NIF data sets do provide spatially-resolved signals (~5 μm spatial resolution), and the layer is observed to transform homogenously. There is no evidence of spatially heterogenous reflectivity or velocity signals in our data sets.

In the NIF experiments, a temperature gradient is established in the sample layer from the start, with increasing temperature going from the LiF window to the Cu piston. This comes about because the initial shock launched across the layer is slightly decaying, causing an entropy gradient to be established across the layer with higher entropy near the piston (Fig. S5); furthermore, the heated Cu piston transfers additional heat into the layer over a thickness of ~100 nm adjacent to the piston surface. As a consequence, the metallization transition begins at the Cu piston surface (because higher isentropes metallize at lower pressures) and propagates as a transformation front moving across the layer from the Cu piston towards the LiF window.

The energy driving the transformation process comes from the mechanical *PdV* work provided by the compression process. Because the metallized region is cooler than the insulating region, the temperature gradient is locally reversed at the transformation front; conductive heat transfer into the metallized region is therefore possible. However, the rate of pressurization *dP/dt* is too fast to allow thermal conduction to have much effect on the transformation rate. The optical signal of the transformation (reflectivity increase) occurs when the transformation front reaches the LiF window, and is observed at the thermodynamic state corresponding to the intersection of the isentrope in the insulating phase with IM phase line (point P_0, T_0 in Fig. S32). The current EOS models do not account for the first-order IM transition, and predict isentropic compression paths following $0.8 < dT/dP < 1.6$ K/GPa paths across the transition (larger at higher *T*). The plotted *T* therefore corresponds to *T* at the start of the transformation. A higher *P* the temperature should drop as a consequence of the latent heat of the transformation; in other words, if an appropriate temperature diagnostic were available we expect to see a rapid temperature drop simultaneous with the increase in reflectivity.

Extended phase diagram

In Fig. S33 we place current experimental data sets on an extended phase diagram along with shock compression data. These data include observations of optical reflectivity and shock temperature along the principal Hugoniot of D_2, and similar observations for shock compression of precompressed samples of H_2. The metallization transition at these conditions has been observed to be continuous, with no evidence of first-order behavior (*61*, *62*) . The revised temperature estimates of the Z data are included. Fig. S34 compares the dynamic compression results for the IM transition in D_2 with currently published models, and with the revised temperatures for the Z experiments.

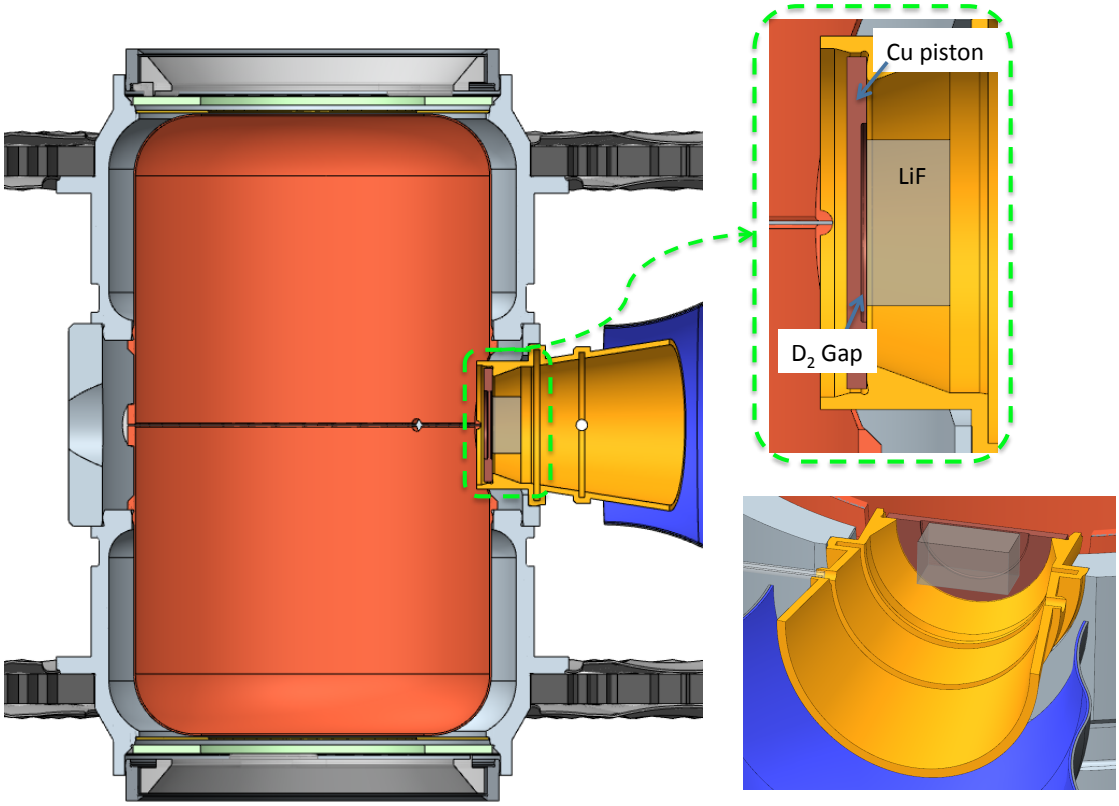

Fig. S1.
Sketch of the target assembly showing details of the sample package.

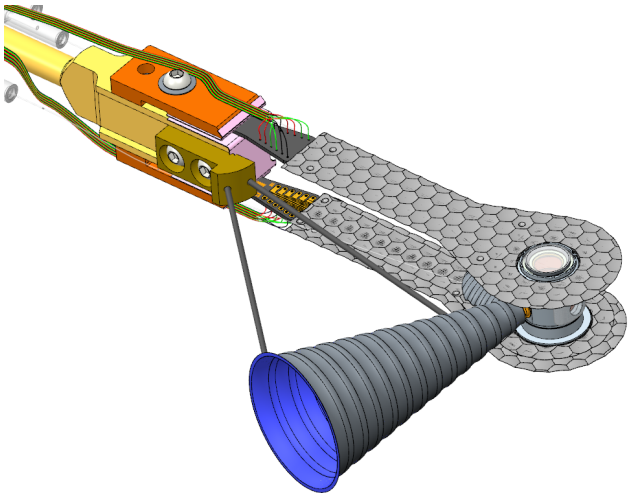

Fig. S2
Target assembly attached to cryogenic support as installed in the target chamber.

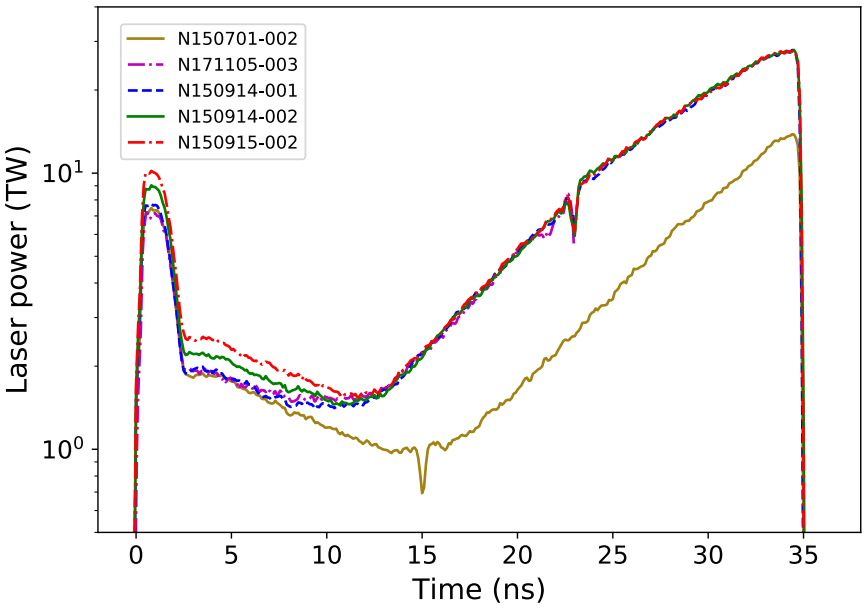

Fig. S3

Laser power history delivered to the hohlraum interior for each of the four experiments carried out in the present study. The temperature-pressure path depends on the initial shock, set by the amplitude of the initial power spike.

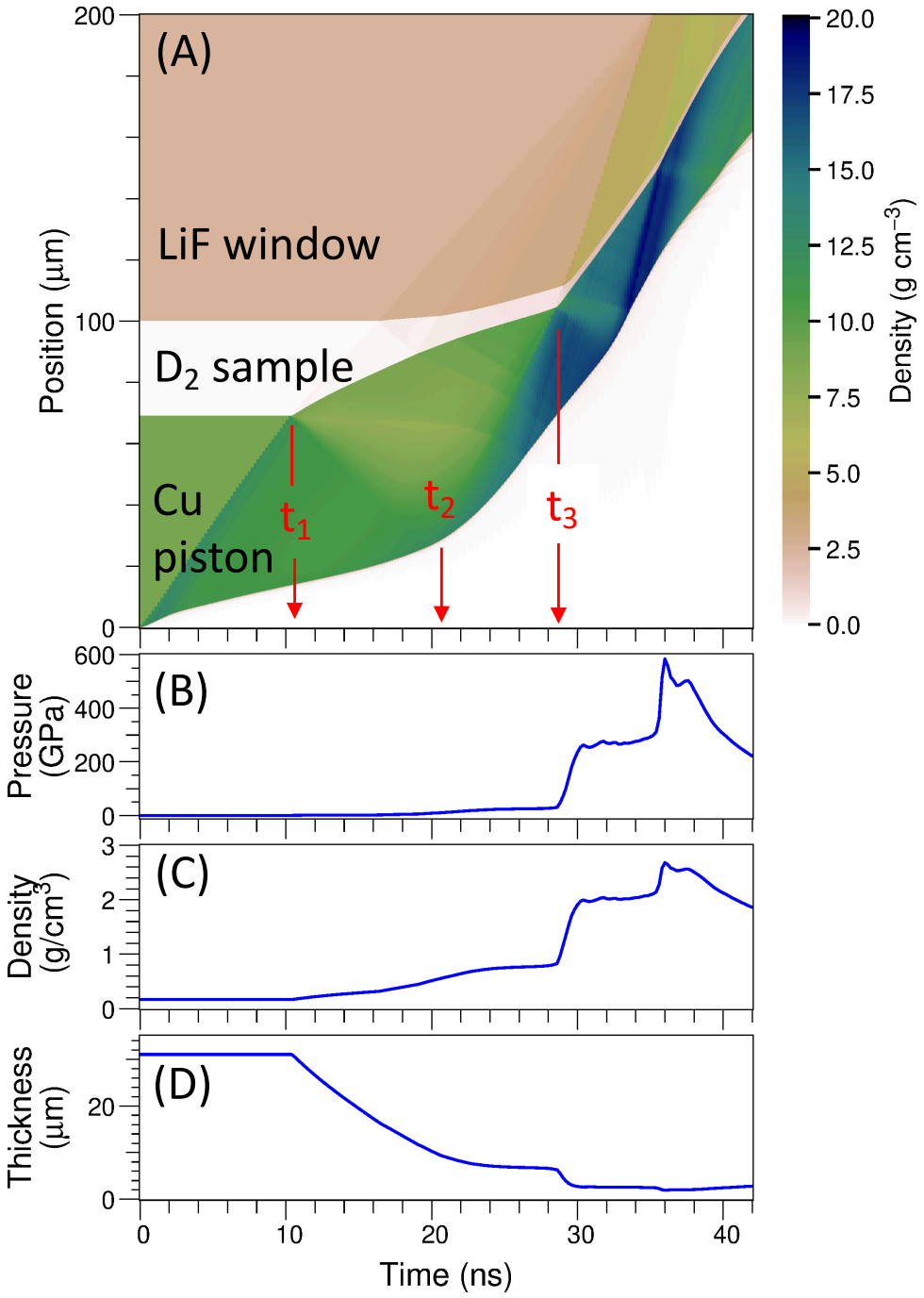

Fig. S4

(A) Representative result from a HYADES simulation of the density evolution in the target structure showing the main features of the compression process. Other frames are: (B) average pressure in the D_2 sample layer, (C) average density, and (D) thickness of the layer.

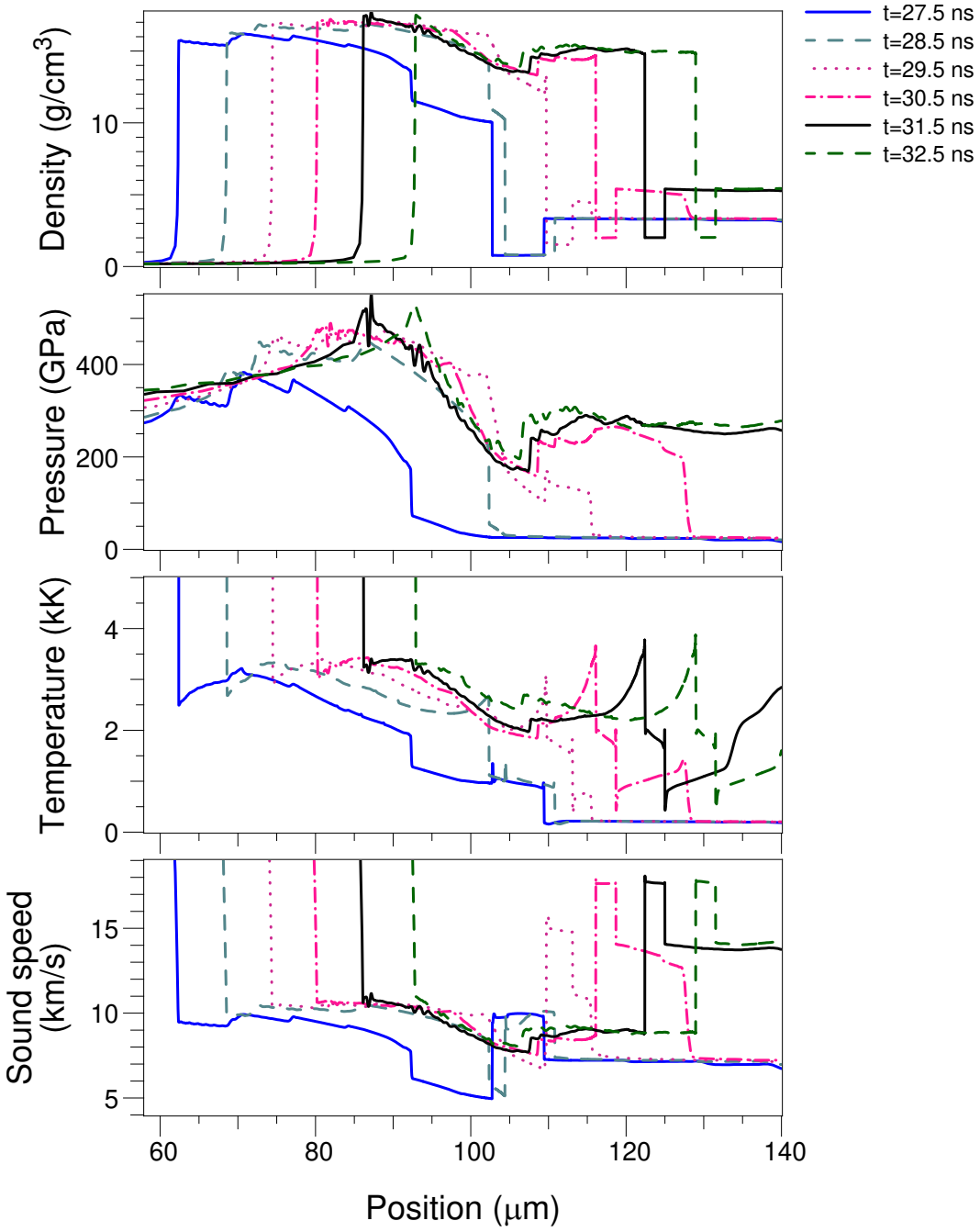

Fig. S5

Snapshots of density, pressure, temperature and sound speed from the computation shown in Fig. S4, focusing on details around the IM transition (second reverberation sequence). The average position of the deuterium sample moves from 105 μm to 130 μm, while the pressure rises from 25 GPa to 270 GPa. At all times shown the sound speed of the sample is about twice the sound speed in the adjacent Cu and 30% larger than the sound speed in the LiF window.

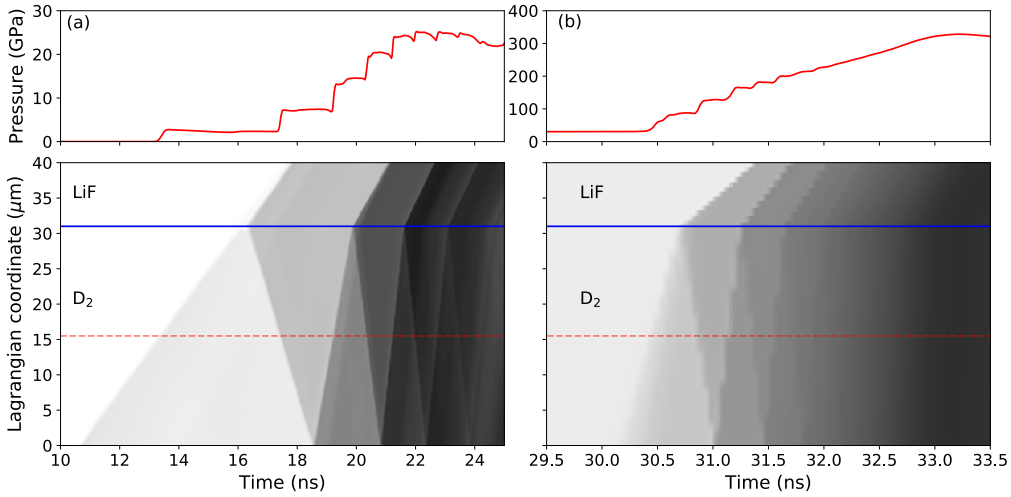

Fig. S6

Details of the reverberation sequences in the layer: (A) the initial reverberation sequence in the deuterium layer; and, (B) second reverberation sequence followed by ramp. The interface between LiF window and D_2 layer is indicated by the blue lines. In this calculation the Cu/D_2 interface is set to lagrangian coordinate = 0. The upper frames show pressure versus time in the center of the layer (along red dashed line); lower frames show color-scale representations of the pressure history throughout the entire sample, revealing the reverberation pattern. Color scales in (A) and (B) are matched to the pressure axis limits in the upper plots. The plots were extracted from detailed simulations that were matched to the observed velocity histories of the Cu piston and LiF window interface.

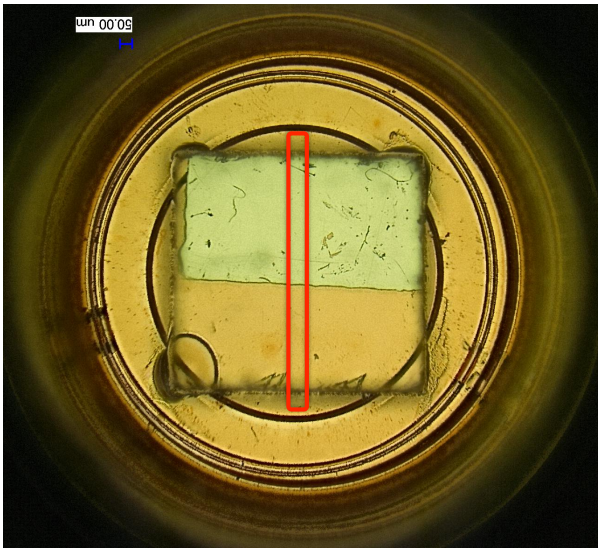

Fig. S7

View of the sample package as seen from the VISAR line-of-sight. The lower sections of the 1 mm square LiF window provides a view of the Cu piston surface and the upper section has the Al flashing place at the deuterium/LiF interface. A central chord is projected onto the slit of the VISAR streak camera as indicated by the red rectangle.

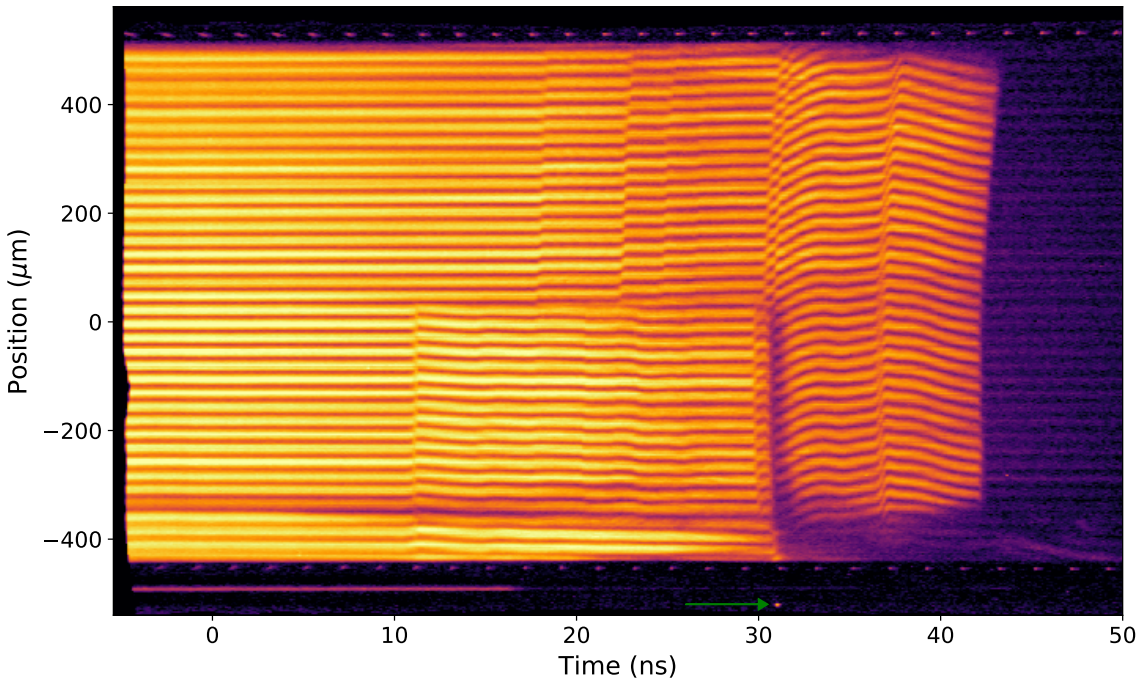

Fig. S8

Raw streak recording (displayed with logarithmic color scale). Timing combs (high precision 0.5 GHz clock reference) are recorded along the top and bottom edges of the record. An absolute timing fiducial is indicated by the green arrow.

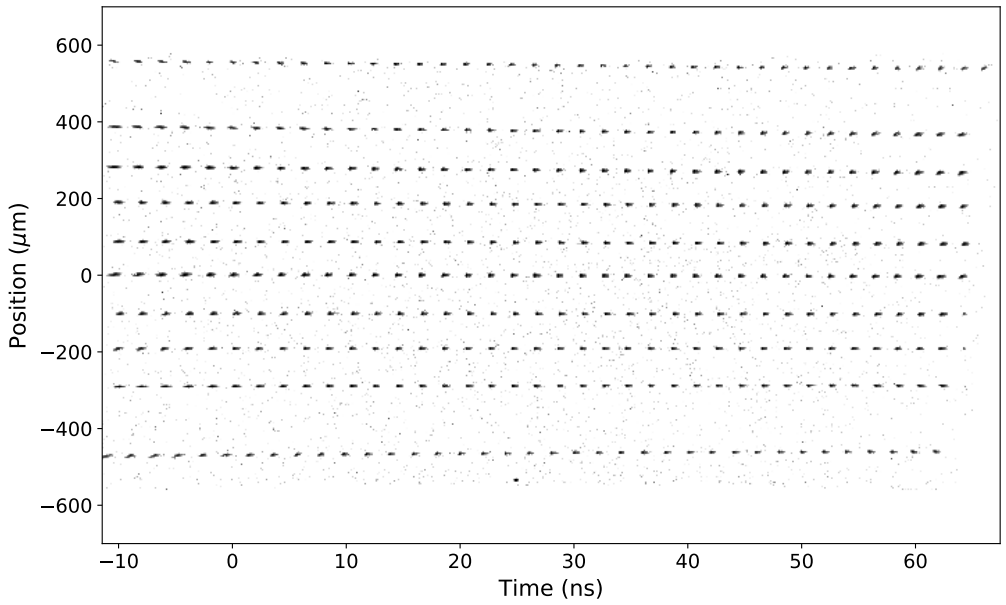

Fig. S9

Example of a high precision position-time calibration acquired before each experiment on each streak camera.

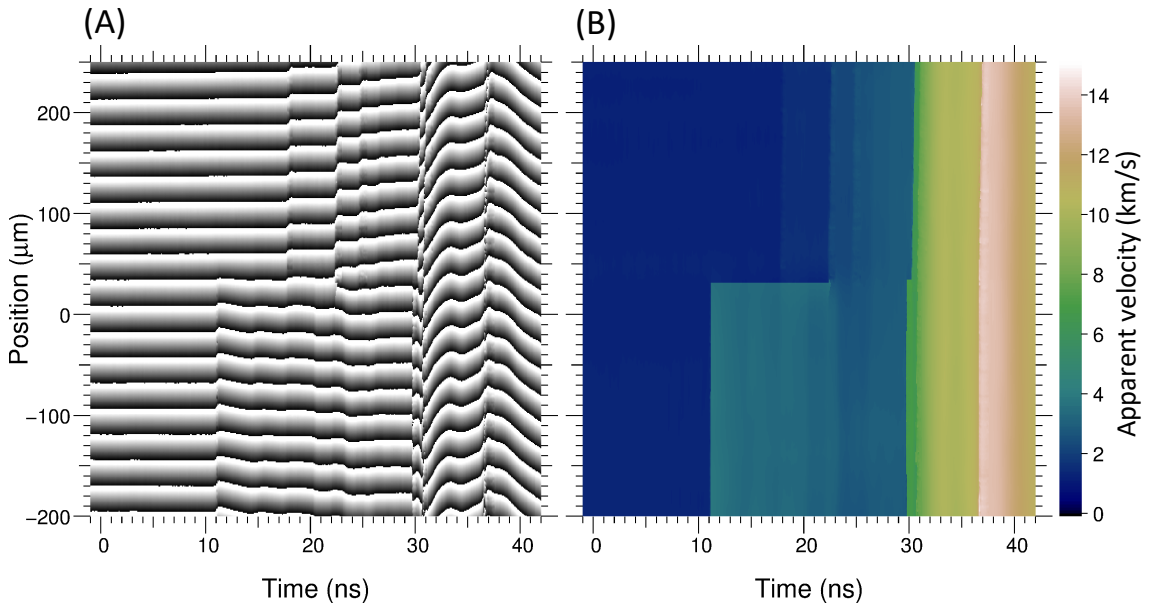

Fig. S10

(A) Example of the wrapped phase corresponding to the raw data shown in Fig. S8. (B) Velocity map extracted from the phase.

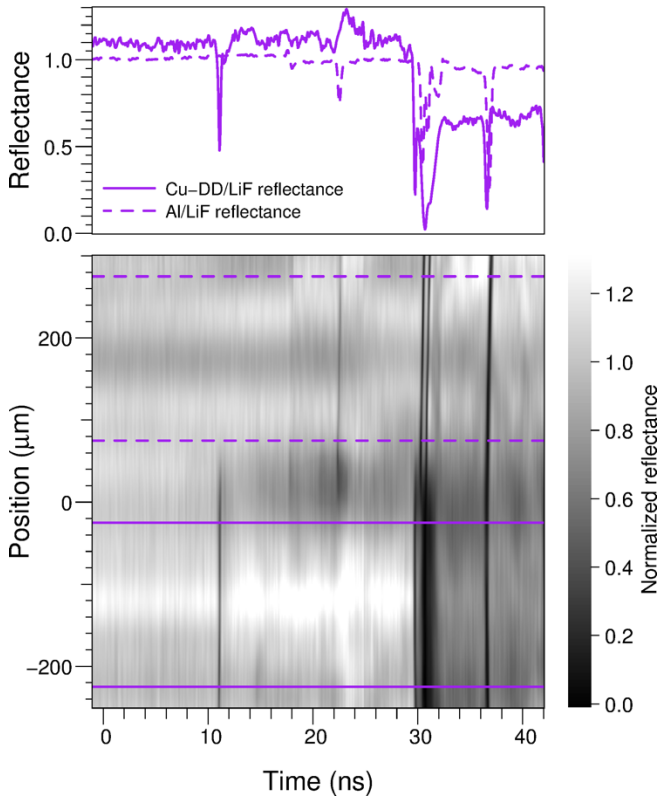

Fig. S11

Upper frame shows the time varying reflectance averaged over a pair of 200 μm wide segments of the Al/LiF (dashed) and Cu/D_2–DD/LiF (solid) interfaces repectively. Lower frame shows the normalized reflectance map from which these profiles were extracted based on the raw data shown in Fig. S8; integration regions are denoted by the dashed and solid pairs of lines. The short drops in reflectance of duration ~200 ps are artifacts caused by velocity transients occurring on time scales comparable to or faster than the detector time resolution (omitted from the reflectivity analysis). The Cu piston surface has higher initial reflectivity than the Al/LiF interface due to the higher reflectivity of Cu at the 660 nm probe wavelength. Long wavelength spatial variations of ±15% in the reflectance map are present owing to spatial variations in the optical quality of the target package components and in the laser illumination pattern (including laser speckle). These variations appear at low frequencies owing to averaging by the CWT processing algorithms; they are further reduced by using the wide spatial integration regions.

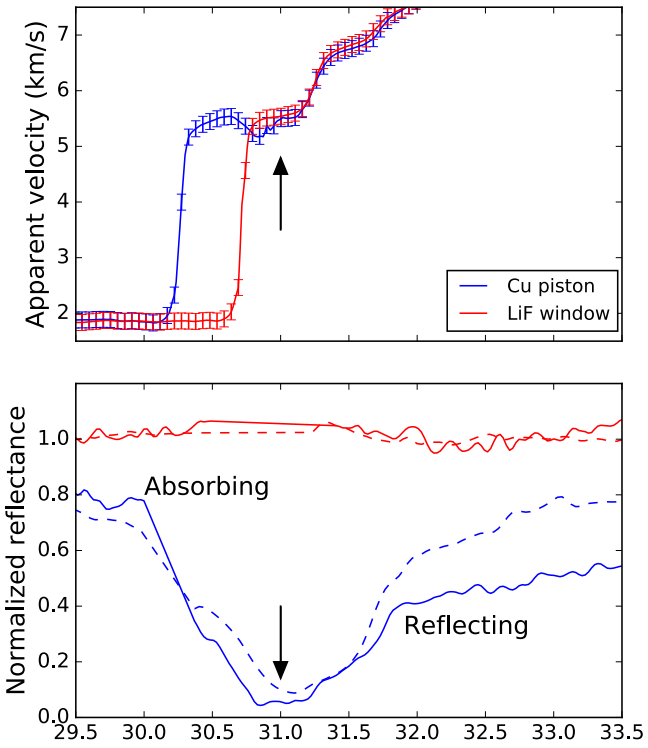

Fig. S12

Upper frame shows the apparent velocities observed from the two parts of the target, and the arrow indicates the time t_M when the two velocities match. Lower frame: the time t_M is simultaneous with the minimum in the reflectance signal. In the lower frame dashed and solid curves correspond to independent results extracted from the two detection channels.

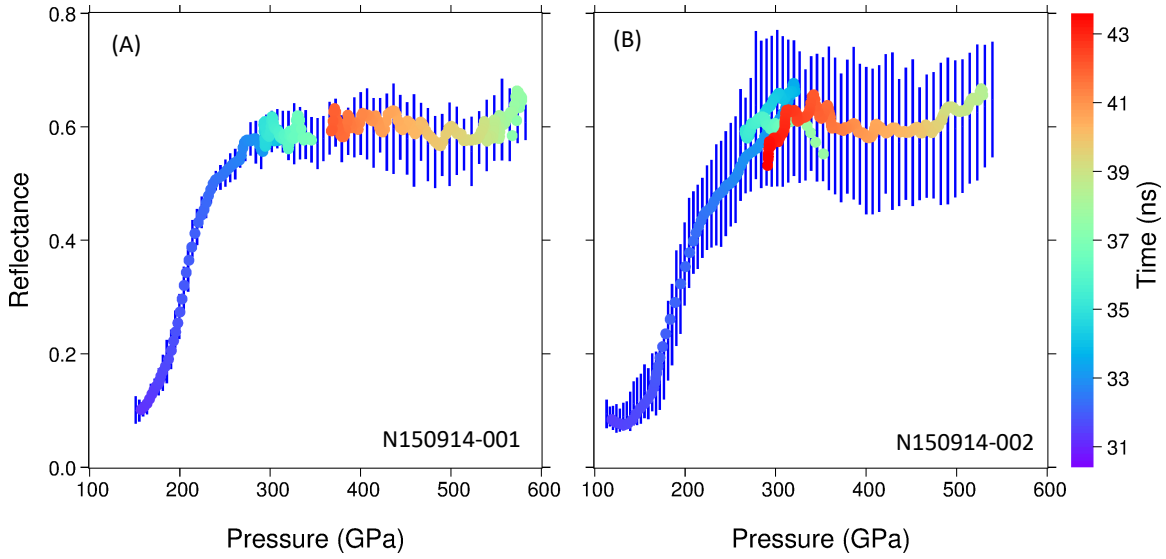

Fig. S13

Reflectance measurements during the IM transition and peak compression with the time history of the measurement encoded according to the color bar on the right. The signals do not display any apparent time-dependence (hysteresis) such as was observed in the experiments of Knudson *et al.*

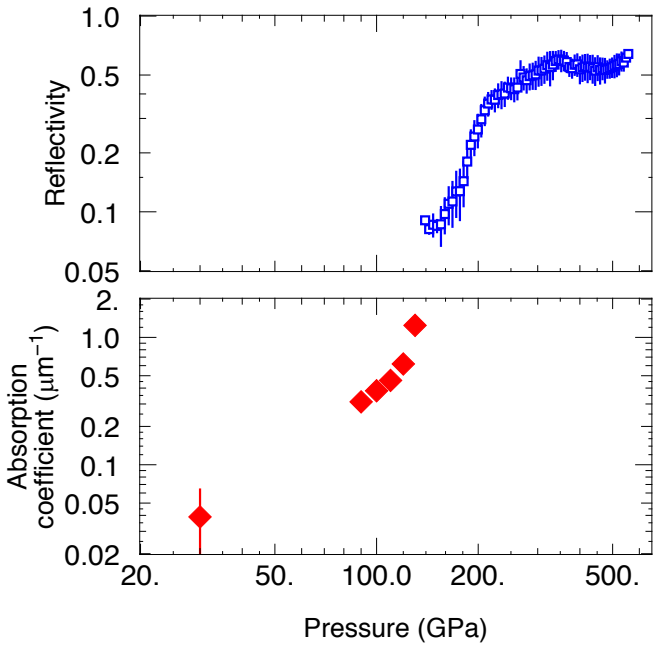

Fig. S14

Reflectivity and absorption coefficient extracted from the reflectance map. No states are sampled between the end of the first reverberation sequence ($P \sim 30$ GPa) and the start of the second reverberation sequence ($P \sim 80$ GPa).

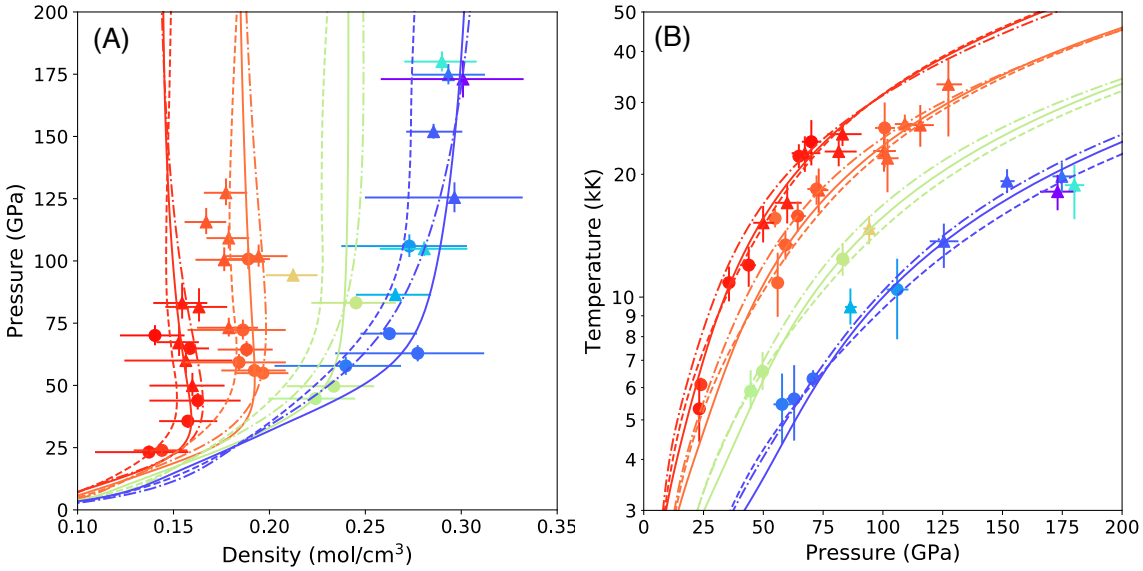

Fig. S15

(A) Pressure density comparison of precompressed Hugoniots computed from the Caillabet *et al.*(*32*) (solid), Kerley (*31*) (dashed) and Correa *et al.*(*33*) (chain-dashed) with pre-compressed Hugoniot data reported in Brygoo *et al.* (*34*) (originally reported in Loubeyre *et al.* (*12*)). Initial densities for the model Hugoniots are 0.033 (red), 0.044 (orange), 0.061 (green) and 0.081 (blue) mol/cm^3, initial temperature is 295 K. (B) Comparison of the same model Hugoniots and data on the temperature-pressure plane.

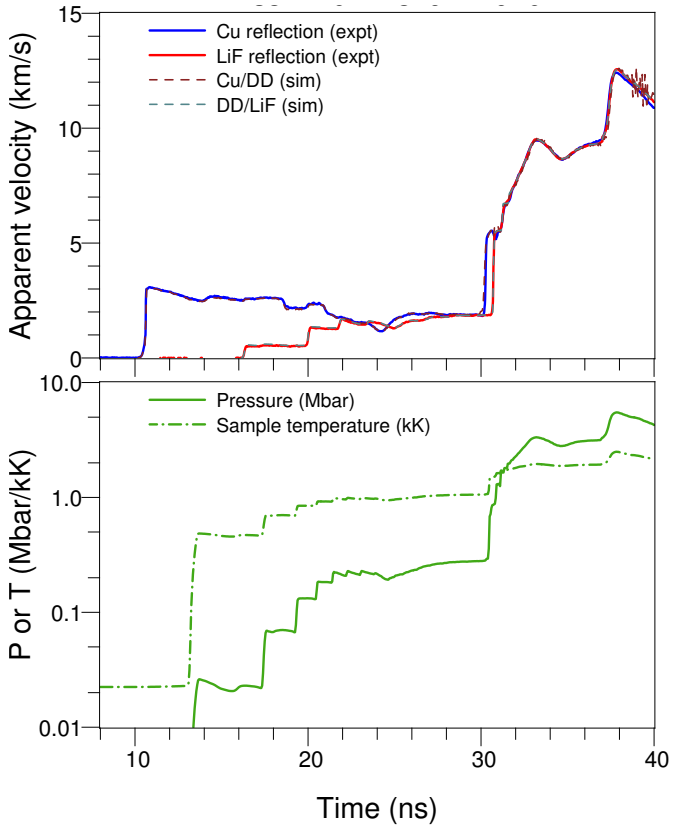

Fig. S16

Upper frame: observed and simulated apparent velocities for the two optical paths observed in experiment of N150914-002. Lower frame: pressure and temperature time histories for a Lagrangian element in the middle of the sample layer.

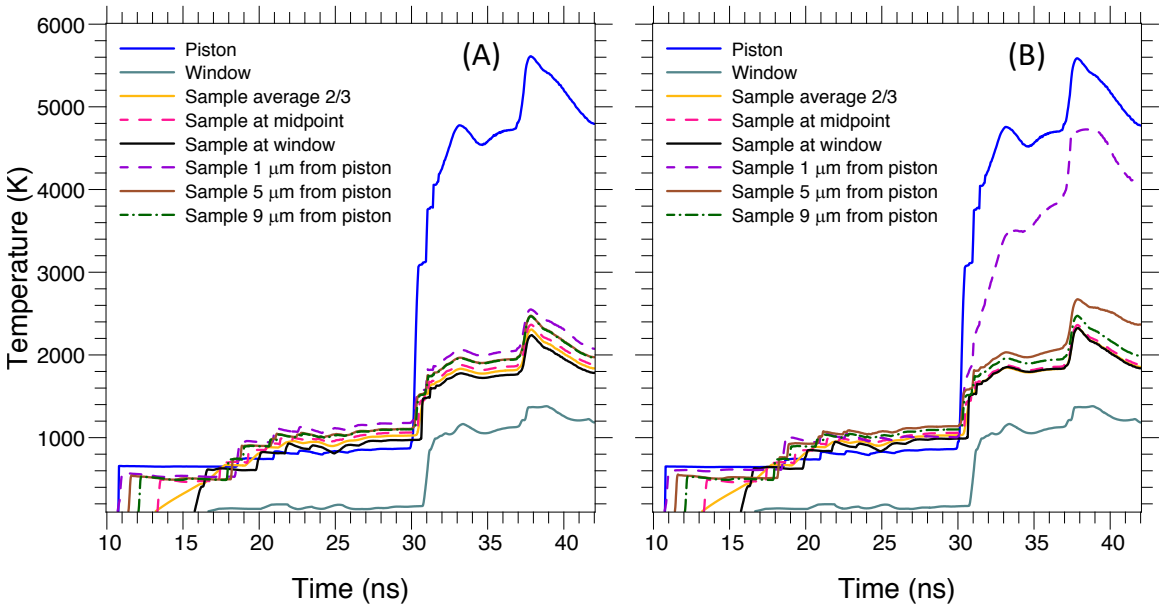

Fig. S17

Temperature history of the piston surface, the LiF window and the sample layer for N150914-002 using the Kerley EOS model for deuterium: (A) simulated with no heat conduction; and, (B) with heat conduction. The label "average 2/3" refers to the average temperature over 2/3 of the full thickness of the layer adjacent to the window. The other curves refer sample elements with initial Lagrangian positions at the window, the midpoint and at 1, 5, and 9 μm from the piston (after 10-fold compression these distances are 10 times smaller in real space).

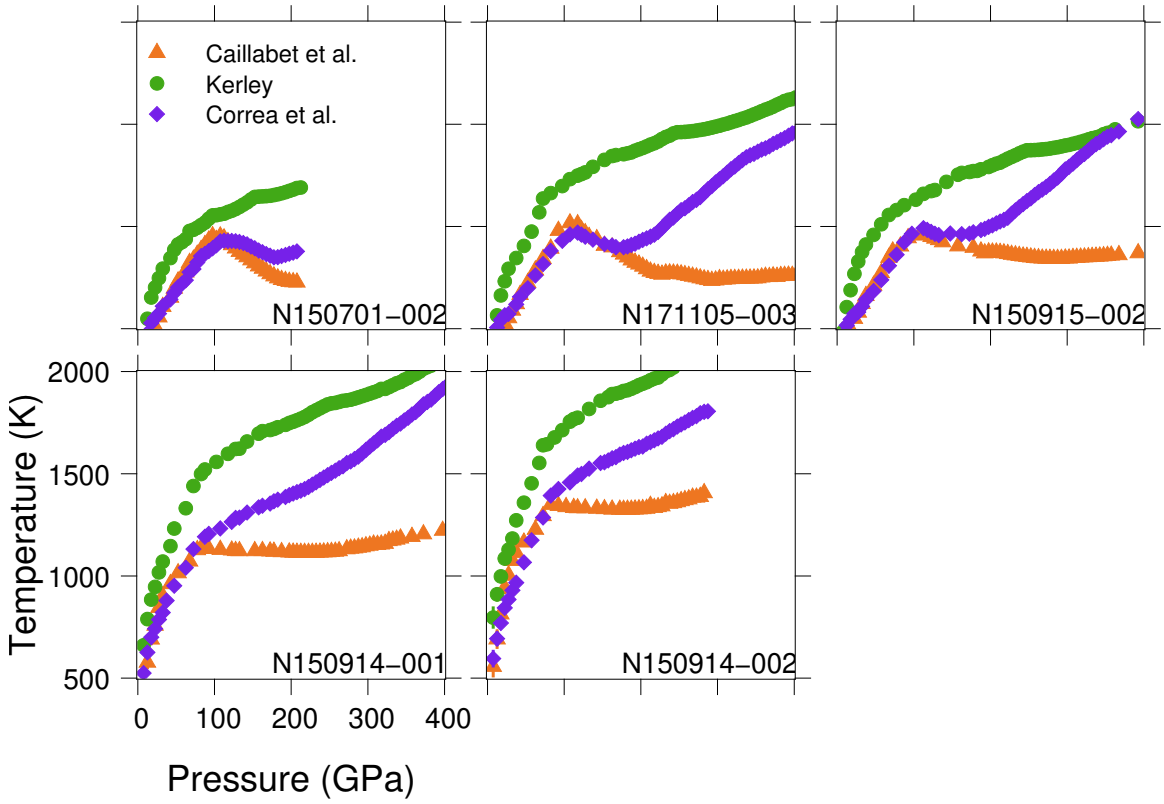

Fig. S18

Temperature-pressure paths for all five experiments and three global equation of state models for deuterium.

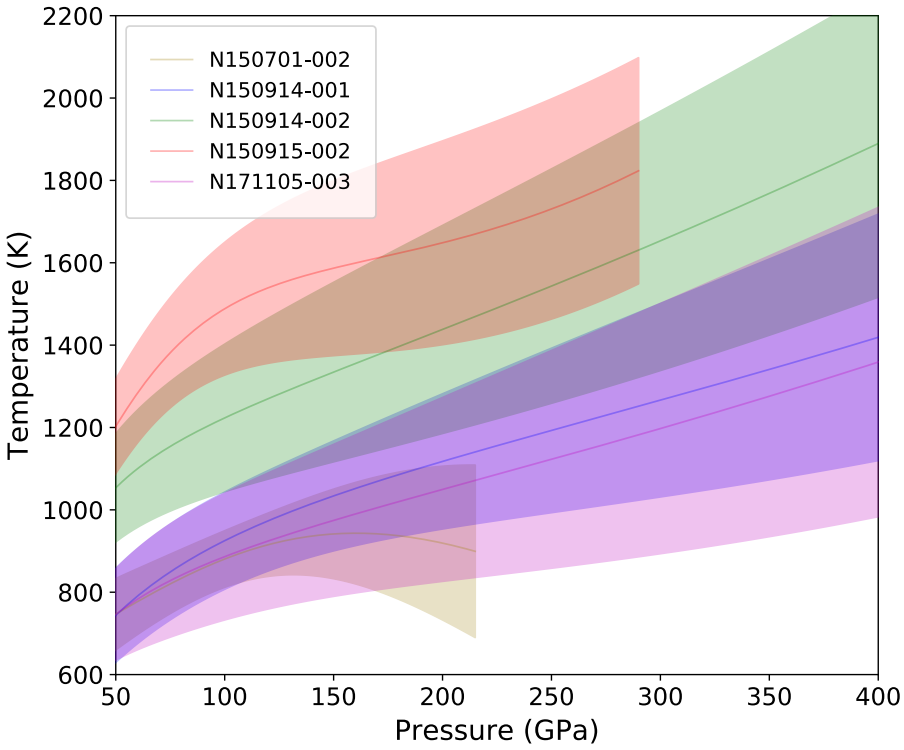

Fig. S19

Estimated temperature-pressure paths for the five experiments. The upper and lower bounds are estimated from the spread among the EOS models; solid curves are mean values.

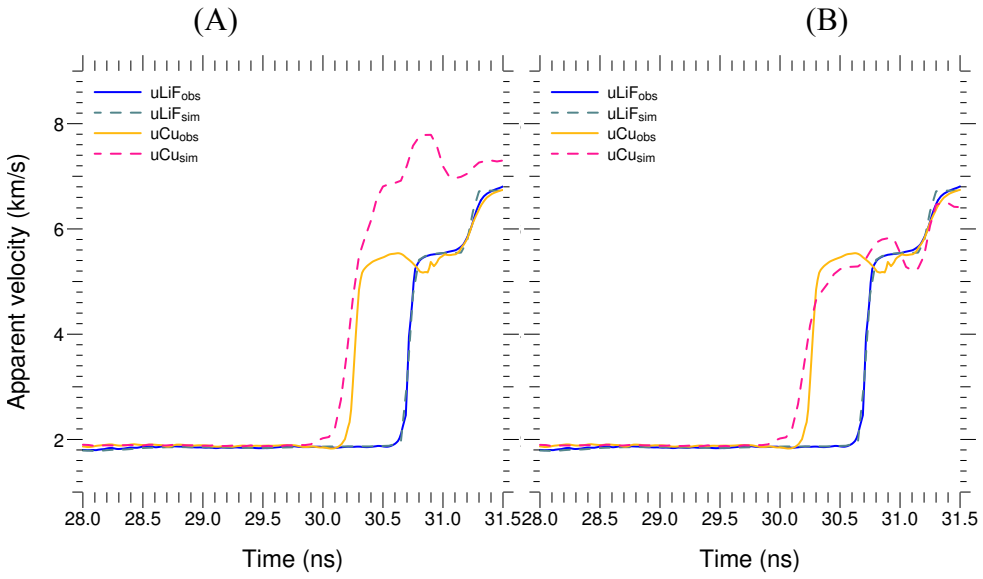

Fig. S20

(A) Apparent velocities from converged simulations for N150914-2 assuming an extrapolated Dewaele fit for the refractive index of deuterium; (B) assuming the modified form of equation (4) for the refractive index.

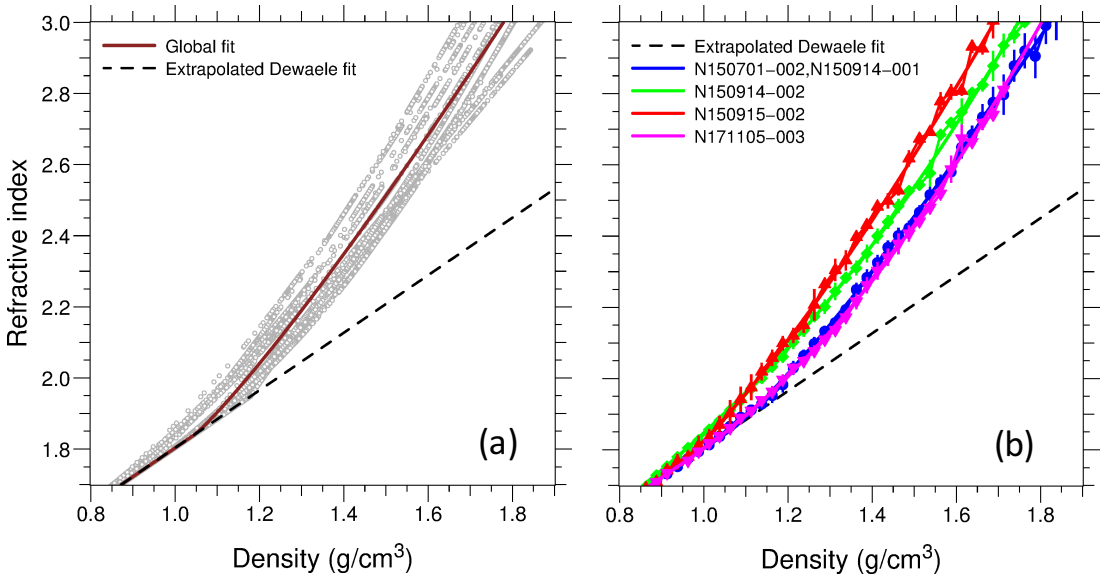

Fig. S21

(A) Ensemble of 15 refractive index fits as a function of density optimized to match the simulated to observed apparent velocities; also plotted is an averaged global fit. (B) Refractive index fits separated according to experiment (three simulations per experiment). The refractive index exceeds 3 above approximately 1.7 g/cm^3 density and displays a systematic temperature dependence.

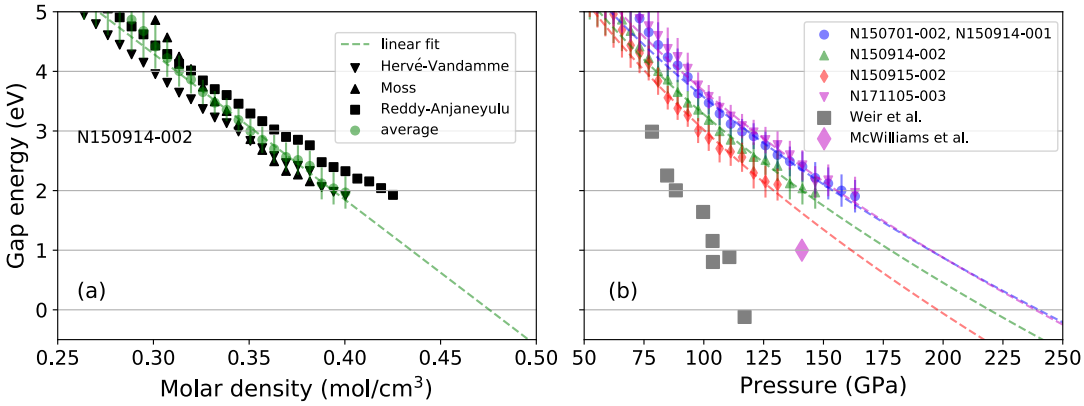

Fig. S22

(A) Estimated band gap based on refractive index data and empirical formulas of Moss, Reddy & Anjaneyulu and Hervé & Vandamme for one of the experiments (see text for references). The linear fit as a function of density was determined from a global fit to the results from all three empirical formulas for density > 0.25 mol cm^{-3}. (B) Estimated band gaps (with extrapolation of the linear density fit) as a function of pressure for all of the experimental cases corresponding to a range of temperatures: 1000 K (N150701-002, N150914–001), 1320 K (N150914-002), 1550 K (N150915-002), and 1000 K (N171105-003). Also shown are the estimated band gap data of Weir *et al.* near 3500 K and McWilliams *et al.* at 2400 K.

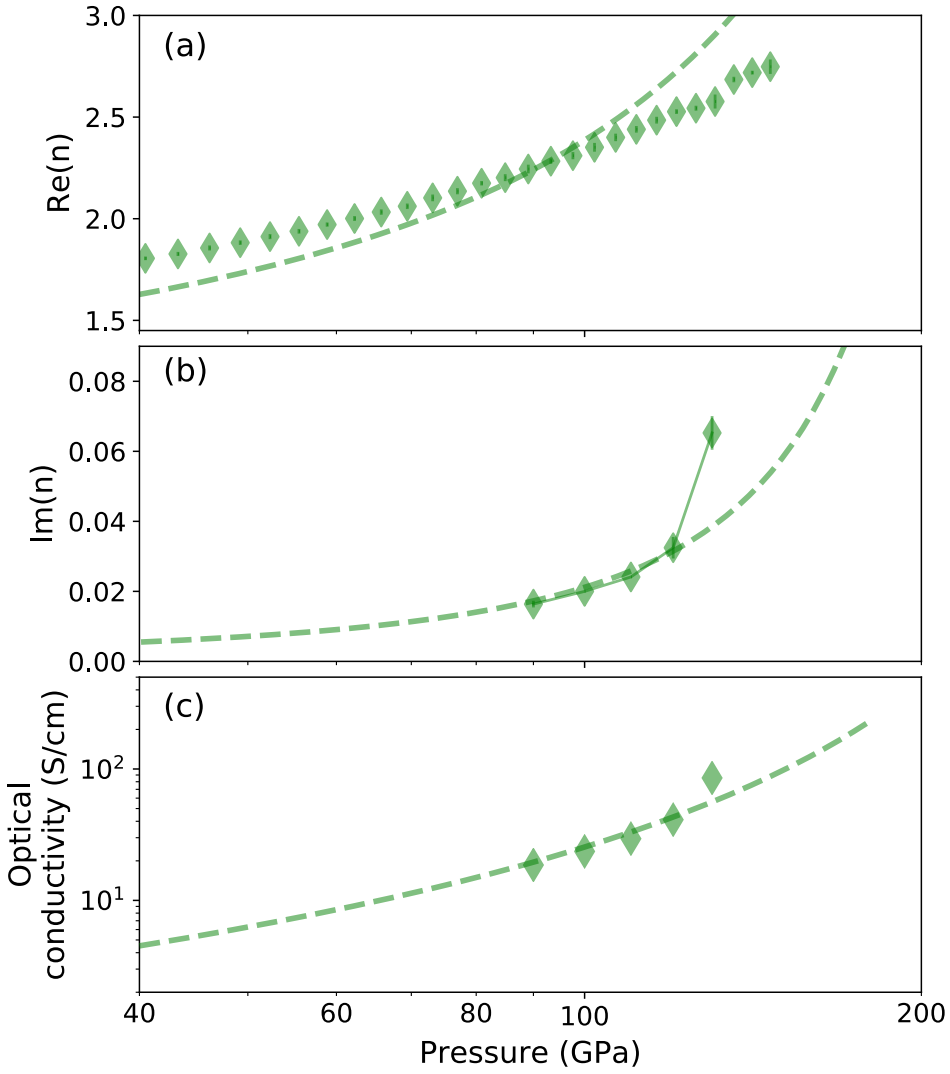

Fig. S23

(A) Real part of the index of refraction inferred from experiment N171105-003 (symbols) and real part of the index from Lorentz model (dashed curve). (B) Imaginary part of the index inferred from the data (symbols) and corresponding Lorentz model (dashed curve). (C) Optical conductivity inferred from the experiment (symbols) compared with the Lorentz model (dashed curve). Similar behavior is found for the other experiments.

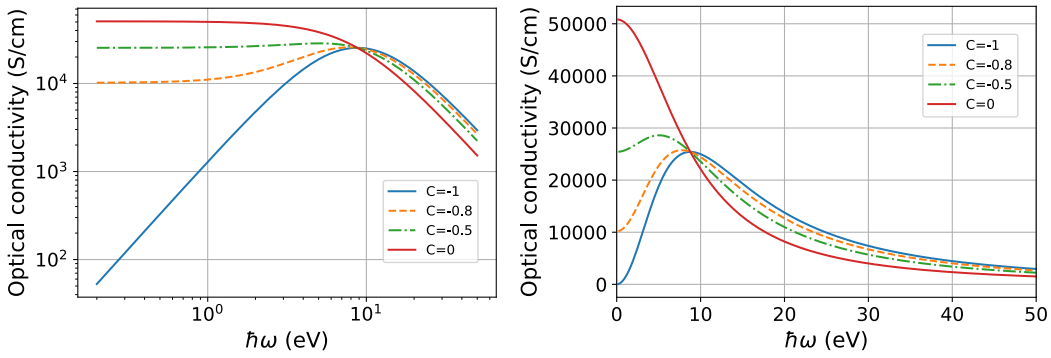

Fig. S24

Optical conductivity computed with the Smith-Drude model for $\tau = 0.075$ fs, $\rho = 2.0$ g/cm^3 and several cases of the backscatter parameter C indicated in the legend. Left and right frames show identical curves with logarithmic scales on the left, linear scales on the right.

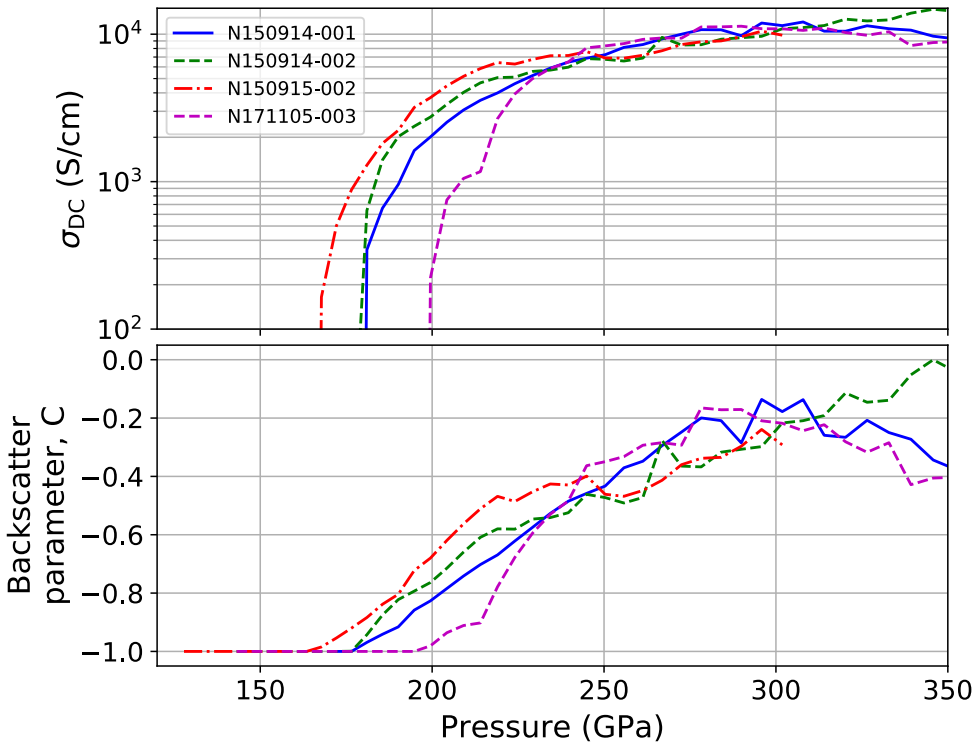

Fig. S25

Upper: DC conductivity extracted from the reflectivity data using the Smith-Drude model. Lower: Corresponding backscatter parameter C. The parameters in the Smith-Drude model were: $\tau = 0.075$ fs and N evaluated with the expression given in equation (7).

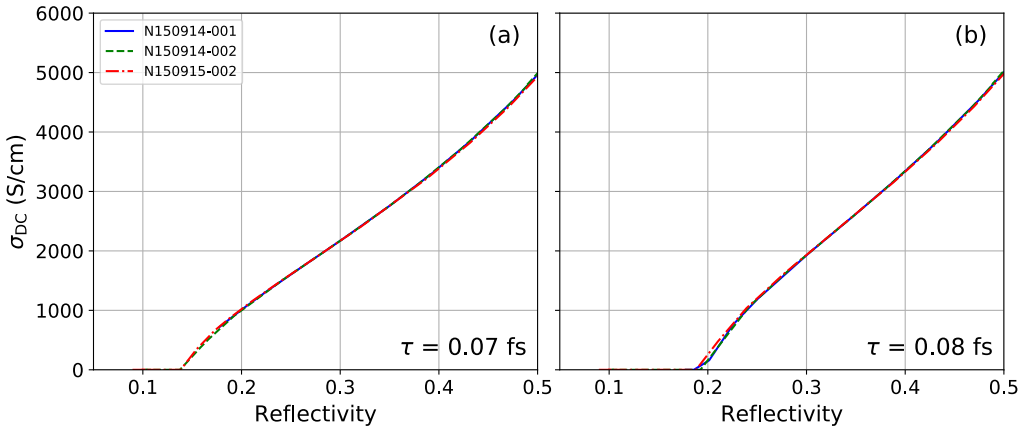

Fig. S26

(A) DC conductivity from the Smith-Drude model as a function of the reflectivity for τ=0.07 fs. (B) DC conductivity from the Smith-Drude model as a function of the reflectivity for τ=0.08 fs.

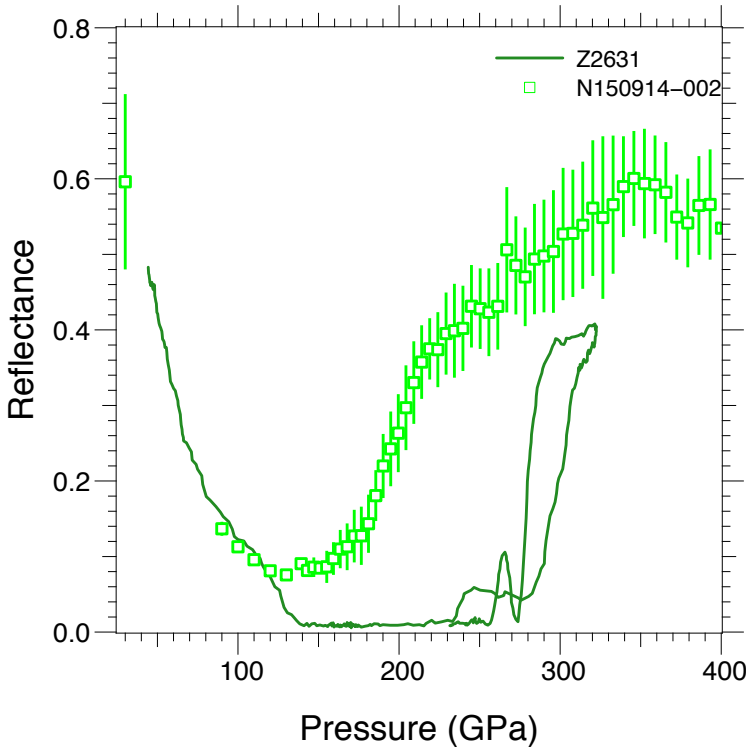

Fig. S27

Comparison of reflectance signals from Z and NIF experiments (scaled to account for the Al/LiF reference). Early time reflectances (P < 120 GPa) are comparable, while for P > 120 GPa (and t > 2650 ns) the reflectance observed in the Z experiments are systematically lower than the NIF, e.g. R~1% in the range 120 < P < 240 GPa, where ~10% reflectivity is expected.

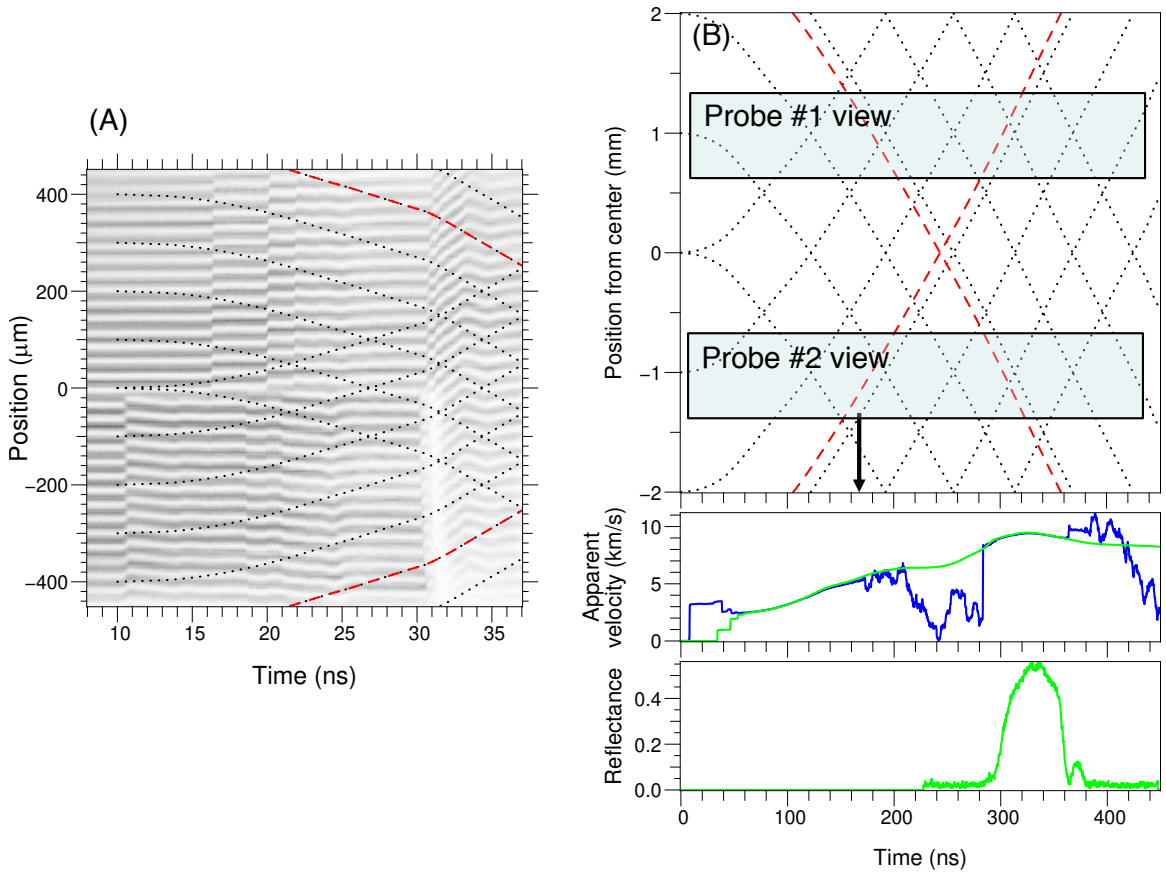

Fig. S28

(A) Characteristics diagram for N150914-2, computed using the Kerley EOS model using the time-dependent sound speed, showing acoustic trajectories in the deuterium sample (dotted) launched at 100 μm spacing starting at t = 10 ns (not all are shown). Dashed red characteristics launched from the edges of the LiF window enclose the inertially confined sample domain. (B) Characteristics diagram for one of the Z experiments, computed using the Kerley EOS model and launched at 1 mm spacing. The red dashed characteristics, launched from the edges of the LiF window, pass through the probe field of view at 170 ns (heavy black arrow) and reach the center near 240 ns.

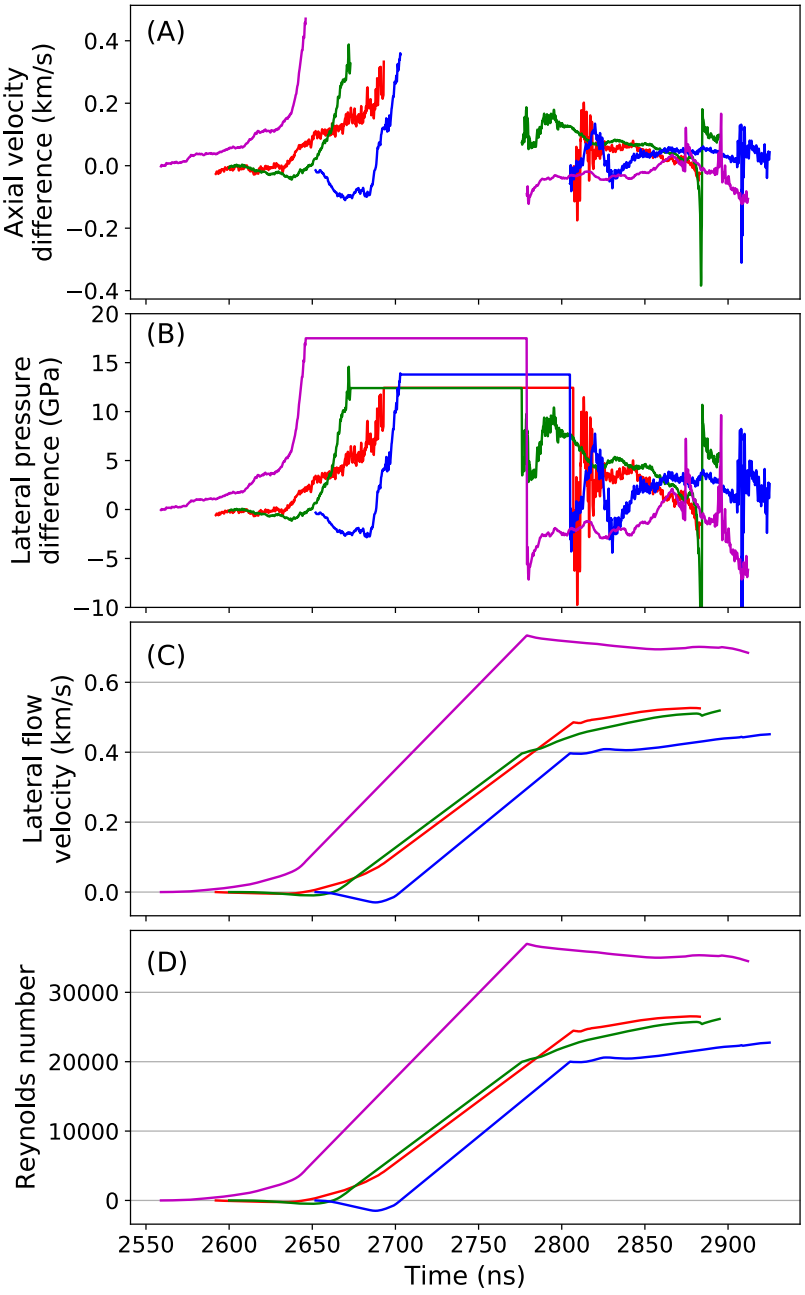

Fig. S29

(A) Difference in axial velocity between the LiF window and the D_2 VISAR probes. (B) Pressure difference between the two probes. (C) Flow velocity in the sample layer estimated by integrating equation (10) over the signals in (B). (D) Reynolds numbers associated with the lateral flows. Colors are chosen to match the colors used in Knudson *et al.*

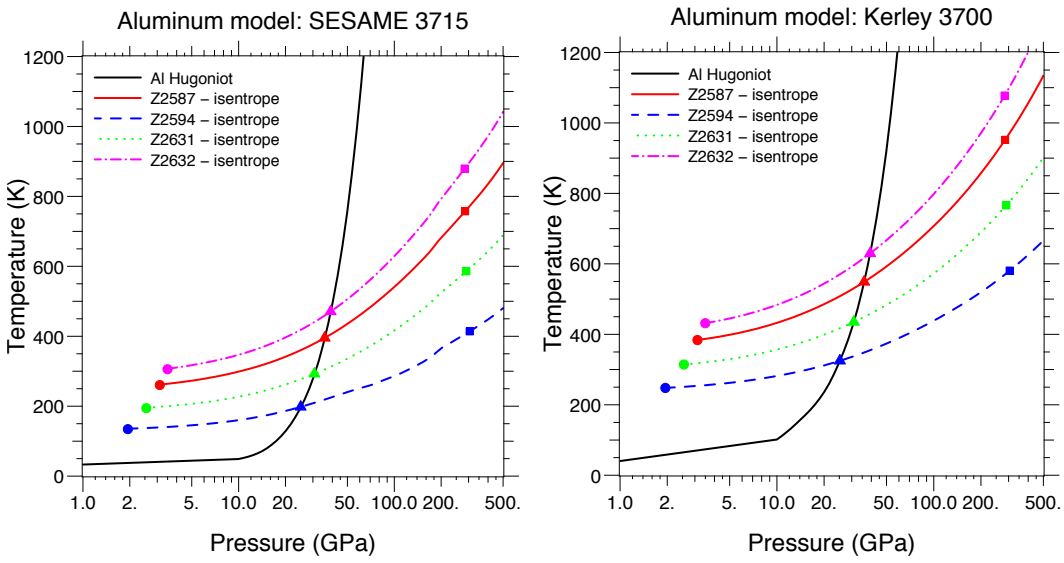

Fig. S30

Al piston temperatures estimated from the first shock states in the four Z experiments for the SESAME 3715 model (left) and Kerley 3700 model (right). Triangles show the incident shock stress level along the principal Hugoniot, circles are the release states matched to the initial shock launched in the deuterium, and squares show the estimated temperatures at the reported IM transition pressures. Curves connecting the points are isentropes.

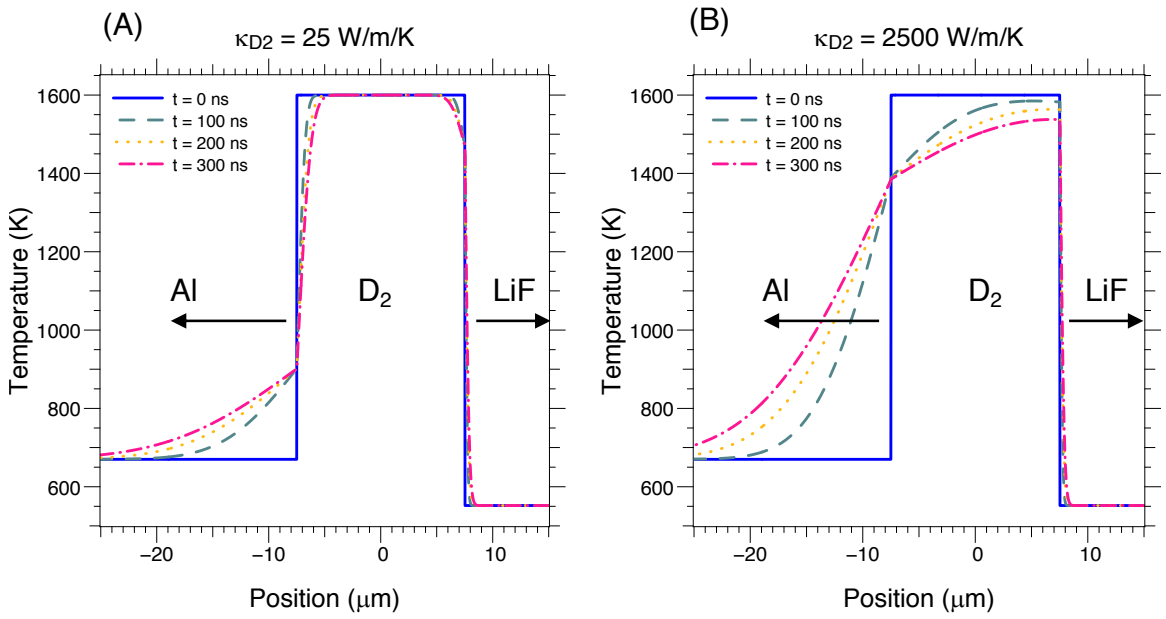

Fig. S31

Temperature evolution as a function of time in the Al piston (position < -8μm), the D_2 layer (center position) and the LiF window (position > 8 μm). The cases are: (A) thermal conductivity κ_{D2} = 25 W/m/K in the deuterium and (B) thermal conductivity κ_{D2} = 2500 W/m/K.

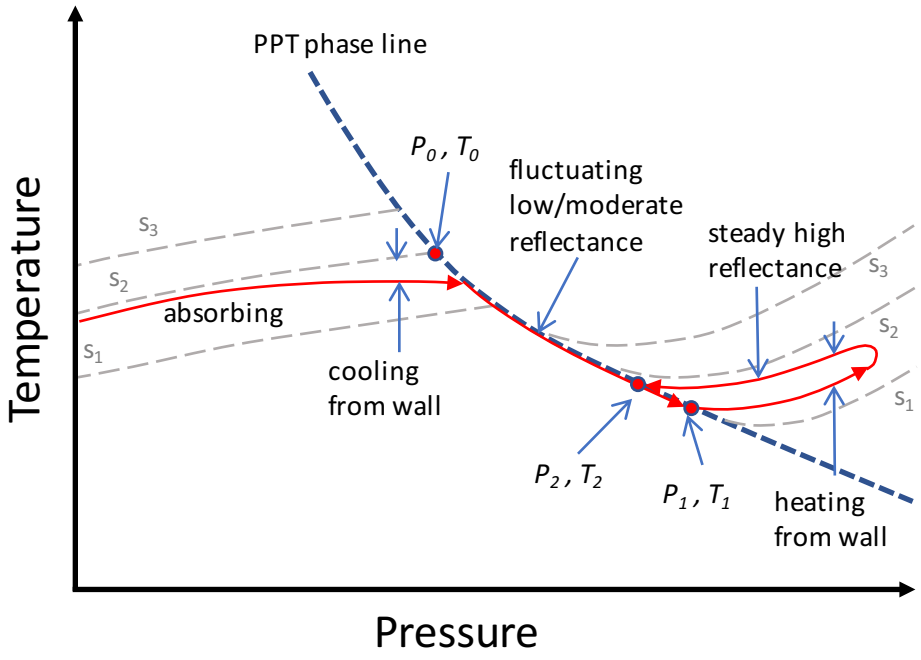

Fig. S32

Features of the ramp compression path through *P*-*T* space in the Z experiments. A family of isentropes with entropies s_1, s_2 and s_3 are sketched (grey-dashed curves) as they pass through the first order IM transition (heavy dashed curve). The isentrope s_2 intersects the PPT line at P_0, T_0. An experiment initially launched at entropy s_2 follows the solid red path. Temperature at the intersection with the PPT line is reduced by ~100 K owing to cooling from the Al piston wall. Further compression cools the sample because of latent heat. Transformation is complete at P_1, T_1. Near peak compression the sample is reheated by the Al piston wall, and the path re-enters the mixed phase region at P_2, T_2. The temperature differences are T_0 -[T_1 or T_2] $\gtrsim$ 700 K (section 5h), and corresponding pressure differences are [P_1 or P_2] – P_0 ~ 100 GPa.

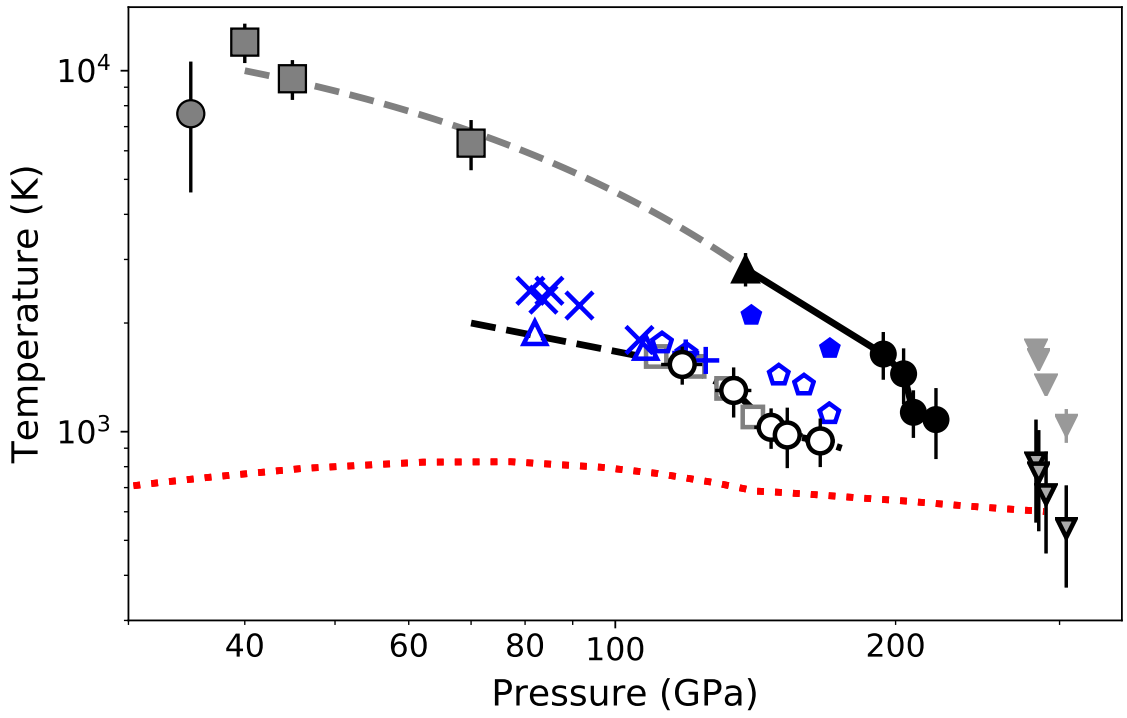

Fig. S33

Extended phase diagram of H2/D2 at high P-T conditions. Symbols indicate the results of experiments. Present results: threshold where optical absorption coefficient exceeds 1 μm-1 at photon energy of 1.9 eV (black open circles and black dashed line); and, points where the D_2-LiF interface reflectivity exceeds R=30% (black solid circles). The thick black curve connects these points to the metallization transition, $\sigma \approx 2000$ S/cm, identified by Weir *et al.* (*36*) (solid black triangle). Previous experimental results on H_2: Ohta *et al.* (*18*) (x) and Dzyabura *et al.* (crosses) (*17*) both from heating curve analyses of laser-heated DACs; Zaghoo *et al.* (open and solid pentagons) from DAC optical transmission and reflectance (*19*, *21*); McWilliams *et al.* determination of the onset of absorption from transient DAC optical transmission measurements (open triangles) (*20*); melting measurements of Zha *et al.* (*23*) (chain-dashed red line). Previous results on D_2: Knudson *et al.*, absorption onset for 2.3 eV photon (open squares) (*22*); Knudson *et al.*, reported reflectivity jumps (inverted gray triangles) (*22*); and, after adjustment of *T* based on reinterpretation (black-edged gray inverted triangles, Table S3). The dashed extension of the metallization boundary connects to single-shock compression data: reflectivity and temperature at 50% of peak reflectivity along the D_2 principal Hugoniot (*11*, *107*, *108*) (grey filled circle); and along precompressed Hugoniots (Loubeyre *et al.* (*12*), gray-filled squares).

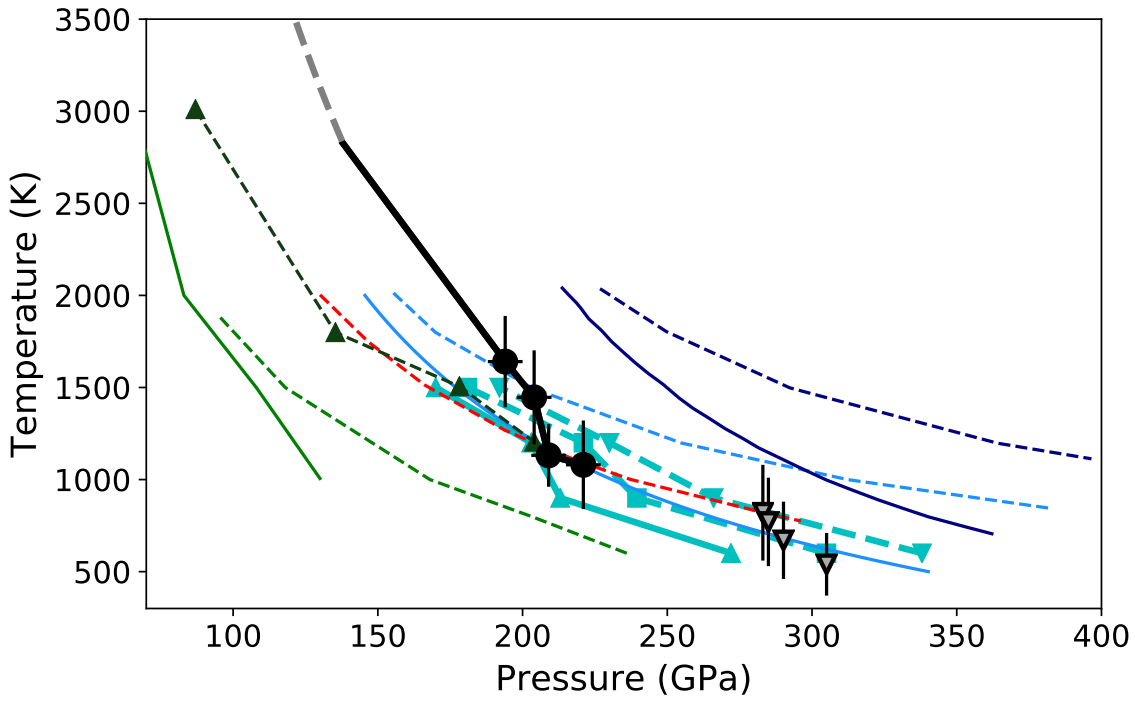

Fig. S34

Theoretical results for the IM transition, as summarized in Pierleoni *et al.* (*15*) Computations with density functional molecular dynamics using different functionals include: PBE with quantum corrections (green solid), PBE with classical ions (green dashed), HSE (dashed red), vdW-DF1 with quantum corrections (light blue solid), vdW-DF1 with classical ions (light blue dashed), vdW-DF2 with quantum corrections (dark blue solid) vdW-DF2 with classical ions (dark blue dashed). Also shown are the coupled electron-ion Monte Carlo calculations of Pierleoni *et al.* (*15*) or hydrogen (cyan trangles & thick solid line) and classical protons (cyan inverted triangles & thick dashed line) and the quantum Monte-Carlo calculations by Mazzola *et al.* (*16*) (dark green triangles & dashed line). The red chain-dashed curve corresponds to the melt curve measured by Zha *et al.* (*23*) The solid black circles and inverted black-edged grey triangles are as in Fig. 3 and Fig. S33.

Table S1.

Incident shock state and *P-T* at the points when the absorption coefficient reaches a threshold of 1 μm^{-1} and when the D/LiF interface reflectivity exceeds 30%. These points are plotted in Fig. 3.

	Initial shock state		Onset of absorption ($\alpha = 1/\mu m$)			Insulator-metal transition		
Experiment	Initial D_2 u_p (km/s)	Initial P (GPa)	V (km/s)	P (GPa)	T (K)	$V_{R>30\%}$ (km/s)	$P_{R>30\%}$ (GPa)	$T_{R>30\%}$ (K)
N150701-2	2.31	1.79	6.41±0.2	166±6	940±170	N/A	N/A	N/A
N171105-3	2.39	1.89	6.10±0.2	153±6	980±200	7.62±0.2	221±6	1080±240
N150914-1	2.58	2.15	5.95±0.2	147±6	1030±150	7.37±0.2	209±6	1130±170
N150914-2	3.08	2.92	5.61±0.2	134±6	1300±210	7.23±0.2	204±6	1450±260
N150915-2	3.36	3.30	5.43±0.2	118±6	1540±200	7.04±0.2	194±6	1640±250

Table S2.

Incident shock state and temperature along isentropes evaluated for two different aluminum EOS models, producing estimates of the piston surface temperature during the Z experiments.

Experiment	Initial D_2 u_p (km/s)	First shock stress in Al (GPa)	Insulator-metal transition pressure (GPa)	Estimated T_{IM} of piston SESAME 3715 EOS model (K)	Estimated T_{IM} of piston Kerley 3700 EOS model (K)	T_{avg} (K)
Z2587	3.20	35.9	285	952	758	860±140
Z2594	2.43	25.1	305	581	414	500±120
Z2631	2.85	30.8	290	766	586	680±130
Z2632	3.42	39.2	283	1078	880	980±140

Table S3.

Published transition temperatures (from Knudson *et al.*) based on the original interpretation of the Z experiments; and, revised according to Clausius-Clapeyron estimates.

Experiment	Insulator-metal transition pressure (GPa)	T_0 published (K)	T_1 revised (K)
Z2587	285	1600	770±240
Z2594	305	1150	540±170
Z2631	290	1420	670±210
Z2632	283	1700	820±260

References

1. J. M. McMahon, M. A. Morales, C. Pierleoni, D. M. Ceperley, The properties of hydrogen and helium under extreme conditions. *Rev. Mod. Phys.* **84**, 1607–1653 (2012).

2. N. W. Ashcroft, Metallic Hydrogen: A High-Temperature Superconductor? *Phys. Rev. Lett.* **21**, 1748–1749 (1968).

3. E. G. Brovman, Y. Kagan, A. Kholas, Properties of metallic hydrogen under pressure. *Sov. Phys. JETP*. **35**, 783 (1972).

4. E. Babaev, A. Sudbo, N. W. Ashcroft, A superconductor to superfluid phase transition in liquid metallic hydrogen. *Nature*. **431**, 666–668 (2004).

5. N. Nettelmann, A. Becker, B. Holst, R. Redmer, Jupiter Models with Improved Ab Initio Hydrogen Equation of State (H-REOS.2). *The Astrophysical Journal*. **750**, 52 (2012).

6. J. E. P. Connerney *et al.*, The Juno Magnetic Field Investigation. *Space Science Reviews*. **213**, 39–138 (2017).

7. G. É. Norman, A. N. Starostin, Thermodynamics of a dense plasma. *Journal of Applied Spectroscopy*. **13**, 965–967 (1970).

8. W. Ebeling, W. Richert, Plasma phase transition in hydrogen. *Physics Letters A*. **108**, 80–82 (1985).

9. D. Saumon, G. Chabrier, Fluid hydrogen at high density: The plasma phase transition. *Phys. Rev. Lett.* **62**, 2397–2400 (1989).

10. S. T. Weir, A. C. Mitchell, W. J. Nellis, Metallization of Fluid Molecular Hydrogen at 140 GPa (1.4 Mbar). *Phys. Rev. Lett.* **76**, 1860–1863 (1996).

11. P. M. Celliers *et al.*, Shock-Induced Transformation of Liquid Deuterium into a Metallic Fluid. *Phys. Rev. Lett.* **84**, 5564–5567 (2000).

12. P. Loubeyre *et al.*, Extended data set for the equation of state of warm dense hydrogen isotopes. *Phys. Rev. B*. **86**, 144115 (2012).

13. W. Lorenzen, B. Holst, R. Redmer, First-order liquid-liquid phase transition in dense hydrogen. *Phys. Rev. B*. **82**, 195107 (2010).

14. M. A. Morales, C. Pierleoni, E. Schwegler, D. M. Ceperley, Evidence for a first-order liquid-liquid transition in high-pressure hydrogen from ab initio simulations. *Proceedings of the National Academy of Sciences*. **107**, 12799–12803 (2010).

15. C. Pierleoni, M. A. Morales, G. Rillo, M. Holzmann, D. M. Ceperley, Liquid–liquid phase transition in hydrogen by coupled electron–ion Monte Carlo simulations. *Proceedings of the National Academy of Sciences*. **113**, 4953–4957 (2016).

16. G. Mazzola, R. Helled, S. Sorella, Phase Diagram of Hydrogen and a Hydrogen-Helium Mixture at Planetary Conditions by Quantum Monte Carlo Simulations. *Phys. Rev. Lett.* **120**, 025701 (2018).

17. V. Dzyabura, M. Zaghoo, I. F. Silvera, Evidence of a liquid–liquid phase transition in hot dense hydrogen. *Proceedings of the National Academy of Sciences*. **110**, 8040–8044 (2013).

18. K. Ohta *et al.*, Phase boundary of hot dense fluid hydrogen. **5**, 16560 (2015).

19. M. Zaghoo, A. Salamat, I. F. Silvera, Evidence of a first-order phase transition to metallic hydrogen. *Phys. Rev. B*. **93**, 155128 (2016).

20. R. S. McWilliams, D. A. Dalton, M. F. Mahmood, A. F. Goncharov, Optical Properties of Fluid Hydrogen at the Transition to a Conducting State. *Phys. Rev. Lett.* **116**, 255501 (2016).

21. M. Zaghoo, I. F. Silvera, Conductivity and dissociation in liquid metallic hydrogen and implications for planetary interiors. *Proceedings of the National Academy of Sciences* (2017), doi:10.1073/pnas.1707918114.

22. M. D. Knudson *et al.*, Direct observation of an abrupt insulator-to-metal transition in dense liquid deuterium. *Science*. **348**, 1455–1460 (2015).

23. C. Zha, H. Liu, J. S. Tse, R. J. Hemley, Melting and High P-T Transitions of Hydrogen up to 300 GPa. *Phys. Rev. Lett.* **119**, 075302 (2017).

24. N. Subramanian, A. F. Goncharov, V. V. Struzhkin, M. Somayazulu, R. J. Hemley, Bonding changes in hot fluid hydrogen at megabar pressures. *Proceedings of the National Academy of Sciences*. **108**, 6014–6019 (2011).

25. R. T. Howie, P. Dalladay-Simpson, E. Gregoryanz, Raman spectroscopy of hot hydrogen above 200 GPa. *Nat Mater*. **14**, 495–499 (2015).

26. W. J. Nellis, A. A. Louis, N. W. Ashcroft, Metallization of fluid hydrogen. *Philosophical Transactions of the Royal Society A - Mathematical, Physical and Engineering Sciences*. **356**, 135-- 138 (1998).

27. S. Scandolo, Liquid–liquid phase transition in compressed hydrogen from first-principles simulations. *Proceedings of the National Academy of Sciences*. **100**, 3051–3053 (2003).

28. I. Tamblyn, S. A. Bonev, Structure and Phase Boundaries of Compressed Liquid Hydrogen. *Phys. Rev. Lett.* **104**, 065702 (2010).

29. M. D. Knudson, M. P. Desjarlais, High-Precision Shock Wave Measurements of Deuterium: Evaluation of Exchange-Correlation Functionals at the Molecular-to-Atomic Transition. *Phys. Rev. Lett.* **118**, 035501 (2017).

30. P. M. Celliers *et al.*, Supplementary Material.

31. G. I. Kerley, "Equations of State for Hydrogen and Deuterium" (SAND2003-3613, Sandia National Laboratories, 2003).

32. L. Caillabet, S. Mazevet, P. Loubeyre, Multiphase equation of state of hydrogen from ab initio calculations in the range 0.2 to 5 g/cc up to 10 eV. *Phys. Rev. B*. **83**, 094101 (2011).

33. A. Correa, L. X. Benedict, Equation of State of Hydrogen (2017).

34. S. Brygoo *et al.*, Analysis of laser shock experiments on precompressed samples using a quartz reference and application to warm dense hydrogen and helium. *Journal of Applied Physics*. **118**, 195901 (2015).

35. A. Dewaele, J. H. Eggert, P. Loubeyre, R. Le Toullec, Measurement of refractive index and equation of state in dense He, H2, H2O, and Ne under high pressure in a diamond anvil cell. *Phys. Rev. B*. **67**, 094112 (2003).

36. W. J. Nellis, S. T. Weir, A. C. Mitchell, Minimum metallic conductivity of fluid hydrogen at 140 GPa (1.4 Mbar). *Phys. Rev. B*. **59**, 3434–3449 (1999).

37. N. V. Smith, Classical generalization of the Drude formula for the optical conductivity. *Phys. Rev. B*. **64**, 155106 (2001).

38. Z. M. Geballe, R. Jeanloz, Origin of temperature plateaus in laser-heated diamond anvil cell experiments. *Journal of Applied Physics*. **111**, 123518 (2012).

39. H. Mao, R. J. Hemley, Ultrahigh-pressure transitions in solid hydrogen. *Rev. Mod. Phys.* **66**, 671–692 (1994).

40. P. Loubeyre, F. Occelli, R. LeToullec, Optical studies of solid hydrogen to 320 GPa and evidence for black hydrogen. *Nature*. **416**, 613–617 (2002).

41. D. E. Fratanduono *et al.*, Refractive index of lithium fluoride ramp compressed to 800 GPa. *Journal of Applied Physics*. **109**, 123521 (2011).

42. P. A. Rigg, M. D. Knudson, R. J. Scharff, R. S. Hixson, Determining the refractive index of shocked [100] lithium fluoride to the limit of transmissibility. *J. Appl. Phys.* **116**, 033515 (2014).

43. M. Dion, H. Rydberg, E. Schröder, D. C. Langreth, B. I. Lundqvist, Van der Waals Density Functional for General Geometries. *Phys. Rev. Lett.* **92**, 246401 (2004).

44. J. P. Perdew, K. Burke, M. Ernzerhof, Generalized Gradient Approximation Made Simple. *Phys. Rev. Lett.* **77**, 3865–3868 (1996).

45. K. Lee, É. D. Murray, L. Kong, B. I. Lundqvist, D. C. Langreth, Higher-accuracy van der Waals density functional. *Phys. Rev. B*. **82**, 081101 (2010).

46. E. E. Salpeter, On Convection and Gravitational Layering in Jupiter and in Stars of Low Mass. *The Astrophysical Journal*. **181**, L83 (1973).

47. D. J. Stevenson, E. E. Salpeter, The dynamics and helium distribution in hydrogen-helium fluid planets. *Astrophysical Journal Supplement Series*. **35**, 239–261 (1977).

48. W. Lorenzen, B. Holst, R. Redmer, Demixing of Hydrogen and Helium at Megabar Pressures. *Phys. Rev. Lett.* **102**, 115701 (2009).

49. J. E. KLEPEIS, K. J. SCHAFER, T. W. BARBEE, M. Ross, Hydrogen-Helium Mixtures at Megabar Pressures: Implications for Jupiter and Saturn. *Science*. **254**, 986 (1991).

50. O. Pfaffenzeller, D. Hohl, P. Ballone, Miscibility of Hydrogen and Helium under Astrophysical Conditions. *Phys. Rev. Lett.* **74**, 2599–2602 (1995).

51. J. Vorberger, I. Tamblyn, B. Militzer, S. A. Bonev, Hydrogen-helium mixtures in the interiors of giant planets. *Phys. Rev. B*. **75**, 024206 (2007).

52. M. A. Morales *et al.*, Phase separation in hydrogen–helium mixtures at Mbar pressures. *Proc Natl Acad Sci USA*. **106**, 1324 (2009).

53. M. A. Morales, S. Hamel, K. Caspersen, E. Schwegler, Hydrogen-helium demixing from first principles: From diamond anvil cells to planetary interiors. *Phys. Rev. B*. **87**, 174105 (2013).

54. M. Schöttler, R. Redmer, Ab Initio Calculation of the Miscibility Diagram for Hydrogen-Helium Mixtures. *Phys. Rev. Lett.* **120**, 115703 (2018).

55. B. Militzer, W. B. Hubbard, Ab Initio Equation of State for Hydrogen-Helium Mixtures with Recalibration of the Giant-planet Mass-Radius Relation. *The Astrophysical Journal*. **774**, 148 (2013).

56. A. Becker *et al.*, Ab Initio Equations of State for Hydrogen (H-REOS.3) and Helium (He-REOS.3) and their Implications for the Interior of Brown Dwarfs. *The Astrophysical Journal Supplement Series*. **215**, 21 (2014).

57. R. L. Kauffman *et al.*, High Temperatures in Inertial Confinement Fusion Radiation Cavities Heated with 0.35 μm Light. *Phys. Rev. Lett.* **73**, 2320–2323 (1994).

58. M. D. Rosen, The science applications of the high-energy density plasmas created on the Nova laser. *Phys. Plasmas*. **3**, 1803–1812 (1996).

59. R. E. Marshak, Effect of Radiation on Shock Wave Behavior. *Phys. Fluids*. **1**, 24–29 (1958).

60. H. N. Kornblum, R. L. Kauffman, J. A. Smith, Measurement of 0.1–3 keV x rays from laser plasmas. *Rev. Sci. Instrum.* **57**, 2179–2181 (1986).

61. E. L. Dewald *et al.*, Dante soft x-ray power diagnostic for National Ignition Facility. *Rev. Sci. Instrum.* **75**, 3759–3761 (2004).

62. J. T. Larsen, S. M. Lane, HYADES—A plasma hydrodynamics code for dense plasma studies. *Journal of Quantitative Spectroscopy and Radiative Transfer*. **51**, 179–186 (1994).

63. F. Datchi, P. Loubeyre, R. LeToullec, Extended and accurate determination of the melting curves of argon, helium, ice (H2O), and hydrogen (H2). *Phys. Rev. B*. **61**, 6535–6546 (2000).

64. D. P. Dobson, Self-diffusion in liquid Fe at high pressure. *Physics of the Earth and Planetary Interiors*. **130**, 271–284 (2002).

65. E. S. Posner, D. C. Rubie, D. J. Frost, V. Vlček, G. Steinle-Neumann, High P–T experiments and first principles calculations of the diffusion of Si and Cr in liquid iron. *Geochimica et Cosmochimica Acta*. **203**, 323–342 (2017).

66. H. F. Wilson, B. Militzer, Sequestration of Noble Gases in Giant Planet Interiors. *Phys. Rev. Lett.* **104**, 121101 (2010).

67. L. M. Barker, R. E. Hollenbach, Laser interferometer for measuring high velocities of any reflecting surface. *J. Appl. Phys.* **43**, 4669–4675 (1972).

68. P. M. Celliers *et al.*, Line-imaging velocimeter for shock diagnostics at the OMEGA laser facility. *Rev. Sci. Instrum.* **75**, 4916–4929 (2004).

69. R. E. Setchell, Refractive index of sapphire at 532 nm under shock compression and release. *J. Appl. Phys.* **91**, 2833–2841 (2002).

70. C. T. Silbernagel, P. Torres, D. H. Kalantar, in *Proc. SPIE* (2004), vol. 5559, pp. 435–442.

71. P. Datte *et al.*, in *Proc. SPIE* (SPIE, 2013; http://dx.doi.org/10.1117/12.2026893), vol. 8850, p. 88500G.

72. G. R. Labaria, A. L. Warrick, P. M. Celliers, D. H. Kalantar, in *Proc. SPIE* (2015), vol. 9345, p. 93450Q.

73. M. Takeda, H. Ina, S. Kobayashi, Fourier-transform method of fringe-pattern analysis for computer-based topography and interferometry. *J. Opt. Soc. Am.* **72**, 156–60 (1982).

74. P. Tomassini *et al.*, Analyzing laser plasma interferograms with a continuous wavelet transform ridge extraction technique: the method. *Appl. Opt.* **40**, 6561–6568 (December DEC 102001).

75. M. K. Philpott, A. George, G. Whiteman, J. De'Ath, J. C. F. Millett, The application of line imaging velocimetry to provide high resolution spatially resolved velocity data in plate impact experiments. *Meas. Sci. Tech.* **26**, 125204 (2015).

76. S. Crockett, S. Rudin, "Lithium Fluoride Equation of State (SESAME 7271)" (LA-UR-06-8401, Los Alamos National Laboratory, 2006).

77. J.-P. Davis, M. D. Knudson, L. Shulenburger, S. D. Crockett, Mechanical and optical response of [100] lithium fluoride to multi-megabar dynamic pressures. *J. Appl. Phys.* **120**, 165901 (2016).

78. S. A. Bonev, E. Schwegler, T. Ogitsu, G. Galli, A quantum fluid of metallic hydrogen suggested by first-principles calculations. *Nature*. **431**, 669–672 (2004).

79. E. Gregoryanz, A. F. Goncharov, K. Matsuishi, H. Mao, R. J. Hemley, Raman Spectroscopy of Hot Dense Hydrogen. *Phys. Rev. Lett.* **90**, 175701 (2003).

80. S. Deemyad, I. F. Silvera, Melting Line of Hydrogen at High Pressures. *Phys. Rev. Lett.* **100**, 155701 (2008).

81. M. I. Eremets, I. A. Trojan, Evidence of maximum in the melting curve of hydrogen at megabar pressures. *JETP Letters*. **89**, 174–179 (2009).

82. H. Shimizu, E. M. Brody, H. K. Mao, P. M. Bell, Brillouin Measurements of Solid n-H2 and n-D2 to 200 kbar at Room Temperature. *Phys. Rev. Lett.* **47**, 128–131 (1981).

83. W. J. Evans, I. F. Silvera, Index of refraction, polarizability, and equation of state of solid molecular hydrogen. *Phys. Rev. B*. **57**, 14105–14109 (1998).

84. P. C. Souers, *Hydrogen properties for fusion energy* (University of California, Berkeley, 1986).

85. M. M. Marinak *et al.*, Three-dimensional HYDRA simulations of National Ignition Facility targets. *Physics of Plasmas*. **8**, 2275–2280 (2001).

86. P. M. Celliers, thesis, University of British Columbia, Vancouver, British Columbia (1987). doi: 10.14288/1.0085458

87. P. Colella, P. R. Woodward, The Piecewise Parabolic Method (PPM) for gas-dynamical simulations. *J. Comp. Phys.* **54**, 174–201 (1984).

88. J. K. Dukowicz, A general, non-iterative Riemann solver for Godunov's method. *J. Comp. Phys.* **61**, 119–137 (1985).

89. T. S. Moss, Relations between the refractive index and energy gap of semiconductors. *Phys. Status Solidi B*. **131**, 415 (1985).

90. R. R. Reddy, S. Anjaneyulu, Analysis of the Moss and Ravindra Relations. *Phys. Status Solidi B*. **174**, K91 (1992).

91. P. Hervé, L. K. J. Vandamme, General relation between refractive index and energy gap in semiconductors. *Infrared Phys. Techn.* **35**, 609–15 (1994).

92. N. M. Ravindra, P. Ganapathy, J. Choi, Energy gap–refractive index relations in semiconductors – An overview. *Infrared Phys. Techn.* **50**, 21–9 (2007).

93. A. F. Ioffe, A. R. Regel, *Prog. Semicond.* **4**, 237 (1960).

94. M. Gurvitch, Ioffe-Regel criterion and resistivity of metals. *Phys. Rev. B*. **24**, 7404 (1981).

95. L. A. Collins *et al.*, Dynamical and optical properties of warm dense hydrogen. *Phys. Rev. B*. **63**, 184110 (2001).

96. L. A. Collins, J. D. Kress, D. E. Hanson, Reflectivity of warm dense deuterium along the principal Hugoniot. *Phys. Rev. B*. **85**, 233101 (2012).

97. M. D. Knudson, private communication (2015).

98. D. Ryutov *et al.*, Similarity Criteria for the Laboratory Simulation of Supernova Hydrodynamics. *The Astrophysical Journal*. **518**, 821 (1999).

99. R. P. Drake, *High-Energy-Density Physics Fundamentals, Inertial Fusion, and Experimental Astrophysics* (Springer, Berlin, 2006).

100. J. Clérouin, The viscosity of dense hydrogen: from liquid to plasma behaviour. *Journal of Physics: Condensed Matter*. **14**, 9089 (2002).

101. Z.-G. Li *et al.*, Benchmarking the diffusion and viscosity of H-He mixtures in warm dense matter regime by quantum molecular dynamics simulations. *Physics of Plasmas*. **24**, 052903 (2017).

102. G. Sidebotham, *Heat Transfer Modeling An Inductive Approach* (Springer, New York, 2015; http://dx.doi.org/10.1007/978-3-319-14514-3).

103. F. W. Dittus, L. M. K. Boelter, Heat transfer in automobile radiators of the tubular type. *International Communications in Heat and Mass Transfer*. **12**, 3–22 (1985).

104. D. Jo, O. S. Al-Yahia, R. M. Altamimi, J. Park, H. Chae, Experimental Investigation Of Convective Heat Transfer In A Narrow Rectangular Channel For Upward And Downward Flows. *Nuclear Engineering and Technology*. **46**, 195–206 (2014).

105. P. A. Sterne, S. B. Hansen, B. G. Wilson, W. A. Isaacs, Equation of state, occupation probabilities and conductivities in the average atom Purgatorio code. *High Energy Density Physics*. **3**, 278–282 (2007).

106. B. Holst, M. French, R. Redmer, Electronic transport coefficients from ab initio simulations and application to dense liquid hydrogen. *Phys. Rev. B*. **83**, 235120 (2011).

107. G. W. Collins *et al.*, Temperature Measurements of Shock Compressed Liquid Deuterium up to 230 GPa. *Phys. Rev. Lett.* **87**, 165504 (2001).

108. J. E. Bailey *et al.*, Time-resolved optical spectroscopy measurements of shocked liquid deuterium. *Phys. Rev. B*. **78**, 144107 (2008).